The Molecular and Electronic Structure of Isolated Platinum Sites Enabled by Expedient Measurement of ^{195}Pt Chemical Shift Anisotropy

Amrit Venkatesh,[1,2] Domenico Gioffrè,[3] Benjamin A. Atterberry,[1,2] Lukas Rochlitz,[3] Scott L. Carnahan,[1,2] Zhuoran Wang,[4] Georges Menzildjian,[4] Anne Lesage,[4] Christophe Copéret,[3]* Aaron J. Rossini[1,2]**

[1]*Iowa State University, Department of Chemistry, Ames, IA, USA, 50011*

[2]*US DOE Ames Laboratory, Ames, Iowa, USA, 50011*

[3]*Department of Chemistry and Applied Biosciences, ETH Zürich, CH-8093 Zürich, Switzerland.*

[4]*Univ Lyon, ENS Lyon, Université Lyon 1, CNRS, High-Field NMR Center of Lyon, UMR 5082, F-69100 VILLEURBANNE, France.*

Corresponding Authors

*e-mail: anne.lesage@ens-lyon.fr

*e-mail: ccoperet@ethz.ch

*e-mail: arossini@iastate.edu

Abstract

Techniques that can characterize the molecular structures of dilute surface species are required to facilitate the rational synthesis and improvement of single-site and single-atom, such as the important class of Pt-based systems. In this context, ^{195}Pt solid-state NMR spectroscopy could be an ideal tool for this task because ^{195}Pt NMR spectra and sizeable chemical shift anisotropy (CSA) are highly sensitive probes of the local chemical environment and electronic structure. However, the broadening of ^{195}Pt solid-state NMR spectra by CSA often results in low NMR sensitivity. Furthermore, characterization of Pt sites on surfaces is complicated by the typical low Pt loadings that are between 0.2 to 5 wt.%. Here, we introduce a set of solid-state NMR methods that exploit fast MAS and indirect detection of a sensitive spy nucleus (^{1}H or ^{31}P) to enable rapid acquisition of ^{195}Pt MAS NMR spectra. We demonstrate that high-resolution wideline ^{195}Pt MAS NMR spectra can be in minutes to a few hours for a series of molecular and single-site Pt species grafted on silica with Pt loading of only 3-5 wt.%. Low-power, long-duration, sideband-selective excitation and saturation pulses are incorporated into t_1-noise eliminated (TONE) dipolar heteronuclear multiple quantum coherence (D-HMQC), perfect echo resonance echo saturation pulse double resonance (PE RESPDOR) or *J*-resolved pulse sequences. The complete ^{195}Pt MAS NMR spectrum is then reconstructed by recording a series of 1D NMR spectra where the offset of the ^{195}Pt pulses is varied. Analysis of the ^{195}Pt MAS NMR spectra yields the ^{195}Pt chemical shift tensor parameters. Analysis of the NMR signatures based on relativistic zeroth order approximation (ZORA) DFT calculations enables the rationalization of changes in the observed ^{195}Pt CSA across the series of Pt compounds. Simple and predictive orbital models relate the measured spectral signatures to specific electronic environments and allows the identification of coordination environment by inspection of the CSA (isotropic chemical shift and measured spans).

The methodology developed here paves the way for the detailed structural and electronic analysis of dilute platinum sites in single-atom and single-site heterogeneous catalysts.

TOC Graphic

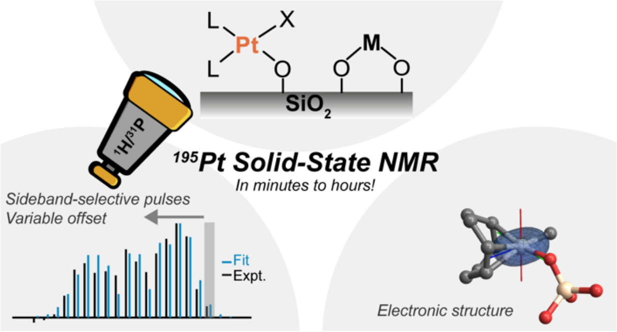

Introduction

Heterogeneous catalysis is widely used in industrial chemistry; it is vital for sustainable chemical processes.[1-5] Recently, single-site[6-7] and single-atom[8] catalysts have emerged as a distinct class of highly efficient heterogeneous catalysts that display unique reactivity, increased catalytic efficiency and improved precious metal utilization. The ultimate goal in catalysis science is to derive detailed structure-activity relationship for rational development. The search for single-site catalysts that comprise of a well-defined coordination environment has thus been an active field of research. In this context, Surface Organometallic Chemistry (SOMC) has emerged as a powerful approach that relies on the controlled reaction of tailored molecular precursors with the functionality of supports, such as the isolated OH groups of oxide materials.[9-11] These well-defined surface species can be used directly as single-site catalysts or as precursors to i) generate isolated metal sites with defined oxidation state and nuclearity, or ii) control the interface, growth and composition of supported nanoparticles.[12-16] A key aspect of SOMC is the need to obtain an atomic-level characterization of surface species, using in particular solid-state nuclear magnetic resonance (NMR) spectroscopy.[5, 17-23]

Notably solid-state NMR spectroscopy has been used to determine the three-dimensional structure of surface single-sites with a sub-angstrom precision.[24-25] The complete measurement of the NMR chemical shift tensor via determination of the isotropic chemical shift and the chemical shift anisotropy (CSA) provides a fingerprint of the electronic structure and symmetry of an atomic environment.[26-29] For example, differences in magnitude of the CSA (the span), determined experimentally, and the computed orientation of the chemical shift tensors can be traced back to specific molecular frontier orbitals and their relative energies in organometallic complexes; this has been used for instance to predict the reactivity of alkene and alkyne metathesis catalysts,[30-34] unravel the electronic structure of organo-tellurides[35] and understand the π-accepting abilities of carbenes.[36-38] Many metal-based catalysts have abundant spin-1/2 isotopes which can theoretically be directly probed by solid-state NMR spectroscopy (^{89}Y, ^{103}Rh, ^{109}Ag, ^{113}Cd, ^{119}Sn, ^{183}W, ^{199}Hg, ^{195}Pt, ^{207}Pb, etc.). However, direct NMR experiments on the metal nucleus of supported catalysts are challenging because of the typically low metal loadings. Consequently, NMR experiments have traditionally been limited to highly receptive isotopes of metals such as aluminum,[39] scandium,[21] vanadium,[40-41] niobium[18] and/or isotopically enriched materials.[22, 42-43] Recently, sensitivity-enhancement by dynamic nuclear polarization (DNP) or proton detection has enabled NMR experiments on catalysts featuring unreceptive nuclei.[44-49]

The noble metal platinum is utilized in numerous catalytic processes.[8, 50-52] However, Pt(II) sites often adopt a square-planar geometry, giving rise to very large magnitude of ^{195}Pt CSA of several thousand ppm, making acquisition of ^{195}Pt solid-state NMR spectra challenging.[53-55] Yet, measurement of ^{195}Pt isotropic chemical shifts and CSA provides invaluable information by providing direct insight into the identity and symmetry of atoms within the Pt coordination sphere as well as a full understanding of the electronic structure.[55-60] Towards this goal, various schemes have been proposed for the acquisition of wideline solid-state NMR spectra.[53, 61-63] DNP has been used to enhance further the sensitivity of wideline solid-state NMR experiments under static[46, 64-65] and moderate magic angle spinning (MAS) conditions.[49] However, these methods offer poor ^{195}Pt NMR resolution. Recently, we used static DNP experiments to characterize a model Pt single-site catalyst at 3.7 wt.% Pt loading, however even with DNP, six days of acquisition time was required to measure the ^{195}Pt CSA.[66] A rapidly developing approach to improve the sensitivity and resolution of solid-state NMR experiments, which can be readily applied with standard solid-state NMR spectrometers, is indirect detection of insensitive nuclei under fast MAS.[67-70]

In this work, we demonstrate that ^{195}Pt chemical shift tensors can be measured with high resolution in only minutes to a few hours for a series of molecular and single-site Pt species grafted on silica with Pt loading of only 3-5 wt.% (Figure 1). Our approach consists in the incorporation of long duration, low-power sideband-selective pulses into indirect detection ^{1}H{^{195}Pt} t_1-noise eliminated heteronuclear multiple quantum coherence (TONE D-HMQC), perfect echo resonance echo saturation pulse double resonance (PE RESPDOR) and ^{31}P{^{195}Pt} *J*-resolved pulse sequences all of which are performed with fast MAS ($\nu_{rot} \geq 25$ kHz). By varying the offset of the sideband-selective pulses across the ^{195}Pt spectrum and monitoring the 1D NMR signal intensity, complete ^{195}Pt NMR spectra can be obtained with sensitivity far exceeding that offered by traditional methods. These schemes, together with DFT computations, were applied to unravel the molecular and electronic signatures of Pt species. The large variations in experimental ^{195}Pt CSA can be related to simple orbital models, rationalizing the effect of different coordination environments on ^{195}Pt CSA patterns.

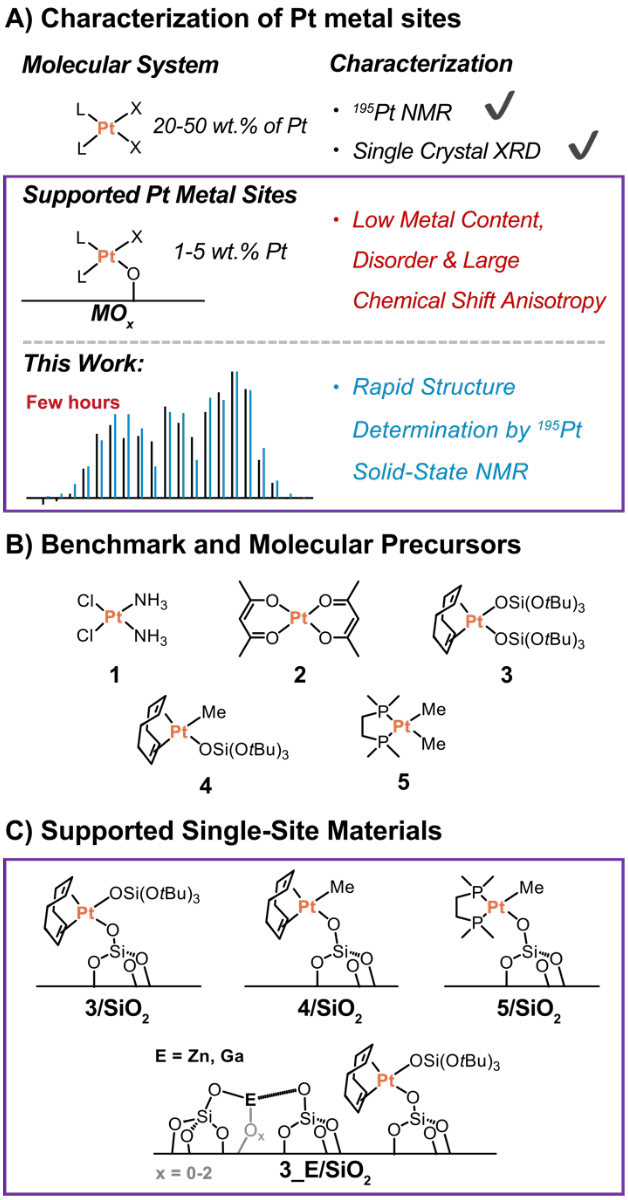

Figure 1. (A) Graphical summary of the characterization of molecular and supported Pt metal sites and the development of methodology for fast structure determination using ^{195}Pt solid-state NMR. Scheme showing the structures of the (B) molecular and (C) supported single-site Pt compound studied in this work. The Pt loadings of the supported compounds were 3.73 wt.% (**3/SiO₂**), 2.77 wt.% (**3_Zn/SiO₂**), 4.37 wt.% (**3_Ga/SiO₂**), 4.96 wt.% (**4/SiO₂**) and 4.39 wt.% (**5/SiO₂**).

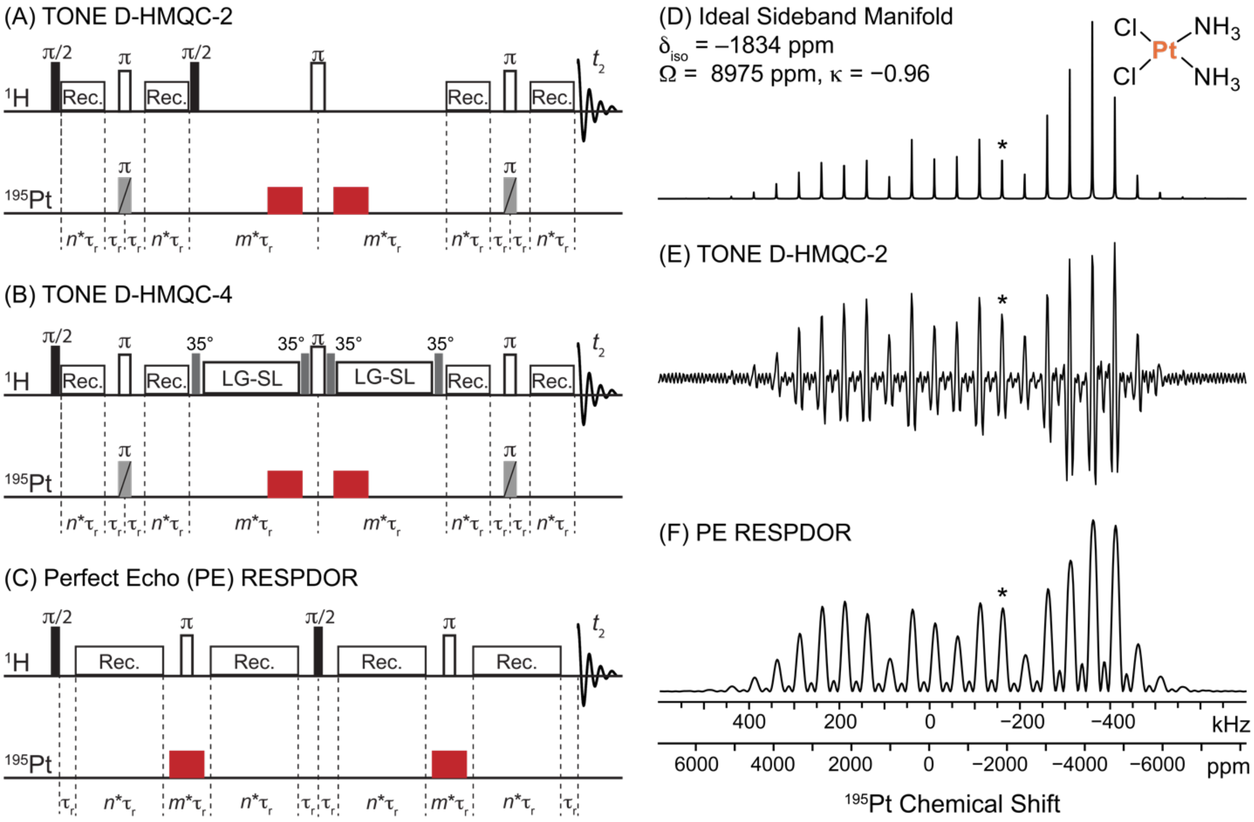

Figure 2. $^{1}H\{^{195}Pt\}$ (A) TONE D-HMQC-2, (B) TONE D-HMQC-4 and (C) Perfect echo (PE) RESPDOR pulse sequences with long duration, low-rf field sideband-selective excitation/saturation pulses on the ^{195}Pt channel (red rectangles). *m* and *n* are positive integers and τ_r denotes a rotor period. (D-F) Simulations of ^{195}Pt CSA sideband manifolds of cisplatin at 50 kHz MAS and $B_0 = 9.4$ T. (D) Ideal simulation. Numerical SIMPSON simulations of sideband manifolds obtained by varying the offset in steps of 1 kHz of 60 μs ^{195}Pt sideband-selective (9 kHz rf field) excitation or saturation pulses within (E) TONE D-HMQC or (F) PE RESPDOR pulse sequences, respectively. The previously reported values of ^{195}Pt isotropic shifts, and CSA parameters (span (Ω) and skew (κ)) were used in all cases. The isotropic shift is indicated by an asterisk. Additional details on simulations are provided in the experimental section.

Results and Discussion

Sideband-Selective ^{195}Pt NMR methods. Wideline $^{1}H\{^{195}Pt\}$ D-HMQC experiments[71-74] use short duration high-powered excitation pulses to excite the broad ^{195}Pt NMR spectra and small, rotor-asynchronous t_1-increments to finely sample the indirect dimension time domain signal, allowing observation of the entire spinning sideband manifold in the frequency domain after 2D Fourier transformation. However, when the indirect dimension frequency domain signal is broken into a series of sidebands due to a significant CSA, the sensitivity of the NMR experiment is significantly reduced (Figure S1), and further attenuated by t_1-noise. Therefore, wideline 2D ^{1}H{^{195}Pt} D-HMQC experiments have been so far limited to molecular platinum compounds where the platinum has a high concentration. Recently Paluch *et al.* showed that the traditional microsecond duration, high-rf field excitation pulses ($\nu_1 > 150$ kHz) used in ^{1}H{^{195}Pt} D-HMQC experiments on samples with large CSA can be replaced with low-rf field pulses (5-50 kHz) with durations of one rotor cycle or longer.[75] However, the use of these longer duration excitation pulses makes the D-HMQC experiment very sensitive to the frequency offset of the indirectly detected nucleus; the pulses must be applied on resonance with an isotropic peak or sideband; hence, we denote these pulses as being sideband-selective. Here, we incorporate sideband-selective excitation or saturation ^{195}Pt pulses into the D-HMQC and RESPDOR pulse sequences, respectively. To obtain the MAS ^{195}Pt solid-state NMR spectra a series of one-dimensional, sideband-selective D-HMQC or RESPDOR experiments are performed. The ^{195}Pt pulse offset frequency is stepped in increments equal to the MAS frequency. By plotting the 1D NMR signal intensities as a function of the ^{195}Pt pulse offset the MAS ^{195}Pt NMR spectrum can be reconstructed (Figure 2 and Figure S2-S4). This method is analogous to previous work that utilized indirect detection schemes such as TRAPDOR,[76] REAPDOR,[77] RESPDOR[78] or PROSPR[79] where the signal dephasing of the detected nucleus at different transmitter offsets was used to reconstruct the NMR spectrum of a heteronucleus.

D-HMQC and RESPDOR with $SR4_1^2$ recoupling[80] are susceptible to MAS instability that results in a random variation of the ^{1}H signals, thereby reducing reproducibility.[81-83] To address this problem we use our recently described t_1-noise eliminated (TONE) D-HMQC pulse sequences to reduce t_1-noise and improve sensitivity (see Figure S5 for a comparison of sideband-selective D-HMQC vs TONE D-HMQC experiments).[74, 83] Additionally, we describe a perfect echo (PE)

RESPDOR pulse sequence that incorporates the perfect echo symmetry[84] into RESPDOR (Figure 2C). PE RESPDOR offers improved robustness towards MAS frequency fluctuations and homonuclear couplings in comparison to standard RESPDOR (see Note S1 and Figures S6-S11 for details). The use of PE RESPDOR to accurately measure heteronuclear distances is discussed elsewhere.[85]

Figure 2D shows the simulated ideal ^{195}Pt sideband manifold of cisplatin, based on the previously reported CSA parameters $\delta_{iso} = -1834$ ppm, $\Omega = 8975$ ppm and $\kappa = -0.96$,[60, 71] where δ_{iso}, Ω and κ denote the isotropic chemical shift, span and skew of the chemical shift tensor, respectively. Next, we performed numerical SIMPSON[86-88] simulations which show the effects of varying the offset of 60 μs, 9 kHz rf field ^{195}Pt pulses in 2 kHz steps for the TONE D-HMQC-2 and PE RESPDOR pulse sequences (Figure 2E and 2F). A comparison of Figure 2E and 2F with Figure 2D shows that the ^{195}Pt NMR spectrum is reproduced in both cases, with peak intensities obtained with the PE RESPDOR sequence being very similar to the ideal spectrum (Figure 2D).

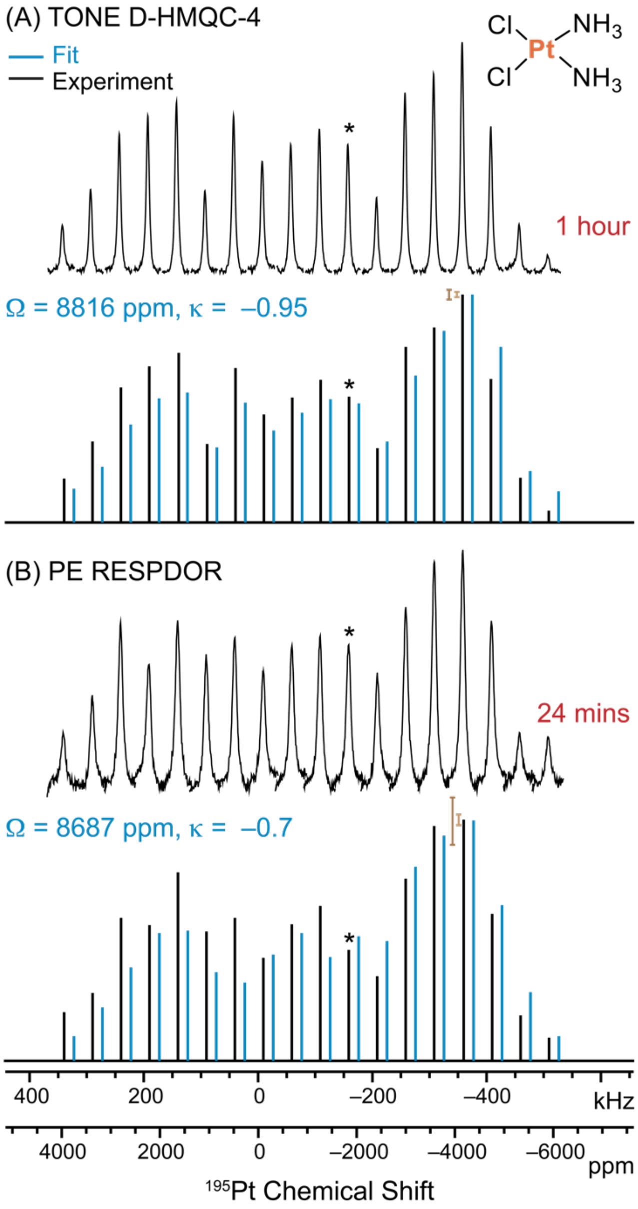

Figure 3. ^{1}H{^{195}Pt} sideband-selective solid-state NMR experiments on cisplatin (**1**) performed with a 50 kHz MAS frequency and 60 µs, 9 kHz rf field sideband-selective ^{195}Pt pulses. Sideband-selective (A) TONE D-HMQC-4 and (B) PE RESPDOR experiments; (top) 1D ^{1}H{^{195}Pt} NMR spectra recorded with different ^{195}Pt selective pulse offsets and (bottom, black sticks) stick representation of the ^{1}H{^{195}Pt} signal intensities. (blue sticks) SIMPSON simulated intensities corresponding to the indicated CS tensor parameters which gave the lowest RMSD. Error bars are provided only for the most intense sideband as the same magnitude of error applies to all sidebands. The error bar on the right accounts only for SNR whereas the error bar shown on the left accounts for both MAS instability and SNR. The cumulative errors in the signal intensities are about 2% for TONE D-HMQC-4 and 10% for the PE RESPDOR. Total experiment times are indicated in red.

^{195}Pt Solid-State NMR of Benchmark Precursors. We tested the sideband-selective ^{1}H{^{195}Pt} TONE D-HMQC-4 and PE RESPDOR experiments with the two prototypical molecular

compounds cisplatin (**1**) and Pt(acac)$_2$ (**2**). Figure 3 shows the results obtained with cisplatin. Since the selective saturation pulses have narrow bandwidths, pulses must be applied precisely on-resonance with ^{195}Pt NMR signals. The position of a sideband can be located using a high sensitivity rotor-synchronized D-HMQC experiment[66, 73, 75] or by varying the offset of the sideband-selective pulses in steps of 1-2 kHz, until the signal (or dephasing) is observed; the former approach was employed throughout this work. Plotting the ^{1}H{^{195}Pt} TONE D-HMQC-4 signal as a function of the pulse offset yields the sideband intensities (black trace, Figure 3A). The CSA parameters were determined by least-squares fitting of the sideband intensities using SIMPSON simulations (Figure S12). The resulting CSA parameters (Ω = 8816 ppm, κ = –0.95) are in close agreement with the known values (Ω = 8975 ppm, κ = −0.96).[60, 71] Similarly, sideband-selective ^{1}H{^{195}Pt} PE RESPDOR experiments were also performed and the intensities of the dephasing difference spectra at different ^{195}Pt offsets were plotted (Figure 3B). The PE RESPDOR dataset was normalized to an experiment with the selective-saturation pulse applied far off-resonance to the ^{195}Pt signals. Least-squares fit of this data with SIMPSON simulations provided Ω = 8687 ppm, κ = –0.7, with only a small deviation from the ideal values, which can be explained by the slight fluctuation of the signal intensities due to MAS instability (Figure S11C).

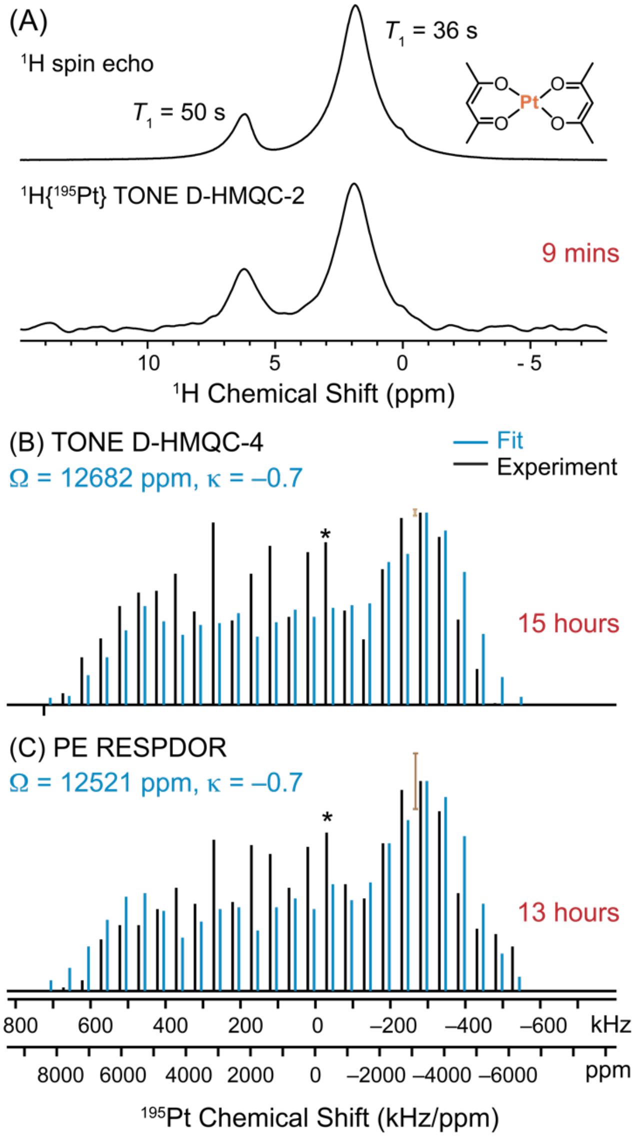

Figure 4. ^{195}Pt sideband-selective experiments on Pt(acac)$_2$ (**2**) performed with a 50 kHz MAS frequency. (A) (top) ^{1}H spin echo and (bottom) standard 1D ^{1}H{^{195}Pt} TONE D-HMQC-2 spectra. (black trace) Sideband-selective (B) TONE D-HMQC-4, and (C) PE RESPDOR experiments. The dephasing difference ($S_0 - S$) of the PE RESPDOR signal at 6.3 ppm (CH proton) was used and the maximum dephasing was about 7%. (blue trace) SIMPSON simulations with (B) TONE D-HMQC-2 and (C) PE RESPDOR and the indicated CS tensors parameters that yielded the lowest RMSD. Error bars are provided only for the most intense sideband as the same magnitude of error applies to all sidebands. The error bar shown for experimental TONE D-HMQC-4 accounts for SNR (ca. 1.6% of signal intensity) whereas the 14% error bar shown for PE RESPDOR account for both MAS instability and SNR. Total experiment times are indicated in red.

^{1}H{^{195}Pt} sideband-selective NMR methods were also applied to **2**, which has not previously been analyzed by ^{195}Pt solid-state NMR previously. The 1D ^{1}H solid-state NMR spectrum of **2** showed two signals at 1.9 and 6.3 ppm, corresponding to the methyl and CH hydrogen atoms of the acac ligands, respectively (Figure 4A). A standard 1D $^{1}H\{^{195}Pt\}$ TONE D-HMQC-2 spectrum showing both ^{1}H NMR signals can be obtained in a few minutes (Figure 4A), despite the long ^{1}H T_1 (36 and 50 s for the methyl and methine ^{1}H, respectively) and small ^{1}H-^{195}Pt heteronuclear dipolar couplings of ca. 300 Hz. As we have shown previously, $^{1}H\{^{195}Pt\}$ S-REDOR experiments can be used to precisely measure ^{1}H-^{195}Pt distances.[66, 74] In case of **2**, the CH proton shows faster dephasing due to a shorter Pt-HC distance of 4.29 Å (expected dipolar coupling constant of 332 Hz) in comparison to a longer 4.41 Å distance (expected dipolar coupling constant of 306 Hz) to the nearest methyl proton (Figure S13A).

Rotor-synchronized 2D TONE D-HMQC-4 experiments were performed with MAS frequencies of 50 and 52 kHz to measure the ^{195}Pt isotropic chemical shift (Figure S13B). Notably, two ^{195}Pt signals at –360 and –385 ppm were observed, suggesting that the sample studied here contains two crystallographically inequivalent sites, in disagreement with the currently known crystal structure of **2**.[89] It is possible that the sample of **2** studied here exists as a different polymorph. A wideline D-HMQC experiment takes 45 hours and it suffers from an incomplete excitation because of the large CSA (Figure S13C), the Ω was estimated to be 11800 ppm (Figure S13D, Note S2), in good agreement with a previous estimate of 10000 ppm from solution ^{195}Pt NMR relaxation experiments.[90] On the other hand, with sideband-selective TONE D-HMQC-4 and PE RESPDOR experiments, ^{195}Pt NMR spectra were obtained in only 15 and 13 hours, respectively (Figure 4). Fits of the ^{195}Pt NMR spectra obtained with TONE D-HMQC-4 or PE RESPDOR yielded a κ of –0.7 and similar Ω values of 12682 ppm or 12521 ppm (Figure S14), which are in good agreement with the parameters determined from the wideline ^{195}Pt NMR spectrum (Figure S13D).

In summary, the sideband-selective $^{1}H\{^{195}Pt\}$ TONE D-HMQC and PE RESPDOR experiments were performed with unprecedented sensitivity: the entire ^{195}Pt MAS NMR spectrum of cisplatin was obtained in only 1 hour with TONE D-HMQC-4 and 24 minutes with PE RESPDOR, while for Pt(acac)$_2$ sideband patterns were obtained within 15 hours, demonstrating the value of sideband-selective techniques. Given the high signal to noise ratios observed with cisplatin (Figure S15), preliminary sideband manifolds can typically be obtained in a few minutes for most pure compounds. With these remarkable first results on molecular compounds, sideband-selective $^{1}H\{^{195}Pt\}$ solid-state NMR experiments were then applied to examine silica-supported platinum compounds.

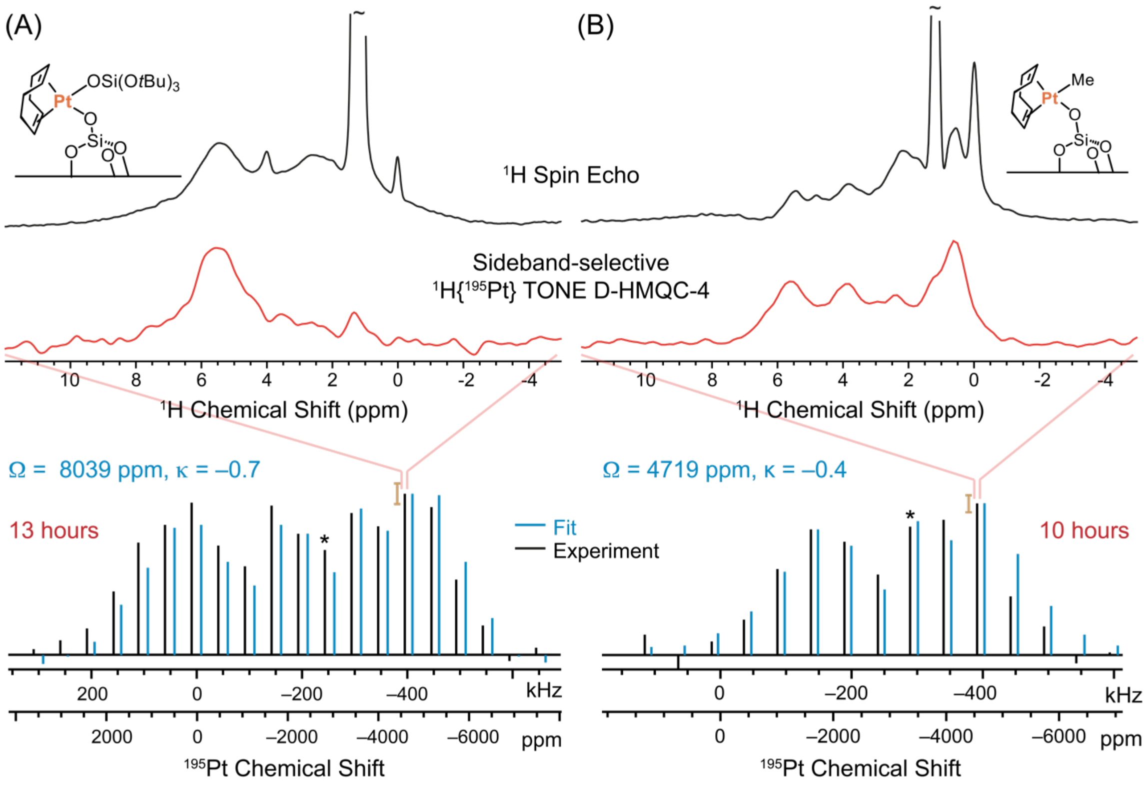

Figure 5. ^{195}Pt sideband-selective NMR experiments with silica-supported Pt compounds (A) **3/SiO₂** and (B) **4/SiO₂**. (top) 1D ^{1}H spin echo NMR spectra, (middle) sideband-selective $^{1}H\{^{195}Pt\}$ TONE D-HMQC-4 spectra at the indicated ^{195}Pt offset (corresponding to the most intense sidebands). (bottom, black trace) $^{1}H\{^{195}Pt\}$ sideband-selective TONE D-HMQC-4 spectra of (A) **3/SiO₂** and (B) **4/SiO₂**, obtained from the intensities of the CH ^{1}H NMR signal at ca. 5.5 ppm and the CH$_3$ ^{1}H NMR signal at 1.1 ppm, respectively. (blue trace) SIMPSON simulations with TONE D-HMQC-2 using ^{195}Pt (A) $\Omega = 8039$ ppm, $\kappa = -0.7$ and

(B) Ω = 4719 ppm, κ = −0.4, which correspond to the CS tensors parameters that give the lowest RMSD. The error bar accounting for SNR is shown for the most intense sideband. Intense *t*-butoxide methyl signals were truncated in the ^{1}H spin echo NMR spectra. All experiments were performed with a 50 kHz MAS frequency.

^{195}Pt Solid-State NMR of Molecular and Single-Site Compounds. In order to investigate materials relevant to heterogeneous catalysis, we first measured the ^{195}Pt CSA of a model single-site compound prepared by grafting [(COD)Pt(OSi(O*t*Bu)$_3$)$_2$] on partially dehydroxylated silica[12, 91] (**3/SiO$_2$**) with a surface Pt loading of 3.73 wt.% (ca. 1 Pt/nm^2). Recently, we determined the CS tensor parameters of this compound (δ_{iso} = −2819 ppm, Ω = 8412 ppm, κ = −0.77) using a combination of DNP-SENS $^{1}H \rightarrow ^{195}Pt$ BRAIN-CP WCPMG and isotropic fast MAS ^{1}H-^{195}Pt TONE D-HMQC experiments that required approximately five days and one day of spectrometer time, respectively.[66] As we showed previously, the ^{195}Pt isotropic peak and sidebands of the grafted compound are broad (ca. 8-10 kHz full width at half maximum) because there is an inhomogeneous distribution of isotropic shifts.[66] To enable efficient excitation/saturation in the sideband-selective experiments, 40 μs excitation pulses with an optimal rf field of 16 kHz were used (Table S1, Figure S3-S4). The sideband-selective TONE D-HMQC-4 experiment yielded the ^{195}Pt CSA pattern within 13 hours and it was fit to Ω = 8039 ppm, κ = −0.7, consistent with the reported values mentioned above (Figure 5A and Figure S16-S17). Although PE RESPDOR showed only a maximum dephasing of 5% (corresponding to an estimated error of ca. 20% of the dephasing difference signal intensities), a ^{195}Pt NMR spectrum was obtained in only 3.3 hours and fits of this spectrum gave Ω = 7876 ppm, κ = −0.8 (Figure S18). The significant savings in time (few hours) compared to our previous report (6 days),[66] demonstrates the high sensitivity of the sideband-selective experiments for measurement of ^{195}Pt NMR spectra.

To probe if the sideband-selective experiments are suitable to detect differences in the ligand environment of supported compounds, we obtained ^{195}Pt NMR spectra of

[(COD)PtMe]/SiO_2 (**4/SiO_2**) that has a surface Pt loading of 4.96 wt.%. In **4/SiO_2,** the –OSi(O*t*Bu)$_3$ ligand of **3/SiO_2** is replaced with a methyl ligand. Consequently, in **4/SiO_2** the two sets of olefinic protons in the COD ligand become inequivalent due to the *trans* effect; the CH protons *trans* to the methyl and –OSi groups appear at 5.6 and 3.9 ppm, respectively, in close accordance with the solution ^{1}H NMR spectrum of **4** (δ_{iso} = 5.90 and 3.56 ppm, Figure S18).[12] As a result, the signal intensities of the olefinic protons is halved in comparison to **3/SiO_2** which will decrease the overall indirect detection sensitivity. However, the methyl group protons at 1.2 ppm are also in close proximity to the Pt center and can also be used as spy nuclei for the indirect detection experiments. Indeed, all of these ^{1}H NMR signals are clearly observed in rotor-synchronized 1D and 2D ^{1}H{^{195}Pt} TONE D-HMQC-2 spectra (Figure 5B, Figure S19), indicating that the COD and methyl ligand remain coordinated to Pt after grafting on silica. For **4/SiO_2** δ_{iso} was determined to be –3327 ppm from the rotor-synchronized 2D ^{1}H{^{195}Pt} TONE D-HMQC-2 spectra (Figure S19). A single 1D sideband-selective ^{1}H{^{195}Pt} TONE D-HMQC-4 spectrum can be acquired in only 40 minutes with a SNR of 20 at the most intense sideband. Consequently, the entire ^{195}Pt MAS NMR spectrum of **4/SiO_2** was obtained in only 10 hours (Figure 5B). Least-squares fitting of the resulting pattern with SIMPSON simulations provides Ω = 4719 ppm, $\kappa = -0.7$ (Figure S20), which illustrates a significant lowering of the span in comparison to **3/SiO_2**. These results demonstrate that the new solid-state NMR experiments are well suited to capture differences in the Pt environment.

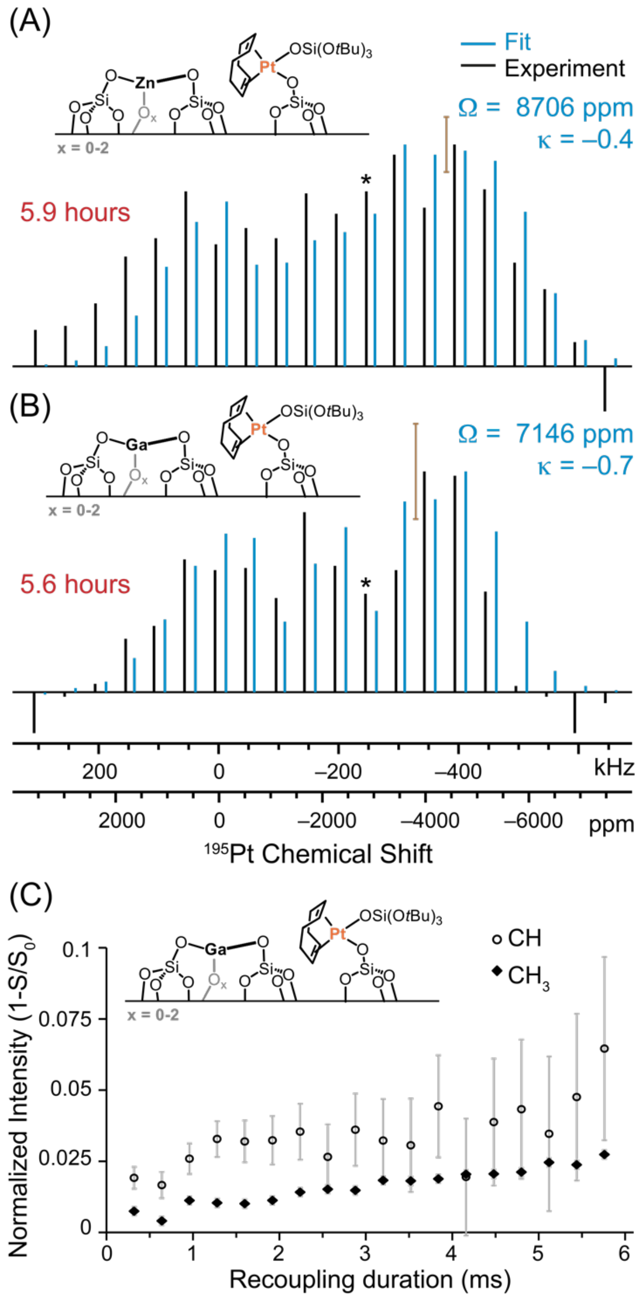

Figure 6. Sideband-selective $^{1}H\{^{195}Pt\}$ PE RESPDOR experiments on single-site Pt compounds (A) **3_Zn/SiO$_2$** and (B) **3_Ga/SiO$_2$**. (black) Experimental patterns and (blue) SIMPSON simulations performed using the indicated CS tensor parameters. A maximum experimental signal dephasing of (A) 6.4% and (B) 3.7% was observed. Error bars are shown for the most intense sidebands. (C) $^{1}H\{^{71}Ga\}$ PE RESPDOR build-up curves: plot showing normalized dephasing difference signal intensity ($1–S/S_0$) as a function of dipolar recoupling duration for (circles) CH and (diamonds) CH_3 groups in the grafted [(COD)Pt(OSi(O*t*Bu)$_3$)] complex.

In order to probe the sensitivity of these newly developed NMR experiments to modifications on the surface, we investigated the surface species of [(COD)Pt(OSi(O*t*Bu)$_3$)$_2$]

grafted on silica doped with different Lewis acids, namely Zn(II) and Ga(III), in order to probe the local environment around Pt and determine if there are any interactions of Pt with the adjacent Lewis acid sites. These systems, denoted **3_Zn/SiO$_2$** and **3_Ga/SiO$_2$**, were chosen because they are used as precursors to prepare highly active mixed-metal nanoparticle catalysts for the non-oxidative propane dehydrogenation.[13, 15-16] The 1D ^{1}H NMR spectra of both compounds clearly show signals corresponding to CH$_3$ (ca. 1.2 ppm), CH$_2$ (ca. 2.2 ppm) and the olefinic CH (ca. 5.6 ppm) protons (Figure S21), in good agreement with the chemical shift assignments of **3/SiO$_2$**.[66] The ligand structure was further confirmed by 2D ^{1}H single quantum-double quantum (SQ-DQ) correlation spectroscopy, and ^{13}C and ^{29}Si DNP-SENS (Figure S21-S23). Rotor-synchronized 2D ^{1}H{^{195}Pt} TONE D-HMQC spectra were used to measure the isotropic ^{195}Pt chemical shifts of –2844 and –2828 ppm for **3_Zn/SiO$_2$** and **3_Ga/SiO$_2$**, respectively (Figure S24). These isotropic shift values are entirely consistent with a similar Pt local environment as found in **3/SiO$_2$** (^{195}Pt δ_{iso} = –2819 ppm).

Figure 6A and 6B shows comparisons between experimental sideband patterns obtained with ^{1}H{^{195}Pt} PE RESPDOR and corresponding SIMPSON simulations using the best fit ^{195}Pt CS tensor parameters. We obtained Ω = 8706 ppm and κ = –0.4 for **3_Zn/SiO$_2$** and Ω = 7146 ppm, κ = –0.7 for **3_Ga/SiO$_2$**, from least-squares fitting (Figure S25). Notably, the ^{195}Pt NMR spectra obtained with the sideband-selective experiments are clearly superior to those obtained with DNP-SENS ^{1}H→^{195}Pt BRAIN-CP-WCPMG[62] NMR experiments, which provided only partial excitation of the ^{195}Pt shielding patterns, with greatly reduced intensity at the high-frequency side of the pattern (Figure S26). Note that similar distortions of intensity were previously seen in the^{1}H→^{195}Pt BRAIN-CP-WCPMG spectrum of **3/SiO$_2$**.[66]

Clearly, the structure of the grafted single-site [(COD)Pt(OSi(O*t*Bu)$_3$)] species in **3_Zn/SiO$_2$** is similar to **3/SiO$_2$**. In case of **3_Ga/SiO$_2$**, the observed ^{195}Pt sideband manifold indicates a span that is lower than that of **3/SiO$_2$** by ca. 1250 ppm, which could indicate differing interactions between the grafted Pt compounds and the co-grafted Ga^{3+} and Zn^{2+} ions, that in turn suggests slight average differences in the conformation and electronic structure. Note that the reduction in span of **3_Ga/SiO$_2$** could also be partially attributed to the error in intensities due to a low PE RESPDOR dephasing of ca. 3.7%. To confirm the proximity of the co-grafted Pt complex and the Ga^{3+} ions, we performed ^{1}H{^{71}Ga} PE RESPDOR experiments which show dephasing of the olefinic CH and the methyl groups of the siloxide ligand (Figure 6C). The slow build-up of the ^{1}H{^{71}Ga} PE RESPDOR curve is consistent with ^{1}H-^{71}Ga inter-nuclear distances on the order of several angstroms. Similar RESPDOR experiments could not be performed on **3_Zn/SiO$_2$** due to the low ^{67}Zn natural abundance of 4.1%.

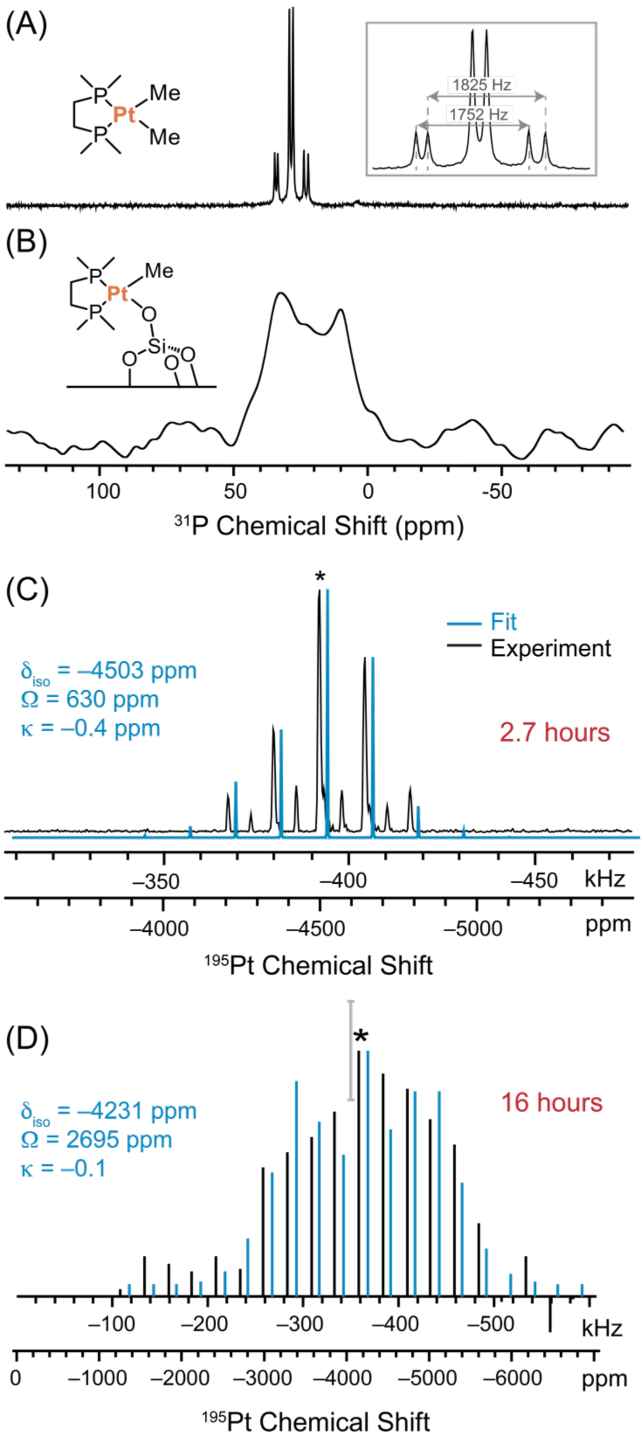

Figure 7. ^{31}P{^{195}Pt} NMR experiments on compounds **5** and **5/SiO$_2$**. ^{1}H→^{31}P CP-MAS spectra of (A) **5** and (B) **5/SiO$_2$** obtained at 25 kHz MAS. (C) 1D ^{195}Pt projection from a 2D ^{31}P{^{195}Pt} CP constant time *J*-HMQC spectrum of **5** acquired with a 12.5 kHz MAS frequency. (D) ^{195}Pt CSA pattern of **5/SiO$_2$** acquired with a sideband-selective ^{1}H-^{31}P{^{195}Pt} CP *J*-resolved pulse sequence using CPMG detection and a 25 kHz MAS frequency.

$^{31}P\{^{195}Pt\}$ J-HMQC and J-Resolved NMR Experiments. So far, we have used the highly sensitive ^{1}H spins near ^{195}Pt to indirectly observe ^{195}Pt CSA patterns and determine the local structure of single-site Pt compounds. However, many catalysts will contain ligands with nuclei such as ^{31}P that are directly attached to the central Pt metal atom and can serve as a spy nucleus because they offer good NMR sensitivity; these nuclei can also be utilized to perform sideband-selective experiments. To establish such a generalized approach, we demonstrate the characterization of the precursor [(DMPE)PtMe$_2$] (**5**) and the corresponding supported compound **5/SiO$_2$** (Figure 1) using ^{1}H-^{31}P{^{195}Pt} solid-state NMR experiments performed with a triple-resonance 2.5 mm HXY probe.

Figure 7A shows a ^{1}H→^{31}P CP-MAS spectrum of **5**, which can be obtained within a few minutes. Two ^{31}P sites are observed at 29.1 ppm and 30.4 ppm with $^{1}J_{P\text{-}Pt}$ values of 1825 and 1750 Hz, respectively. Both the chemical shifts and $^{1}J_{P\text{-}Pt}$ values agree closely with previous solution NMR measurements.[92] Note that small variations in bond angles/lengths in the solid-state can create inequivalence and cause two ^{31}P NMR signals to be observed instead of one. Next, we performed a ^{31}P{^{195}Pt} constant-time *J*-HMQC experiment on **5** (Figure S27A). The constant-time format of the HMQC experiment enables arbitrary and large F_1 spectral widths necessary for the indirect detection of ^{195}Pt spinning sideband manifolds.[71] The resulting ^{195}Pt NMR spectrum was fit to CS tensor parameters of δ_{iso} = –4503 ppm, Ω = 630 ppm and κ = –0.4 (Figure 7C).

The ^{31}P CP-MAS spectrum of **5/SiO$_2$** has a low SNR (ca. 9 after 3.5 hours of acquisition) because of the low Pt surface loading of 4.4 wt % and signal broadening due to surface disorder (Figure 7B). Additionally, the ^{31}P NMR spectrum of **5/SiO$_2$** shows two characteristic features at 35 and 10 ppm. The ^{31}P chemical shifts of the two phosphines likely differ because one is *trans* to a methyl (35 ppm), while the other is *trans* to a siloxide group (10 ppm). CPMG detection was used to accelerate all $^{31}P\{^{195}Pt\}$ solid-state NMR experiments on **5/SiO$_2$**. Due to low sensitivity, it was not possible to perform a $^{31}P\{^{195}Pt\}$ wideline *J*-HMQC experiment on **5/SiO$_2$**. However, a rotor-synchronized $^{31}P\{^{195}Pt\}$ *J*-HMQC spectrum could be obtained and was used to determine that the ^{195}Pt isotropic chemical shift of **5/SiO$_2$** was –4231 ppm (Figure S27B, Figure S28). The ^{195}Pt CSA of **5/SiO$_2$** was then measured using a $^{31}P\{^{195}Pt\}$ CP *J*-resolved (heteronuclear spin echo) experiment with 40 μs ^{195}Pt sideband-selective saturation pulses at 22 kHz rf field (Figure 7D). The dephasing observed for CPMG spikelets at 36 and 29 ppm was averaged to improve the SNR (Figure S29). With this approach, the sideband manifold could be obtained in only 16 hours. Least-squares fitting of the sideband manifold yields Ω = 2695 ppm and κ = –0.1 (Figure 7D, Figure S30). Interestingly, the values of δ_{iso} for **5** and **5/SiO$_2$** only differ by 272 ppm, a small difference with respect to the large chemical shift range of ^{195}Pt. However, the value of Ω for **5/SiO$_2$** is considerably larger than that measured for **5** (2695 *vs* 630 ppm), illustrating the importance of measuring CSA to probe the changes in the local Pt coordination environment upon grafting. The origin of the large difference in ^{195}Pt CSA is further discussed below. In conclusion, NMR-active nuclei other than ^{1}H may be used for indirect detection of ^{195}Pt CSA patterns. Sideband-selective $^{31}P\{^{195}Pt\}$ CP *J*-resolved experiments enabled acquisition of the ^{195}Pt NMR spectrum of **5/SiO$_2$**in only 16 hours. Sideband-selective ^{195}Pt *J*-resolved and *J*-HMQC experiments are also likely to be valuable for the detailed molecular level understanding of single-site Pt materials.

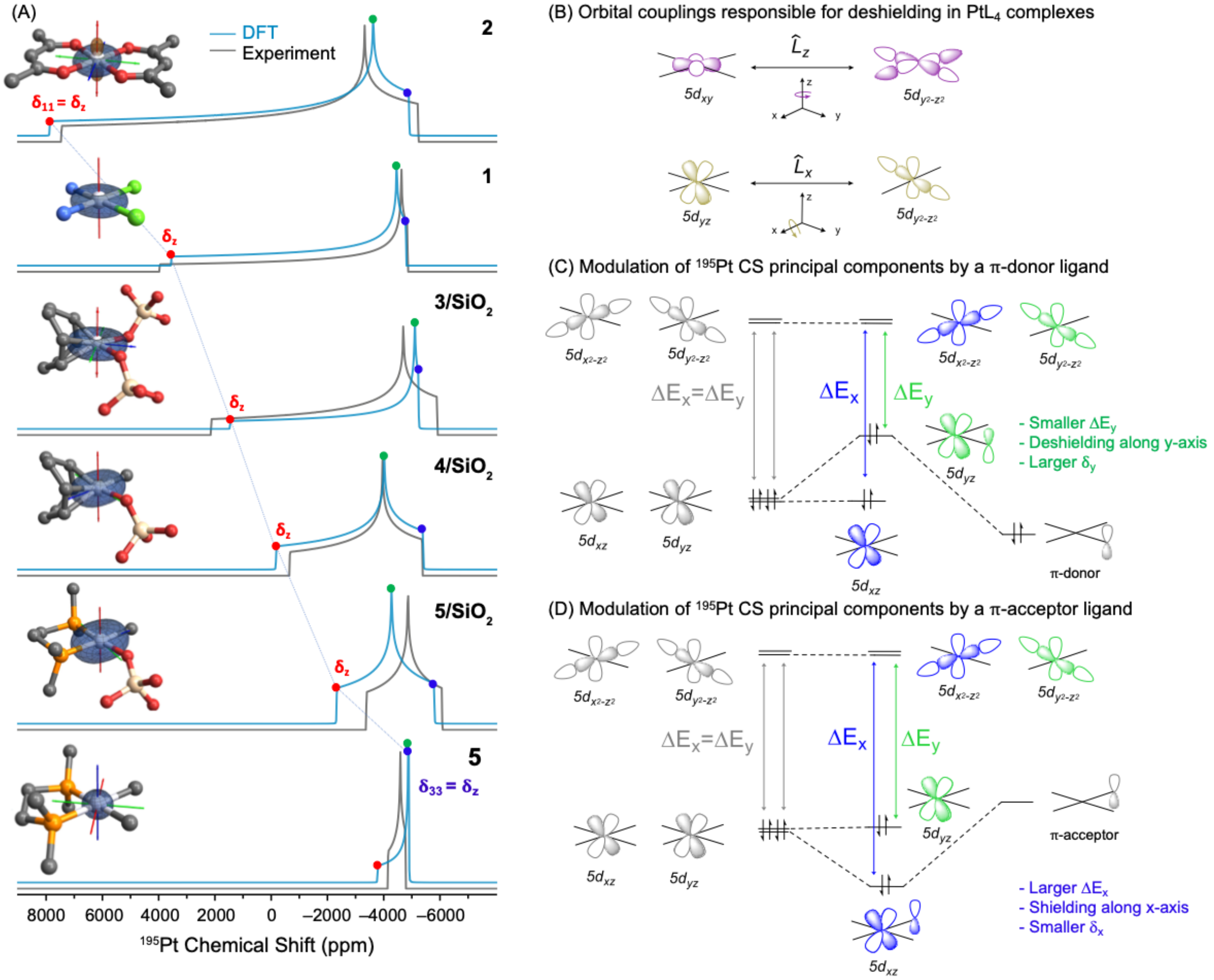

Figure 8. (A) Simulated static ^{195}Pt CSA parameters obtained using parameters from (black traces) sideband-selective NMR experiments and (blue traces) ZORA DFT calculations. The DFT optimized structures and the corresponding 3D representations of the calculated shielding tensors are shown for each compound. (B) Orbital couplings responsible for paramagnetic deshielding in square planar PtL$_4$ complexes. Modulation of orbital energies and Pt CS principal components in the plane by (C) a π-donor and (D) a π-acceptor ligand. In (A), blue and orange lobes indicate positive and negative shielding, respectively. The CSA principal components color code is: $\delta_{11} > \delta_{22} > \delta_{33}$. Plots of the shielding tensors are scaled to 0.002 pm/ppm. A summary of ^{195}Pt CSA parameters from different methods are provided in the Supporting Information in Table S2. NMR calculations of the supported species were performed using with *t*-butoxy siloxide groups in place of the silica surface. Hydrogen atoms are omitted for clarity. For the same reason, only the SiO$_4$ unit of the siloxide ligands is shown

DFT Calculations of ^{195}Pt CS Tensors. Finally, we used ZORA DFT calculations to compute the ^{195}Pt CS tensor parameters of the molecular and supported Pt-species studied. The differences in CSA parameters can be related to differences in the coordination environments using simple and powerful orbital models. Modern computational chemistry packages allow accurate prediction of NMR properties, including ^{195}Pt chemical shifts,[58-59, 93] which is useful for structure determination by NMR crystallography protocols.[55, 94-95] As demonstrated earlier by Ziegler, the origin of the ^{195}Pt CSA can be traced back to electronic structure.[96] Autschbach subsequently demonstrated a localized molecular orbital analysis of ^{195}Pt CS tensors that provides a clear link between the energy and symmetry of orbitals in square planar Pt compounds and the observed CS tensor parameters:[55, 59] the deshielding for the CS component along the *z* direction of the molecular frame (denoted δ_z), originate from the coupling of the high-lying, filled d_{xy} orbital with the antibonding σ *(Pt-L) orbital by the $\hat{L}_z$ operator and, to a minor extent, from the filled d_{xz} and d_{yz} Pt orbitals coupling with the specific σ *(Pt-L) along the y or x axis, by $\hat{L}_y$ and $\hat{L}_x$ respectively (Figure 8B, details in experimental section below).

First, standard gas-phase DFT calculations using the Gaussian09 program[97] were used to optimize atomic coordinates. Then, ZORA DFT calculations as implemented in the ADF program[98] were used to calculate ^{195}Pt CSA principal components ($\delta_{11} > \delta_{22} > \delta_{33}$) and CS tensor parameters. Additional details are provided in the experimental section. The computed and experimental values of CSA are compared in Figure 8A and Table S2 showing a good agreement and thus validating the computational approach.

In all but one cases, δ_{11}, the most deshielded component, lies perpendicular to the plane, along the natural *z*-axis of these square planar compounds ($\delta_{11} = \delta_z$). The exception is for compound **5**, where δ_{33} is aligned with the molecular *z*-axis. Across the series of square planar compounds studied here, the value of δ_z varies from +7873 to –4885 ppm, while the other components in the plane (δ_x/δ_z), varies only within ca. 2000 ppm. Note also that small changes in geometry greatly affect ^{195}Pt CS tensor parameters (Figure S31).

The (de)shielding across the series of Pt-species studied in our work is clearly affected by the energy of σ*(Pt-L) orbitals, which is determined by the σ-donating properties of the corresponding L ligands (Note S3). Thus, it may not be so surprising that changes in the coordination sphere of $Pt^{II}L_4$ compounds dramatically affect the δ_z component, which varies from +7873 (**2**) to –4885 ppm (**5**) upon going from oxygen to carbon-based ligands. As discussed above, the compound **5** presents the most shielded value for δ_z that correspond to δ_{33} and not δ_{11} as for the other compounds discussed here. Using the orbital-rotation model (Figure 8B, details in SI), one can readily justify the much more shielded value for δ_z in **5**; in this molecule there are four strong σ-donor ligands bound to Pt (two methyl and two phosphine) which increases the energy of the σ *(Pt-L) orbital, leading to a high shielding of the Pt nucleus. At the opposite end, the compound **2** has four weak σ-donor oxygen atoms from the acac ligands coordinated to Pt, leading to a lower energy σ *(Pt-L) orbital, more deshielding and a more positive value of δ_z. Overall, the strength of the σ-donating ligands drives the value of δ_z and determine the overall anisotropy and isotropic CS.

The sensitivity of the CS tensor parameters to the types of coordinated ligands explains why **5** and the supported **5/SiO$_2$** have significantly different spans (Figure 8A). The replacement of Pt-methyl bond in **5** by a Pt-siloxide bond in **5/SiO$_2$** upon grafting, leads to a more deshielded δ_z component, as a result of the overall lower σ-donating properties of the siloxide ligand. This analysis also proves suitable to understand the differences in spans among supported Pt sites. For the supported species **3/SiO$_2$** and **4/SiO$_2$** the latter has a more shielded δ_z component, resulting from the presence of a methyl group, a strong σ-donor ligand. A remarkable difference in δ_z can also be observed between **4/SiO$_2$** and **5/SiO$_2$**, where a more shielded δ_z in the latter can be related to the stronger σ-donating properties of DMPE with respect to the COD ligand.

Although CSA parameters in square planar $Pt^{II}L_4$ complexes are mostly affected by σ-interactions, the other principal components lying in the plane can be modulated through π-bonding interactions. These effects are observed upon comparison of **3/SiO$_2$** with the respective asymmetric complex **4/SiO$_2$**. While the symmetric molecular model for **3/SiO$_2$** (having two siloxide ligands) has an axially symmetric CS tensor ($\delta_{22} \approx \delta_{33} \approx -5150$ ppm), the asymmetric system **4/SiO$_2$**, with both a siloxide (weak π-donor) and a methyl ligand (mostly σ-donor) has δ_{22} (–4021 ppm) >> δ_{33} (–5400 ppm). In **4/SiO$_2$**, the most shielded component δ_{33} is aligned with the Pt-methyl bond, while δ_{22} is aligned with the Pt-siloxide bond. Specifically, the presence of a π-donor ligand causes an increase in energy of the overlapping filled Pt $5d_{yz}$ orbital through an antibonding interaction, which ultimately results in an increased energy of the $5d_{yz}$ orbital that allows for a more efficient coupling with σ *(Pt-L), hence the observed deshielding in the direction of the coupling (Figure 8C). On the contrary, a π-acceptor ligand can interact with the filled Pt $5d_{yz}$ orbital, stabilising it, and resulting in a less efficient orbital coupling due to increase in energy difference with the antibonding σ *(Pt-L) (Figure 8D). When combined, these orbital interactions lead to the observed effects in CSA of the asymmetric system **4/SiO$_2$**; analogous observations can be made for **5/SiO$_2$**.

In summary, ^{195}Pt solid-state NMR spectra and CSA provide a signature of the metal sites, the types of ligands and the local symmetry of organometallic complexes and supported Pt species; hence ^{195}Pt solid-state NMR spectroscopy is a powerful tool to characterize compounds and surface sites. Besides, with this knowledge in hand, ^{195}Pt NMR together with chemical shift tensor analysis could be used to determine the unknown geometry of industry-relevant Pt catalysts, and to correlate their spectroscopic signature with catalytic activity.

Conclusions

In conclusion, we have developed robust and expedient sideband-selective solid-state NMR methods to rapidly measure the spectroscopic (^{195}Pt NMR) signatures of Pt-containing compounds and materials, including some having very large anisotropy, e.g. Pt(acac)$_2$. The sideband-selective NMR experiments offer an enormous time saving in comparison to state-of-the-art static DNP SENS experiments.[66] Additionally, the sideband-selective NMR methods can be performed at room temperature and require only a few mg of material when performed with fast MAS probes and small diameter rotors. These methods are based on low-power, rectangular pulses that provide sideband-selective excitation or saturation in fast MAS ^{1}H{^{195}Pt} TONE D-HMQC-4 and PE RESPDOR experiments, thus allowing the reconstruction of ^{195}Pt sideband manifolds from a series of 1D NMR spectra. This approach was also extended to sensitive spy nuclei such as ^{31}P for indirect detection in sideband-selective ^{31}P{^{195}Pt} *J*-resolved experiments, thus showing that, even in the absence of ^{1}H in the materials, other widely abundant NMR active spy nuclei can be utilized to obtain valuable molecular-level information on metal sites. Furthermore, natural chemical shift analysis of the CSA patterns down to the nature of the Pt-bonded ligands (σ-donor strength and π-donating/accepting ability) enables to understand the trends of NMR signatures and also demonstrates the potential of Pt NMR spectroscopy to distinguish subtle differences in the Pt-coordination sphere. With this methodology in hand, we are currently exploring structure-reactivity relationships in Pt-based single-atom catalysts, and are also investigating their applications to other high *Z* spin-1/2 nuclei with moderate isotopic abundance that exhibit large CSA. Finally, combining the sideband-selective NMR experiments with DNP should offer further gains in sensitivity that will be needed to study dilute single-atom catalysts or enable the use of nuclei such as natural abundance ^{13}C as a spy-nucleus.

Experimental Section

Synthesis of Materials. All experiments were conducted inside an Argon filled MBraun GloveBox or using standard Schlenk technique, using anhydrous reagents and distilled solvents, unless indicated otherwise. All solvents were stored over 4 Å molecular sieves after being transferred to a glove box. Silica (SiO_2, Aerosil 200®, 200 m^2 g^{-1}) was calcined in air at 500°C before subsequent dehydroxylation at 700°C under high vacuum as reported in literature.[10] The resulting dehydroxylated silica is referred to as SiO_{2-700}. Titration of the resulting SiO_{2-700} using $[Mg(CH_2Ph)_2(THF)_2]$ purified *via* sublimation prior to use,[99] yielded an Si−OH density of 0.3 mmol/g, corresponding to 0.9 accessible Si−OH groups per nm^2. $PtCl_2(NH_3)_2$ (**1**, 99 % purity, Alfa Aesar) and $Pt(acac)_2$ (**2**, 98 % purity, Strem Chemicals) were used as received. $[(COD)Pt(OSi(O^tBu)_3)_2]$ (**3**), $[(COD)PtMe(OSi(O^tBu)_3)]$ (**4**), $[(DMPE)PtMe_2]$ (**5**), $[Zn(OSi(OtBu)_3)_2]_2$ and $[Ga(THF)(OSi(OtBu)_3)_3]$ molecular precursors were synthesized *via* literature procedures with minor modifications.[12, 91, 100-102] $[(COD)Pt(OSi(OtBu)_3)]/SiO_2$ (**3/SiO$_2$**) was synthesized according to the previously described procedure.[66] The materials $[(COD)Pt(OSi(OtBu)_3)]\_Zn^{II}/SiO_2$ (**3_Zn/SiO$_2$**), $[(COD)Pt(OSi(OtBu)_3)]\_Ga^{III}/SiO_2$ (**3_Ga/SiO$_2$**) and $[(COD)PtMe]/SiO_{2-700}$ (**4/SiO$_2$**) were synthesized following adapted literature procedures.[12-13, 15]

$[(COD)Pt(OSi(OtBu)_3)]\_Zn^{II}/SiO_2$ (3_Zn/SiO$_2$): A colourless solution of $[Zn(OSi(OtBu)_3)_2]_2$ (0.234 g, 0.395 mmol) in benzene (10 ml) was added slowly to a suspension of SiO_{2-700} (1.517 g, 0.455 mmol -OH) in benzene (10 ml) while stirring (100 rpm). The resulting suspension was stirred for 5 h at room temperature. The supernatant was removed, and the material washed with benzene (10 ml) three times to wash off unreacted complex. The material was then washed with pentane and subsequently dried under high vacuum (10^{-5} mbar) for 3 h to remove residual solvent. The resulting white solid was then transferred to a tubular quartz reactor and treated under high vacuum (10^{-5} mbar) at high temperature (r.t. to 300 °C (5 °C/min) for 1 h, 400 °C (5 °C/min) for 1 h, 500 °C (5 °C/min) for 1 h, 600 °C (5 °C/min) for 8 h). Part of the resulting white solid (1.193 g, 0.358 mmol –OH assumed) was suspended in benzene (10 ml), and a colourless solution of **3** (0.258 g, 0.311 mmol) in benzene (10 ml) added to it slowly while stirring (100 rpm). The resulting suspension was stirred for 4 h at room temperature. The supernatant was removed, and the material washed with benzene (10 ml) three times to wash off unreacted complex. The material was then washed with pentane and subsequently dried under high vacuum (10^{-5} mbar) for 3 h to remove residual solvent. **3_Zn/SiO$_2$** was obtained as a white solid. Elemental Analysis: 2.77 wt.% Pt, 1.48 wt.% Zn.

[(COD)Pt(OSi(OtBu)$_3$)]_Ga^{III}/SiO$_{2\text{-}700}$ (3_Ga/SiO$_2$): A colourless solution of [Ga(THF)(OSi(OtBu)$_3$)$_3$] (0.245 g, 0.263 mmol) in benzene (10 ml) was added slowly to a suspension of SiO$_{2\text{-}700}$ (1.009 g, 0.303 mmol -OH) in benzene (10 ml) while stirring (100 rpm). The resulting suspension was stirred for 12 h at room temperature. The supernatant was removed, and the material washed with benzene (10 ml) three times to wash off unreacted complex. The material was then washed with pentane and subsequently dried under high vacuum (10^{-5} mbar) for 5 h to remove residual solvent. The resulting white solid was then transferred to a tubular quartz reactor and treated under high vacuum (10^{-5} mbar) at high temperature (r.t. to 300 °C (5 °C/min) for 1 h, 400 °C (5 °C/min) for 1 h, 500 °C (5 °C/min) for 1 h, 600 °C (5 °C/min) for 8 h). Part of the resulting grey solid (0.480 g, 0.144 mmol –OH assumed) was suspended in benzene (10 ml), and a colourless solution of **3** (0.104 g, 0.125 mmol) in benzene (10 ml) added to it slowly while stirring (100 rpm). The resulting suspension was stirred for 12 h at room temperature. The supernatant was removed, and the material washed with benzene (10 ml) three times to wash off unreacted complex. The material was then washed with pentane and subsequently dried under high vacuum (10^{-5} mbar) for 3 h to remove residual solvent. **3_Ga/SiO$_2$** was obtained as a white solid.

[(COD)PtMe]/SiO$_{2\text{-}700}$ (4/SiO$_2$): A colourless solution of **4** (0.087 g, 0.15 mmol) in benzene (10 mL) was added slowly to a suspension of SiO$_{2-700}$ (0.500 g, 0.15 mmol −OH) in benzene (10 mL) while stirring (100 rpm). The resulting suspension was stirred for 12 h at room temperature. The supernatant was removed, and the material washed with benzene (10 mL) three times to wash off unreacted complex. The material was then washed with pentane and dried under high vacuum (10^{-5} mbar) for 4 h to remove residual solvent. **4/SiO$_2$** was obtained as a white solid. Elemental analysis: Pt, 4.96 wt. %.

[(DMPE)PtMe]/SiO$_{2\text{-}700}$ (5/SiO$_2$): A suspension of off-white/brown **5** (0.035 g, 0.093 mmol) in benzene (10 mL) was added slowly to a suspension of SiO$_{2-700}$ (0.311 g, 0.093 mmol −OH) in benzene (10 mL) while stirring (100 rpm). The resulting suspension was stirred for 12 h at room temperature with gradual disappearance of **5** in the suspension. The supernatant was removed, and the material washed with benzene (10 mL) three times to wash off unreacted complex. The material was then washed with pentane and dried under high vacuum (10^{-5} mbar) for 2 h to remove residual solvent. **5/SiO$_2$** was obtained as a white solid. Elemental analysis: 4.39 wt.% Pt; 1.35 wt.% P.

Molecular DFT Calculations. Atomic coordinates were optimized with DFT using Gaussian09.[97] Geometry optimizations were performed using the B3LYP functional[103] in combination with Pople's 6-31G(d) basis sets for H, C, Si atoms and 6-31+G(d) for negatively charged atoms (P, O).[104] The Los Alamos LANL2TZ basis set was used for Pt atoms in conjunction with the associated pseudopotential.[105] NMR calculations were performed using ADF 2016 with the PBE0 functional and Slater-type basis sets of quadruple-ζ quality (QZ4P) for Pt and triple-ζ quality (TZP) for other atoms.[98] Relativistic effects were treated by the 2-component zeroth order regular approximation (ZORA).[106] The calculated ^{195}Pt chemical shifts were referenced to (COD)$PtCl_2$, with an experimental isotropic chemical shift of −3360 ppm, and a calculated isotropic shielding of 5483 ppm. Calculated shielding tensors are plotted as 3D representations of $\sum_{ij} r_i s_{ij} r_j$, polar functions with scaling factors adjusted towards the best readability.[107]

While the chemical shift (δ) is always reported with respect to a reference compound, DFT calculations output the magnetic shielding with respect to the bare nucleus (σ); the equation below is used to convert calculated shielding values to chemical shift values, which are ordered so that $\delta_{11} > \delta_{22} > \delta_{33}$.

$$\begin{pmatrix} \delta_{11} & 0 & 0 \\ 0 & \delta_{22} & 0 \\ 0 & 0 & \delta_{33} \end{pmatrix} = \sigma_{\mathrm{iso}}^{\mathrm{ref}} \begin{pmatrix} 1 & 0 & 0 \\ 0 & 1 & 0 \\ 0 & 0 & 1 \end{pmatrix} - \begin{pmatrix} \sigma_{11} & 0 & 0 \\ 0 & \sigma_{22} & 0 \\ 0 & 0 & \sigma_{33} \end{pmatrix} \quad (1)$$

Plane-wave DFT Calculations. The hydrogen atom positions of $Pt(acac)_2$ in the previously reported crystal structure[89] were optimized using plane-wave density functional theory (DFT). The CASTEP[108] program was used with the PBE-GGA functional[109] and the TS dispersion correction scheme.[110] A k-point spacing of 0.07 Å^{-1} was used for the Monkhorst-Pack grid.

Solid-State NMR Experiments. All experiments were performed at 9.4 T using a Bruker Avance III HD console. ^{1}H, ^{31}P and ^{195}Pt chemical shifts were indirectly referenced to tetramethylsilane using the ^{1}H shift of adamantane at 1.82 ppm. Analytical simulations were performed with the TopSpin solid lineshape analysis module (sola) or ssNake *v*1.1.[111]

Fast MAS ^{1}H{^{195}Pt} Experiments. A Bruker 1.3 mm HX probe and the MAS frequency was 50 kHz unless mentioned otherwise. Cisplatin and L-histidine·HCl·H_2O were purchased and used as received from Alfa Aesar and Fluka, respectively; rotors of these samples were packed under ambient conditions. All other rotors were packed in an argon glovebox and rotors were spun with nitrogen gas. ^{1}H{^{195}Pt} TONE D-HMQC-4 and PE RESPDOR experiments were performed using $SR4_1^2$ dipolar recoupling[80] that was applied at the 2nd order R^3 condition.[112] ^{1}H 90° and 180° pulse durations of 2.5 and 5 μs, respectively were used. The ^{1}H{^{71}Ga} PE RESPDOR experiment used 30 μs ^{71}Ga saturation pulses with a 330 kHz rf field. In ^{1}H{^{195}Pt} TONE D-HMQC-4 experiments, SHAPs used tanh/tan shapes with a 20 μs duration, *ca.* 275 kHz rf field and 5 MHz sweep width. Lee-Goldburg spinlock pulses of ca. 1 ms total duration were applied at a rf field of 150 kHz at the appropriate transmitter offset frequency. For sideband-selective ^{1}H{^{195}Pt} TONE D-HMQC-4 experiments the ^{195}Pt offset for the SHAP inversion pulses was held constant, approximately in the center of NMR powder pattern, while the offset of the sideband-selective pulses was varied. For both TONE D-HMQC-4 and PE RESPDOR sideband-selective experiments the probe was not retuned for each offset. Retuning the probe was found to have a minimal effect on sideband intensities (Figure S5).

Total $SR4_1^2$ dipolar recoupling durations of 1.92 ms (**1**, TONE D-HMQC-4), 2.88 ms (**1**, PE RESPDOR), 3.2 ms (**2**, TONE D-HMQC-4 and PE RESPDOR), 1.76 ms (**3/SiO$_2$**, TONE D-HMQC-4), 2.08 ms (**3/SiO$_2$**, PE RESPDOR), 2.56 ms (**4/SiO$_2$**, TONE D-HMQC-4) and 2.4 ms (**3_Zn/SiO$_2$** and **3_Ga/SiO$_2$**, PE RESPDOR) were used in the various sideband-selective experiments. For the molecular compounds and silica-supported compounds 60 μs, 9 kHz rf field and 40 μs, 16 kHz rf field sideband-selective saturation pulses were employed, respectively. For **4/SiO$_2$** 40 μs sideband-selective pulses with a 12 kHz rf field were used. In case of **1**, although the maximum dephasing observed with PE RESPDOR was only ca. 9% with a total recoupling duration of 2.88 ms, the tolerance to MAS instability is higher at shorter recoupling durations (only

0.7% variation of the RESPDOR S_0 signal intensity was observed, which is the primary source of error in the measurements, Figure S7A). A longer recoupling duration provides more dephasing (Figure S7D) but results in a 'noisier' ^{195}Pt sideband manifold (Figure S11). Therefore, recoupling durations shorter than that providing maximal dephasing may be preferred for the variable offset PE RESPDOR experiments.

The experimental ^{195}Pt sideband-selective patterns are best reproduced by numerical simulations, as performed here using SIMPSON (*vide infra*). Alternatively, an approximate estimate of the CSA values can be obtained using Herzfeld-Berger analysis (HBA).[113-114] For example, with cisplatin, the isotropic shift was fixed to −1834 ppm while Ω and κ were fitted using the HBA program. The estimated CSA parameters for cisplatin were $\Omega = 9776$ and $\kappa = -0.65$ with TONE D-HMQC-4, and $\Omega = 9584$ and $\kappa = -0.64$ with PE RESPDOR (Figure S32). The HBA program used for fitting assumes ideal sideband intensities during fitting; however, the intensities of the ^{195}Pt pattern from the sideband-selective experiments deviate from the ideal pattern and can only be reproduced using numerical simulations. Therefore, HBA should be performed only to estimate the ^{195}Pt CSA.

^{31}P{^{195}Pt} Experiments. All experiments were performed using a Bruker 2.5 mm HXY probe. The pulse sequences used for the acquisition of ^{1}H-^{31}P{^{195}Pt} CP *J*-HMQC and sideband-selective *J*-resolved spectra are shown in Figure S27. Pulse durations of 2.5 μs ($\pi/2$, ^{1}H), 4.75 μs (π, ^{31}P) and 2-2.5 μs ($\pi/2$, ^{195}Pt) were used. The constant-time 2D ^{1}H-^{31}P{^{195}Pt} CP *J*-HMQC spectrum of **5** was acquired with 12.5 kHz MAS, 8 scans, 1.5 s recycle delay ($1.3\times T_1$), indirect spectral width of 500 kHz, 822 complex t_1-increments and a total *J*-evolution time ($2\times m\times\tau_r$) of 1.28 ms (Figure 7C). The ^{1}H→^{31}P CP duration was set to 2.5 ms and optimal ^{1}H and ^{31}P spinlock rf powers of 75 kHz and 83 kHz, respectively, were used; the ^{1}H rf power was ramped from 85-

100%. For all experiments with **5/SiO₂**, a $^{1}H \rightarrow ^{31}P$ CP duration of 5 ms and optimal ^{1}H and ^{31}P spinlock rf powers of 105 kHz and 83 kHz, respectively, were used; the ^{1}H rf power was ramped from 90-100%. The sideband-selective ^{1}H-$^{31}P\{^{195}Pt\}$ CP *J*-resolved spectra of **5/SiO₂** was acquired with 25 kHz MAS, 1800 scans and 1.5 s recycle delay per point; the total *J*-evolution time ($2 \times m \times \tau_r$) was set to 560 μs, and a 40 μs ^{195}Pt saturation pulse at 22 kHz rf was applied. The offset was incremented in steps of the MAS frequency and 21 sub-spectra were obtained. The total duration of each echo in the CPMG train was set to 800 μs and 55 spin echoes were acquired. 100 kHz SPINAL-64 decoupling was applied during *J*-evolution periods and signal acquisition.[115]

SIMPSON simulations. All $^{1}H\{^{195}Pt\}$ SIMPSON simulations were performed with a 50 kHz MAS frequency and a ^{1}H Larmor frequency of 400.498 MHz. The ^{1}H-^{195}Pt dipolar coupling was set to –3500 Hz and an optimal recoupling duration of 2.88 ms was used. For the simulations shown in Figure 2, the rep168 crystal file and 24 gamma angles were used for powder averaging. For all other simulations in the main text, the rep320 crystal file and 13 gamma angles were used. 60 μs selective excitation pulses with an optimized 9 kHz rf field were used in the simulations for all molecular compounds, whereas shorter 40 μs duration pulses at 16 kHz rf were used for the surface compounds. The rf fields for the sideband-selective excitation pulses in D-HMQC were optimized in both simulations and experiments (Table S1). Note, the selectivity of the pulses can be tuned by adjusting the length of the excitation/saturation pulse, with longer pulses being more selective, as expected (Table S1, Figure S3-S4). In all cases, the offset frequency of a sideband was determined by first varying the offset in small steps of 1-2 kHz, followed by stepping the transmitter offset in steps equal to the MAS frequency. Note that the TONE D-HMQC-2 sequence was used for SIMPSON simulations throughout this work, while TONE D-HMQC-4 was used for experiments. TONE D-HMQC-2 was used for simulations because TONE D-HMQC-4 relies on experimental rf inhomogeneity, which is absent in the simulations, to dephase uncorrelated signals.[83] The sideband-selective $^{31}P\{^{195}Pt\}$ *J*-resolved experiments with **5/SiO₂** were simulated using a ^{31}P-^{195}Pt J-coupling of 1825 Hz, a *J*-evolution time of 560 μs, and a 25 kHz MAS frequency as in the experiments.

Plots showing the root mean square deviation (RMSD) between experimental and simulated patterns are provided in the SI for all samples. Briefly, the sideband NMR spectra were fit with the following procedure: (i) visual inspection of the sideband manifold provides a preliminary estimate of the principal components of the CSA tensor, (ii) the skew of the CS tensor was fixed while the span was varied and (iii) finally, the span with the lowest RMSD was fixed and the skew was varied to determine the best fit.

Acknowledgements

This work was primarily supported by a grant from the National Science Foundation CBET-1916809 to AJR. The development of sideband-selective NMR methods was supported by the U.S. Department of Energy (DOE), Office of Science, Basic Energy Sciences, Materials Science and Engineering Division. The Ames Laboratory is operated for the U.S. DOE by Iowa State University under contract # DE-AC02-07CH11358. AJR acknowledges additional support from the Alfred P. Sloan Foundation through a Sloan research fellowship. The research carried out at ETH Zürich was partially funded by the Swiss National Science Foundation (Grant number 200021_169134 and 200020B_192050). This work is part of a project that has received funding from the European Union's Horizon 2020 research and innovation programme under Grant Agreement No 101008500 ("PANACEA"). This work is also supported by the Common Research Laboratory CARMEN (ENS de Lyon, CNRS, IFPEN, Claude Bernard Lyon 1 University, Sorbonne University, and University of Strasbourg). We are grateful to Ribal Jabbour for his help with the setup of static ^{195}Pt solid-state NMR experiments.

Supporting Information

Additional experimental and simulated NMR spectra, tables and experimental details can be found in the supporting information.

References

1. Bowker, M. *The Basis and Applications of Heterogeneous Catalysis*. Oxford University Press: Oxford, 1998.
2. Fechete, I.; Wang, Y.; Vedrine, J. C. The past, present and future of heterogeneous catalysis. *Catal Today* **2012,** *189* (1), 2-27.
3. Friend, C. M.; Xu, B. J. Heterogeneous Catalysis: A Central Science for a Sustainable Future. *Acc. Chem. Res.* **2017,** *50* (3), 517-521.
4. Coperet, C. Fuels and energy carriers from single-site catalysts prepared via surface organometallic chemistry. *Nat. Energy* **2019,** *4* (12), 1018-1024.
5. Tennakoon, A.; Wu, X.; Paterson, A. L.; Patnaik, S.; Pei, Y. C.; LaPointe, A. M.; Ammal, S. C.; Hackler, R. A.; Heyden, A.; Slowing, I. I.; Coates, G. W.; Delferro, M.; Peters, B.; Huang, W. Y.; Sadow, A. D.; Perras, F. A. Catalytic upcycling of high-density polyethylene via a processive mechanism. *Nat. Catal.* **2020,** *3* (11), 893-901.
6. Thomas, J. M.; Raja, R.; Lewis, D. W. Single-site heterogeneous catalysts. *Angew. Chem. Int. Ed.* **2005,** *44* (40), 6456-6482.
7. Korzyński, M. D.; Copéret, C. Single sites in heterogeneous catalysts: separating myth from reality. *Trends Chem.* **2021**.
8. Wang, A. Q.; Li, J.; Zhang, T. Heterogeneous Single-Atom Catalysis. *Nat. Rev. Chem.* **2018,** *2* (6), 65-81.
9. Wegener, S. L.; Marks, T. J.; Stair, P. C. Design Strategies for the Molecular Level Synthesis of Supported Catalysts. *Acc. Chem. Res.* **2012,** *45* (2), 206-214.
10. Coperet, C.; Comas-Vives, A.; Conley, M. P.; Estes, D. P.; Fedorov, A.; Mougel, V.; Nagae, H.; Nunez-Zarur, F.; Zhizhko, P. A. Surface Organometallic and Coordination Chemistry toward Single-Site Heterogeneous Catalysts: Strategies, Methods, Structures, and Activities. *Chem. Rev.* **2016,** *116* (2), 323-421.
11. Pelletier, J. D. A.; Basset, J. M. Catalysis by Design: Well-Defined Single-Site Heterogeneous Catalysts. *Acc. Chem. Res.* **2016,** *49* (4), 664-677.
12. Laurent, P.; Veyre, L.; Thieuleux, C.; Donet, S.; Coperet, C. From Well-Defined Pt(II) Surface Species to the Controlled Growth of Silica Supported Pt Nanoparticles. *Dalton Trans.* **2013,** *42* (1), 238-248.
13. Searles, K.; Chan, K. W.; Burak, J. A. M.; Zemlyanov, D.; Safonova, O.; Coperet, C. Highly Productive Propane Dehydrogenation Catalyst Using Silica-Supported Ga-Pt Nanoparticles Generated from Single-Sites. *J. Am. Chem. Soc.* **2018,** *140* (37), 11674-11679.
14. Coperet, C. Single-Sites and Nanoparticles at Tailored Interfaces Prepared via Surface Organometallic Chemistry from Thermolytic Molecular Precursors. *Acc. Chem. Res.* **2019,** *52* (6), 1697-1708.
15. Rochlitz, L.; Searles, K.; Alfke, J.; Zemlyanov, D.; Safonova, O. V.; Coperet, C. Silica-Supported, Narrowly Distributed, Subnanometric Pt-Zn Particles from Single Sites with High Propane Dehydrogenation Performance. *Chem. Sci.* **2020,** *11* (6), 1549-1555.
16. Payard, P. A.; Rochlitz, L.; Searles, K.; Foppa, L.; Leuthold, B.; Safonova, O. V.; Comas-Vives, A.; Copéret, C. Dynamics and Site Isolation: Keys to High Propane Dehydrogenation Performance of Silica-Supported PtGa Nanoparticles. *JACS Au* **2021**.
17. Zhang, W. P.; Xu, S. T.; Han, X. W.; Bao, X. H. In Situ Solid-State NMR for Heterogeneous Catalysis: A Joint Experimental and Theoretical Approach. *Chem. Soc. Rev.* **2012,** *41* (1), 192-210.
18. D'Elia, V.; Dong, H. L.; Rossini, A. J.; Widdifield, C. M.; Vummaleti, S. V. C.; Minenkov, Y.; Poater, A.; Abou-Hamad, E.; Pelletier, J. D. A.; Cavallo, L.; Emsley, L.; Basset, J. M. Cooperative Effect of Monopodal Silica-Supported Niobium Complex Pairs Enhancing Catalytic Cyclic Carbonate Production. *J. Am. Chem. Soc.* **2015,** *137* (24), 7728-7739.
19. Kobayashi, T.; Perras, F. A.; Slowing, I. I.; Sadow, A. D.; Pruski, M. Dynamic Nuclear Polarization Solid-State NMR in Heterogeneous Catalysis Research. *ACS Catal.* **2015,** *5* (12), 7055-7062.

20. Coperet, C.; Liao, W. C.; Gordon, C. P.; Ong, T. C. Active Sites in Supported Single-Site Catalysts: An NMR Perspective. *J. Am. Chem. Soc.* **2017,** *139* (31), 10588-10596.

21. Vancompernolle, T.; Trivelli, X.; Delevoye, L.; Pourpoint, F.; Gauvin, R. M. On the use of Solid-State ^{45}Sc NMR for Structural Investigations of Molecular and Silica-Supported Scandium Amide Catalysts. *Dalton Trans.* **2017,** *46* (39), 13176-13179.

22. Grekov, D.; Vancompernolle, T.; Taoufik, M.; Delevoye, L.; Gauvin, R. M. Solid-State NMR of Quadrupolar Nuclei for Investigations into Supported Organometallic Catalysts: Scope and Frontiers. *Chem. Soc. Rev.* **2018,** *47* (8), 2572-2590.

23. Culver, D. B.; Venkatesh, A.; Huynh, H.; Rossini, A. J.; Conley, M. P. Al(OR^F)$_3$ (R^F = C(CF$_3$)$_3$) Activated Silica: A Well-Defined Weakly Coordinating Surface Anion. *Chem. Sci.* **2020,** *11* (6), 1510-1517.

24. Berruyer, P.; Lelli, M.; Conley, M. P.; Silverio, D. L.; Widdifield, C. M.; Siddiqi, G.; Gajan, D.; Lesage, A.; Coperet, C.; Emsley, L. Three-Dimensional Structure Determination of Surface Sites. *J. Am. Chem. Soc.* **2017,** *139* (2), 849-855.

25. Perras, F. A.; Paterson, A. L.; Syed, Z. H.; Kropf, A. J.; Kaphan, D. M.; Delferro, M.; Pruski, M. Revealing the Configuration and Conformation of Surface Organometallic Catalysts with DNP-Enhanced NMR. *J. Phys. Chem. C* **2021,** *125* (24), 13433-13442.

26. Zilm, K. W.; Conlin, R. T.; Grant, D. M.; Michl, J. Low-Temperature Natural-Abundance Carbon-13 NMR Spectroscopy of Matrix-Isolated Species - Anisotropy of Shielding Tensor in Ethylene. *J. Am. Chem. Soc.* **1978,** *100* (25), 8038-8039.

27. Widdifield, C. M.; Schurko, R. W. Understanding Chemical Shielding Tensors Using Group Theory, MO Analysis, and Modern Density-Functional Theory. *Concepts Magn. Reson. Part A* **2009,** *34a* (2), 91-123.

28. Facelli, J. C. Chemical shift tensors: Theory and application to molecular structural problems. *Prog. Nucl. Magn. Reson. Spectrosc.* **2011,** *58* (3-4), 176-201.

29. Gordon, C. P.; Raynaud, C.; Andersen, R. A.; Coperet, C.; Eisenstein, O. Carbon-13 NMR Chemical Shift: A Descriptor for Electronic Structure and Reactivity of Organometallic Compounds. *Acc. Chem. Res.* **2019,** *52* (8), 2278-2289.

30. Halbert, S.; Coperet, C.; Raynaud, C.; Eisenstein, O. Elucidating the Link between NMR Chemical Shifts and Electronic Structure in d(0) Olefin Metathesis Catalysts. *J. Am. Chem. Soc.* **2016,** *138* (7), 2261-2272.

31. Lummiss, J. A. M.; Perras, F. A.; McDonald, R.; Bryce, D. L.; Fogg, D. E. Sterically Driven Olefin Metathesis: The Impact of Alkylidene Substitution on Catalyst Activity. *Organometallics* **2016,** *35* (5), 691-698.

32. Yamamoto, K.; Gordon, C. P.; Liao, W. C.; Coperet, C.; Raynaud, C.; Eisenstein, O. Orbital Analysis of Carbon-13 Chemical Shift Tensors Reveals Patterns to Distinguish Fischer and Schrock Carbenes. *Angew. Chem. Int. Ed.* **2017,** *56* (34), 10127-10131.

33. Culver, D. B.; Huynh, W.; Tafazolian, H.; Ong, T. C.; Conley, M. P. The beta-Agostic Structure in $(C_5Me_5)_2Sc(CH_2CH_3)$: Solid-State NMR Studies of $(C_5Me_5)_2$Sc-R (R=Me, Ph, Et). *Angew. Chem. Int. Ed.* **2018,** *57* (30), 9520-9523.

34. Hillenbrand, J.; Leutzsch, M.; Gordon, C. P.; Coperet, C.; Furstner, A. ^{183}W NMR Spectroscopy Guides the Search for Tungsten Alkylidyne Catalysts for Alkyne Metathesis. *Angew. Chem. Int. Ed.* **2020,** *59* (48), 21758-21768.

35. Pietrasiak, E.; Gordon, C. P.; Coperet, C.; Togni, A. Understanding ^{125}Te NMR chemical shifts in Disymmetric Organo-Telluride Compounds from Natural Chemical Shift Analysis. *Phys. Chem. Chem. Phys.* **2020,** *22* (4), 2319-2326.

36. Arduengo, A. J.; Dixon, D. A.; Kumashiro, K. K.; Lee, C.; Power, W. P.; Zilm, K. W. Chemical Shielding Tensor of a Carbene. *J. Am. Chem. Soc.* **1994,** *116* (14), 6361-6367.

37. Vummaleti, S. V. C.; Nelson, D. J.; Poater, A.; Gomez-Suarez, A.; Cordes, D. B.; Slawin, A. M. Z.; Nolan, S. P.; Cavallo, L. What can NMR Spectroscopy of Selenoureas and Phosphinidenes Teach us About the Pi-Accepting Abilities of N-heterocyclic Carbenes? *Chem. Sci.* **2015,** *6* (3), 1895-1904.

38. Engl, P. S.; Santiago, C. B.; Gordon, C. P.; Liao, W. C.; Fedorov, A.; Coperet, C.; Sigman, M. S.; Togni, A. Exploiting and Understanding the Selectivity of Ru-N-Heterocyclic Carbene Metathesis Catalysts for the Ethenolysis of Cyclic Olefins to alpha,omega-Dienes. *J. Am. Chem. Soc.* **2017,** *139* (37), 13117-13125.

39. Taoufik, M.; Szeto, K. C.; Merle, N.; Del Rosal, I.; Maron, L.; Trebosc, J.; Tricot, G.; Gauvin, R. M.; Delevoye, L. Heteronuclear NMR Spectroscopy as a Surface-Selective Technique: A Unique Look at the Hydroxyl Groups of gamma-Alumina. *Chem. Eur. J.* **2014,** *20* (14), 4038-4046.

40. Mance, D.; Comas-Vives, A.; Coperet, C. Proton-Detected Multidimensional Solid-State NMR Enables Precise Characterization of Vanadium Surface Species at Natural Abundance. *J. Phys. Chem. Lett.* **2019,** *10* (24), 7898-7904.

41. Love, A. M.; Cendejas, M. C.; Hanrahan, M. P.; Carnahan, S. L.; Uchupalanun, P.; Rossini, A. J.; Hermans, I. Understanding the Synthesis of Supported Vanadium Oxide Catalysts Using Chemical Grafting. *Chem. Eur. J.* **2020,** *26* (5), 1052-1063.

42. Corma, A.; Nemeth, L. T.; Renz, M.; Valencia, S. Sn-zeolite Beta as a Heterogeneous Chemoselective Catalyst for Baeyer-Villiger Oxidations. *Nature* **2001,** *412* (6845), 423-5.

43. Merle, N.; Trebosc, J.; Baudouin, A.; Rosal, I. D.; Maron, L.; Szeto, K.; Genelot, M.; Mortreux, A.; Taoufik, M.; Delevoye, L.; Gauvin, R. M. ^{17}O NMR gives Unprecedented Insights into the Structure of Supported Catalysts and their Interaction with the Silica Carrier. *J. Am. Chem. Soc.* **2012,** *134* (22), 9263-75.

44. Gunther, W. R.; Michaelis, V. K.; Caporini, M. A.; Griffin, R. G.; Roman-Leshkov, Y. Dynamic Nuclear Polarization NMR Enables the Analysis of Sn-Beta Zeolite Prepared with Natural Abundance ^{119}Sn Precursors. *J. Am. Chem. Soc.* **2014,** *136* (17), 6219-22.

45. Delley, M. F.; Lapadula, G.; Nunez-Zarur, F.; Comas-Vives, A.; Kalendra, V.; Jeschke, G.; Baabe, D.; Walter, M. D.; Rossini, A. J.; Lesage, A.; Emsley, L.; Maury, O.; Coperet, C. Local Structures and Heterogeneity of Silica-Supported M(III) Sites Evidenced by EPR, IR, NMR, and Luminescence Spectroscopies. *J. Am. Chem. Soc.* **2017,** *139* (26), 8855-8867.

46. Camacho-Bunquin, J.; Ferrandon, M.; Sohn, H.; Yang, D. L.; Liu, C.; Ignacio-de Leon, P. A.; Perras, F. A.; Pruski, M.; Stair, P. C.; Delferro, M. Chemoselective Hydrogenation with Supported Organoplatinum(IV) Catalyst on Zn(II)-Modified Silica. *J. Am. Chem. Soc.* **2018,** *140* (11), 3940-3951.

47. Perras, F. A.; Boteju, K. C.; Slowing, II; Sadow, A. D.; Pruski, M. Direct ^{17}O Dynamic Nuclear Polarization of Single-Site Heterogeneous Catalysts. *Chem. Commun.* **2018,** *54* (28), 3472-3475.

48. Nagashima, H.; Trebosc, J.; Kon, Y.; Sato, K.; Lafon, O.; Amoureux, J. P. Observation of Low-gamma Quadrupolar Nuclei by Surface-Enhanced NMR Spectroscopy. *J. Am. Chem. Soc.* **2020,** *142* (24), 10659-10672.

49. Ishizaka, Y.; Arai, N.; Matsumoto, K.; Nagashima, H.; Takeuchi, K.; Fukaya, N.; Yasuda, H.; Sato, K.; Choi, J. C. Bidentate Disilicate Framework for Bis-Grafted Surface Species. *Chem. Eur. J.* **2021,** *27* (47), 12069-12077.

50. Fu, Q.; Saltsburg, H.; Flytzani-Stephanopoulos, M. Active Nonmetallic Au and Pt Species on Ceria-based Water-Gas Shift Catalysts. *Science* **2003,** *301* (5635), 935-938.

51. Vajda, S.; Pellin, M. J.; Greeley, J. P.; Marshall, C. L.; Curtiss, L. A.; Ballentine, G. A.; Elam, J. W.; Catillon-Mucherie, S.; Redfern, P. C.; Mehmood, F.; Zapol, P. Subnanometre Platinum Clusters as Highly Active and Selective Catalysts for the Oxidative Dehydrogenation of Propane. *Nat. Mater.* **2009,** *8* (3), 213-216.

52. Qiao, B. T.; Wang, A. Q.; Yang, X. F.; Allard, L. F.; Jiang, Z.; Cui, Y. T.; Liu, J. Y.; Li, J.; Zhang, T. Single-atom catalysis of CO oxidation using Pt-1/FeOx. *Nat. Chem.* **2011,** *3* (8), 634-641.

53. MacGregor, A. W.; O'Dell, L. A.; Schurko, R. W. New Methods for the Acquisition of Ultra-Wideline Solid-State NMR Spectra of Spin-1/2 Nuclides. *J. Magn. Reson.* **2011,** *208* (1), 103-113.

54. Schurko, R. W. Ultra-Wideline Solid-State NMR Spectroscopy. *Acc. Chem. Res.* **2013,** *46* (9), 1985-1995.

55. Lucier, B. E. G.; Johnston, K. E.; Xu, W. Q.; Hanson, J. C.; Senanayake, S. D.; Yao, S. Y.; Bourassa, M. W.; Srebro, M.; Autschbach, J.; Schurko, R. W. Unravelling the Structure of Magnus' Pink Salt. *J. Am. Chem. Soc.* **2014,** *136* (4), 1333-1351.
56. Austin, E. J. W.; Barrie, P. J.; Clark, R. J. H. Solid-State ^{195}Pt NMR-Studies of the Complexes Pt(En)Cl$_x$ (En = 1,2-Diaminoethane x = 2,3 or 4). *J. Chem. Soc., Chem. Commun.* **1993,** (18), 1404-1405.
57. Sparks, S. W.; Ellis, P. D. ^{195}Pt Shielding Tensors in Potassium Hexachloroplatinate(IV) and Potassium Tetrachloroplatinate(II). *J. Am. Chem. Soc.* **1986,** *108* (12), 3215-3218.
58. Sterzel, M.; Autschbach, J. Toward an Accurate Determination of ^{195}Pt Chemical Shifts by Density Functional Computations: The Importance of Unspecific Solvent Effects and the Dependence of Pt Magnetic Shielding Constants on Structural Parameters. *Inorg. Chem.* **2006,** *45* (8), 3316-3324.
59. Autschbach, J.; Zheng, S. H. Analyzing Pt Chemical Shifts Calculated from Relativistic Density Functional Theory Using Localized Orbitals: The Role of Pt 5d Lone Pairs. *Magn. Reson. Chem.* **2008,** *46*, S45-S55.
60. Lucier, B. E. G.; Reidel, A. R.; Schurko, R. W. Multinuclear Solid-State NMR of Square-Planar Platinum Complexes - Cisplatin and Related Systems. *Canadian Journal of Chemistry-Revue Canadienne De Chimie* **2011,** *89* (7), 919-937.
61. Siegel, R.; Nakashima, T. T.; Wasylishen, R. E. Application of Multiple-Pulse Experiments to Characterize Broad NMR Chemical-Shift Powder Patterns from Spin-1/2 Nuclei in the Solid State. *J. Phys. Chem. B* **2004,** *108* (7), 2218-2226.
62. Harris, K. J.; Lupulescu, A.; Lucier, B. E. G.; Frydman, L.; Schurko, R. W. Broadband Adiabatic Inversion Pulses for Cross Polarization in Wideline Solid-State NMR Spectroscopy. *J. Magn. Reson.* **2012,** *224*, 38-47.
63. Altenhof, A. R.; Jaroszewicz, M. J.; Lindquist, A. W.; Foster, L. D. D.; Veinberg, S. L.; Schurko, R. W. Practical Aspects of Recording Ultra-Wideline NMR Patterns under Magic-Angle Spinning Conditions. *J. Phys. Chem. C* **2020,** *124* (27), 14730-14744.
64. Kobayashi, T.; Perras, F. A.; Goh, T. W.; Metz, T. L.; Huang, W. Y.; Pruski, M. DNP-Enhanced Ultrawideline Solid-State NMR Spectroscopy: Studies of Platinum in Metal-Organic Frameworks. *J. Phys. Chem. Lett.* **2016,** *7* (13), 2322-2327.
65. Kobayashi, T.; Perras, F. A.; Murphy, A.; Yao, Y.; Catalano, J.; Centeno, S. A.; Dybowski, C.; Zumbulyadis, N.; Pruski, M. DNP-enhanced ultrawideline Pb-207 solid-state NMR spectroscopy: an application to cultural heritage science. *Dalton Trans.* **2017,** *46* (11), 3535-3540.
66. Venkatesh, A.; Lund, A.; Rochlitz, L.; Jabbour, R.; Gordon, C. P.; Menzildjian, G.; Viger-Gravel, J.; Berruyer, P.; Gajan, D.; Copéret, C.; Lesage, A.; Rossini, A. J. The Structure of Molecular and Surface Platinum Sites Determined by DNP-SENS and Fast MAS ^{195}Pt Solid-State NMR Spectroscopy. *J. Am. Chem. Soc.* **2020,** *142* (44), 18936-18945.
67. Ishii, Y.; Yesinowski, J. P.; Tycko, R. Sensitivity Enhancement in Solid-State ^{13}C NMR of Synthetic Polymers and Biopolymers by ^{1}H NMR Detection with High-Speed Magic Angle Spinning. *J. Am. Chem. Soc.* **2001,** *123* (12), 2921-2922.
68. Reif, B.; Griffin, R. G. ^{1}H Detected ^{1}H-^{15}N Correlation Spectroscopy in Rotating Solids. *J. Magn. Reson.* **2003,** *160* (1), 78-83.
69. Poppler, A. C.; Demers, J. P.; Malon, M.; Singh, A. P.; Roesky, H. W.; Nishiyama, Y.; Lange, A. Ultrafast Magic-Angle Spinning: Benefits for the Acquisition of Ultrawide-Line NMR Spectra of Heavy Spin-1/2 Nuclei. *ChemPhysChem* **2016,** *17* (6), 812-816.
70. Kobayashi, T.; Nishiyama, Y.; Pruski, M. Heteronuclear Correlation Solid-state NMR Spectroscopy with Indirect Detection under Fast Magic-Angle Spinning. In *Modern Methods in Solid-state NMR: A Practitioner's Guide*, Hodgkinson, P., Ed. The Royal Society of Chemistry: **2018**; pp 1-38.
71. Rossini, A. J.; Hanrahan, M. P.; Thuo, M. Rapid Acquisition of Wideline MAS Solid-State NMR Spectra with Fast MAS, Proton Detection, and Dipolar HMQC Pulse Sequences. *Phys. Chem. Chem. Phys.* **2016,** *18* (36), 25284-25295.
72. Perras, F. A.; Venkatesh, A.; Hanrahan, M. P.; Goh, T. W.; Huang, W.; Rossini, A. J.; Pruski, M. Indirect Detection of Infinite-Speed MAS Solid-State NMR Spectra. *J. Magn. Reson.* **2017,** *276*, 95-102.

73. Li, Y. X.; Trebosc, J.; Hu, B. W.; Shen, M.; Amoureux, J. P.; Lafon, O. Indirect detection of Broad Spectra in Solid-State NMR Using Interleaved DANTE Trains. *J. Magn. Reson.* **2018,** *294*, 101-114.

74. Venkatesh, A.; Perras, F. A.; Rossini, A. J. Proton-Detected Solid-State NMR Spectroscopy of Spin-1/2 Nuclei with Large Chemical Shift Anisotropy. *J. Magn. Reson.* **2021,** *327*, 106983.

75. Paluch, P.; Rankin, A. G. M.; Trebosc, J.; Lafon, O.; Amoureux, J. P. Analysis of HMQC Experiments Applied to a Spin 1/2 Nucleus Subject to Very Large CSA. *Solid State Nucl. Magn. Reson.* **2019,** *100*, 11-25.

76. Grey, C. P.; Vega, A. J. Determination of the Quadrupole Coupling-Constant of the Invisible Aluminum Spins in Zeolite HY with $^{1}H/^{27}Al$ TRAPDOR NMR. *J. Am. Chem. Soc.* **1995,** *117* (31), 8232-8242.

77. Kalwei, M.; Koller, H. Quantitative Comparison of REAPDOR and TRAPDOR Experiments by Numerical Simulations and Determination of H-Al Distances in Zeolites. *Solid State Nucl. Magn. Reson.* **2002,** *21* (3-4), 145-157.

78. Gan, Z. H. Measuring Nitrogen Quadrupolar Coupling with ^{13}C Detected Wide-line ^{14}N NMR under Magic-Angle Spinning. *Chem. Commun.* **2008,** (7), 868-870.

79. Jaroszewicz, M. J.; Altenhof, A. R.; Schurko, R. W.; Frydman, L. Sensitivity Enhancement by Progressive Saturation of the Proton Reservoir: A Solid-State NMR Analogue of Chemical Exchange Saturation Transfer. *J. Am. Chem. Soc.* **2021,** *143* (47), 19778-19784.

80. Brinkmann, A.; Kentgens, A. P. M. Proton-Selective ^{17}O-^{1}H Distance Measurements in Fast Magic Angle Spinning Solid-State NMR Spectroscopy for the Determination of Hydrogen Bond Lengths. *J. Am. Chem. Soc.* **2006,** *128* (46), 14758-14759.

81. Duong, N. T.; Rossi, F.; Makrinich, M.; Goldbourt, A.; Chierotti, M. R.; Gobetto, R.; Nishiyama, Y. Accurate ^{1}H-^{14}N Distance Measurements by Phase-Modulated RESPDOR at Ultra-Fast MAS. *J. Magn. Reson.* **2019,** *308*, 106559.

82. Perras, F. A.; Pruski, M. Reducing t_1 Noise through Rapid Scanning. *J. Magn. Reson.* **2019,** *298*, 31-34.

83. Venkatesh, A.; Luan, X.; Perras, F. A.; Hung, I.; Huang, W.; Rossini, A. J. t_1-Noise Eliminated Dipolar Heteronuclear Multiple-Quantum Coherence Solid-State NMR Spectroscopy. *Phys. Chem. Chem. Phys.* **2020,** *22*, 20815-20828.

84. Parella, T. Towards Perfect NMR: Spin-Echo versus Perfect-Echo Building Blocks. *Magn. Reson. Chem.* **2019,** *57* (1), 13-29.

85. Atterberry, B. A.; Carnahan, S. L.; Chen, Y.; Venkatesh, A.; Rossini, A. J. Double Echo Symmetry-Based REDOR and RESPDOR Pulse Sequences for Proton Detected Measurements of Heteronuclear Dipolar Coupling Constants. *J. Magn. Reson.* **2022,** *336*, 107147.

86. Bak, M.; Rasmussen, J. T.; Nielsen, N. C. SIMPSON: A General Simulation Program for Solid-State NMR Spectroscopy. *J. Magn. Reson.* **2000,** *147* (2), 296-330.

87. Tosner, Z.; Vosegaard, T.; Kehlet, C.; Khaneja, N.; Glaser, S. J.; Nielsen, N. C. Optimal Control in NMR Spectroscopy: Numerical Implementation in SIMPSON. *J. Magn. Reson.* **2009,** *197* (2), 120-134.

88. Tosner, Z.; Andersen, R.; Stevenss, B.; Eden, M.; Nielsen, N. C.; Vosegaard, T. Computer-Intensive Simulation of Solid-State NMR Experiments using SIMPSON. *J. Magn. Reson.* **2014,** *246*, 79-93.

89. Ha, K. Crystal structure of bis(pentane-2,4-dionato-kappa O-2,O ')platinum(II), $Pt(C_5H_7O_2)_2$. *Z. Kristallogr. NCS* **2011,** *226* (3), 329-330.

90. Dechter, J. J.; Kowalewski, J. ^{195}Pt Spin-Lattice Relaxation and Shielding Anisotropy for $Pt(Acac)_2$. *J. Magn. Reson.* **1984,** *59* (1), 146-149.

91. Ruddy, D. A.; Jarupatrakorn, J.; Rioux, R. M.; Miller, J. T.; McMurdo, M. J.; Mcbee, J. L.; Tupper, K. A.; Tilley, T. D. Site-Isolated Pt-SBA15 Materials from Tris(tert-butoxy)siloxy Complexes of Pt(II) and Pt(IV). *Chem. Mater.* **2008,** *20* (20), 6517-6527.

92. Goikhman, R.; Aizenberg, M.; Shimon, L. J. W.; Milstein, D. Transition Metal-Catalyzed Silanone Generation. *J. Am. Chem. Soc.* **1996,** *118* (44), 10894-10895.
93. Davis, J. C.; Buhl, M.; Koch, K. R. On the Origin of $^{35/37}$Cl Isotope Effects on ^{195}Pt NMR Chemical Shifts. A Density Functional Study. *J. Chem. Theory Comput.* **2012,** *8* (4), 1344-1350.
94. Bryce, D. L. NMR Crystallography: Structure and Properties of Materials from Solid-State Nuclear Magnetic Resonance Observables. *Iucrj* **2017,** *4*, 350-359.
95. Hodgkinson, P. NMR Crystallography of Molecular Organics. *Prog. Nucl. Magn. Reson. Spectrosc.* **2020,** *118-119*, 10-53.
96. Gilbert, T. M.; Ziegler, T. Prediction of ^{195}Pt NMR Chemical Shifts by Density Functional Theory Computations: The Importance of Magnetic Coupling and Relativistic Effects in Explaining Trends. *J. Phys. Chem. A* **1999,** *103* (37), 7535-7543.
97. Frisch, M. J.; Trucks, G. W.; Schlegel, H. B.; Scuseria, G. E.; Robb, M. A.; Cheeseman, J. R.; Scalmani, G.; Barone, V.; Mennucci, B.; Petersson, G. A.; Nakatsuji, H.; Caricato, M.; Li, X.; Hratchian, H. P.; Izmaylov, A. F.; Bloino, J.; Zheng, G.; Sonnenberg, J. L.; Hada, M.; Ehara, M.; Toyota, K.; Fukuda, R.; Hasegawa, J.; Ishida, M.; Nakajima, T.; Honda, Y.; Kitao, O.; Nakai, H.; Vreven, T.; Montgomery, J. A.; Peralta, J. J. E.; Ogliaro, F.; Bearpark, M.; Heyd, J. J.; Brothers, E.; Kudin, K. N.; Staroverov, V. N.; Kobayashi, R.; Normand, J.; Raghavachari, K.; Rendell, A.; Burant, J. C.; Iyengar, S. S.; Tomasi, J.; Cossi, M.; Rega, N.; Millam, J. M.; Klene, M.; Knox, J. E.; Cross, J. B.; Bakken, V.; Adamo, C.; Jaramillo, J.; Gomperts, R.; Stratmann, R. E.; Yazyev, O.; Austin, A. J.; Cammi, R.; Pomelli, C.; Ochterski, J. W.; Martin, R. L.; Morokuma, K.; Zakrzewski, V. G.; Voth, G. A.; Salvador, P.; Dannenberg, J. J.; Dapprich, S.; Daniels, A. D.; Farkas, Ö.; Foresman, J. B.; Ortiz, J. V.; Cioslowski, J.; Fox, D. J. *Gaussian 09 Version D.01*, Gaussian Inc.: Wallingford, CT, 2009.
98. te Velde, G.; Bickelhaupt, F. M.; Baerends, E. J.; Guerra, C. F.; Van Gisbergen, S. J. A.; Snijders, J. G.; Ziegler, T. Chemistry with ADF. *J. Comput. Chem.* **2001,** *22* (9), 931-967.
99. Sandoval, J. J.; Palma, P.; Alvarez, E.; Campora, J.; Rodriguez-Delgado, A. Mechanism of Alkyl Migration in Diorganomagnesium 2,6-Bis(imino)pyridine Complexes: Formation of Grignard-Type Complexes with Square-Planar Mg(II) Centers. *Organometallics* **2016,** *35* (18), 3197-3204.
100. Su, K.; Tilley, T. D.; Sailor, M. J. Molecular and Polymer Precursor Routes to Manganese-Doped Zinc Orthosilicate Phosphors. *J. Am. Chem. Soc.* **1996,** *118* (14), 3459-3468.
101. Smith, D. C.; Haar, C. M.; Stevens, E. D.; Nolan, S. P.; Marshall, W. J.; Moloy, K. G. Synthetic, Structural, and Solution Calorimetric Studies of $Pt(CH_3)_2(PP)$ Complexes. *Organometallics* **2000,** *19* (7), 1427-1433.
102. Searles, K.; Siddiqi, G.; Safonova, O. V.; Coperet, C. Silica-Supported Isolated Gallium Sites as Highly Active, Selective and Stable Propane Dehydrogenation Catalysts. *Chem. Sci.* **2017,** *8* (4), 2661-2666.
103. Yanai, T.; Tew, D. P.; Handy, N. C. A New Hybrid Exchange-Correlation Functional using the Coulomb-Attenuating Method (CAM-B3LYP). *Chem. Phys. Lett.* **2004,** *393* (1-3), 51-57.
104. Rassolov, V. A.; Pople, J. A.; Ratner, M. A.; Windus, T. L. 6-31G* Basis Set for Atoms K through Zn. *J. Chem. Phys.* **1998,** *109* (4), 1223-1229.
105. Roy, L. E.; Hay, P. J.; Martin, R. L. Revised Basis Sets for the LANL Effective Core Potentials. *J. Chem. Theory Comput.* **2008,** *4* (7), 1029-1031.
106. vanLenthe, E.; vanLeeuwen, R.; Baerends, E. J.; Snijders, J. G. Relativistic Regular Two-Component Hamiltonians. *Int. J. Quantum Chem.* **1996,** *57* (3), 281-293.
107. Zurek, E.; Pickard, C. J.; Autschbach, J. Density Functional Study of the ^{13}C NMR Chemical Shifts in Single-Walled Carbon Nanotubes with Stone-Wales Defects. *J. Phys. Chem. C* **2008,** *112* (31), 11744-11750.
108. Clark, S. J.; Segall, M. D.; Pickard, C. J.; Hasnip, P. J.; Probert, M. J.; Refson, K.; Payne, M. C. First Principles Methods using CASTEP. *Z. Kristallogr.* **2005,** *220* (5-6), 567-570.
109. Perdew, J. P.; Burke, K.; Ernzerhof, M. Generalized Gradient Approximation Made Simple. *Phys. Rev. Lett.* **1996,** *77* (18), 3865-3868.

110. Tkatchenko, A.; Scheffler, M. Accurate Molecular Van Der Waals Interactions from Ground-State Electron Density and Free-Atom Reference Data. *Phys. Rev. Lett.* **2009,** *102* (7), 073005.
111. van Meerten, S. G. J.; Franssen, W. M. J.; Kentgens, A. P. M. ssNake: A cross-Platform Open-Source NMR Data Processing and Fitting Application. *J. Magn. Reson.* **2019,** *301*, 56-66.
112. Oas, T. G.; Griffin, R. G.; Levitt, M. H. Rotary Resonance Recoupling of Dipolar Interactions in Solid-State Nuclear Magnetic-Resonance Spectroscopy. *J. Chem. Phys.* **1988,** *89* (2), 692-695.
113. Herzfeld, J.; Berger, A. E. Sideband Intensities in NMR Spectra of Samples Spinning at the Magic Angle. *J. Chem. Phys.* **1980,** *73* (12), 6021-6030.
114. Eichele, K. *HBA 1.7.5*, Universität Tübingen, 2015.
115. Fung B.M.; Khitrin A. K.; Ermolaev K. An Improved Broadband Decoupling Sequence for Liquid Crystals and Solids. *J. Magn. Reson.*, **2000**, *142*, 97-101.

Supporting Information for:

The Molecular and Electronic Structure of Isolated Platinum Sites Enabled by Expedient Measurement of ^{195}Pt Chemical Shift Anisotropy

Amrit Venkatesh,[1,2] Domenico Gioffrè,[3] Benjamin A. Atterberry,[1,2] Lukas Rochlitz,[3] Scott L. Carnahan,[1,2] Zhuoran Wang,[4] Georges Menzildjian,[4] Anne Lesage,[4] Christophe Copéret,[3]* Aaron J. Rossini[1,2]**

[1]*Iowa State University, Department of Chemistry, Ames, IA, USA, 50011*

[2]*US DOE Ames Laboratory, Ames, Iowa, USA, 50011*

[3]*Department of Chemistry and Applied Biosciences, ETH Zürich, CH-8093 Zürich, Switzerland.*

[4]*Univ Lyon, ENS Lyon, Université Lyon 1, CNRS, High-Field NMR Center of Lyon, UMR 5082, F-69100 VILLEURBANNE, France.*

Table of Contents

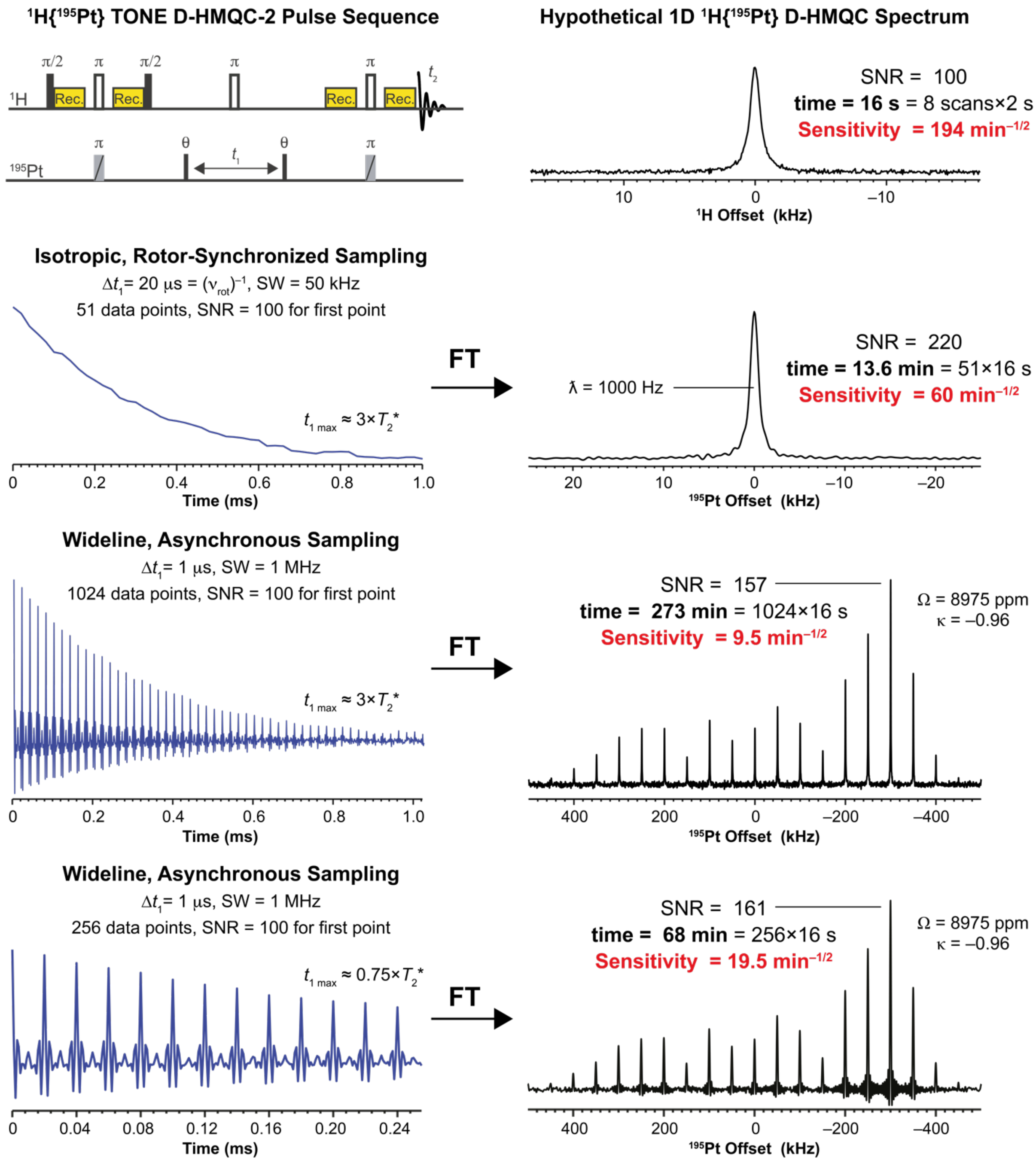

Figure S1. Figure showing simulations of ^{195}Pt NMR spectra using SIMPSON to compare the differences in sensitivity between a (1st row, top) hypothetical 1D ^{1}H{^{195}Pt} TONE D-HMQC-2 spectrum, (2nd row) the isotropic ^{195}Pt NMR spectrum with rotor-synchronized t_1-sampling, (3rd row) the anisotropic ^{195}Pt NMR spectrum with wideline, rotor-asynchronous sampling up to a $t_{1,\mathrm{max}}$ of ca. $3\times T_2$*, which is typically required to resolve multiple ^{195}Pt patterns, and (4th row, bottom) the anisotropic ^{195}Pt NMR spectrum with wideline, rotor-asynchronous sampling and limited $t_{1,\mathrm{max}}$ ($0.75\times T_2$*). The different ^{195}Pt NMR spectra were simulated in SIMPSON by changing the dwell period (Δt_1). Note that these comparisons assume there is no t_1-noise. However, t_1-noise will likely further reduce sensitivity of the wideline, asynchronous sampling methods.

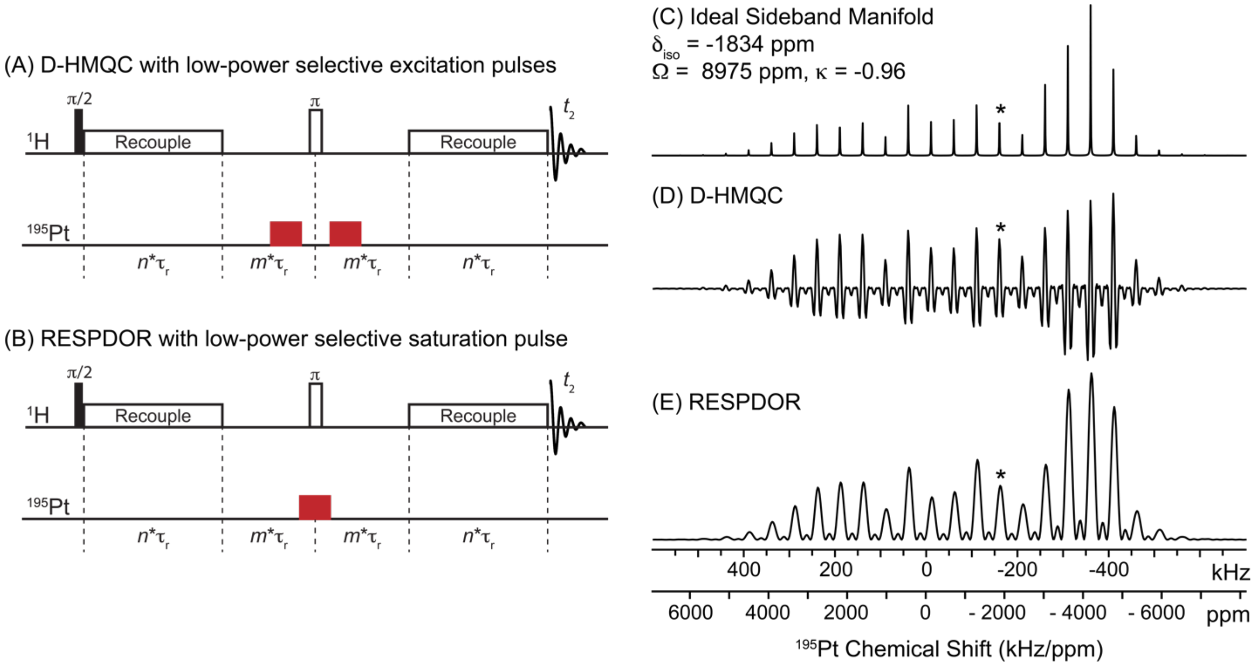

Figure S2. ^{1}H{^{195}Pt} (A) D-HMQC and (B) RESPDOR pulse sequences with long-duration, low-power selective excitation and saturation pulses, respectively, on the ^{195}Pt channel (red rectangles). Typical ^{195}Pt pulse durations are between 20 and 80 μs. *m* and *n* are positive integers and τ_r denotes a rotor period. Simulations of ^{195}Pt CSA sideband manifolds at 50 kHz MAS and B_0 = 9.4 T: (C) analytical simulation, numerical simulations of sideband manifolds obtained with (D) D-HMQC and (E) RESPDOR by varying the offset of 60 μs ^{195}Pt sideband selective pulses. Previously reported values of ^{195}Pt isotropic shifts, and CSA parameters (Ω and κ) of cisplatin were used in all cases (indicated in (D)). The isotropic shift is indicated by an asterisk.

Table S1. Comparison of optimal rf powers for selective excitation pulses of different lengths in D-HMQC SIMPSON simulations and experiments with cisplatin. In both cases, the pulse sequence shown in Figure S2A was used.

Pulse length (μs)	**Optimized rf field (kHz)**	
	SIMPSON	**Experiment**
20	25	30
40	13	16
60	9	9
80	7	7

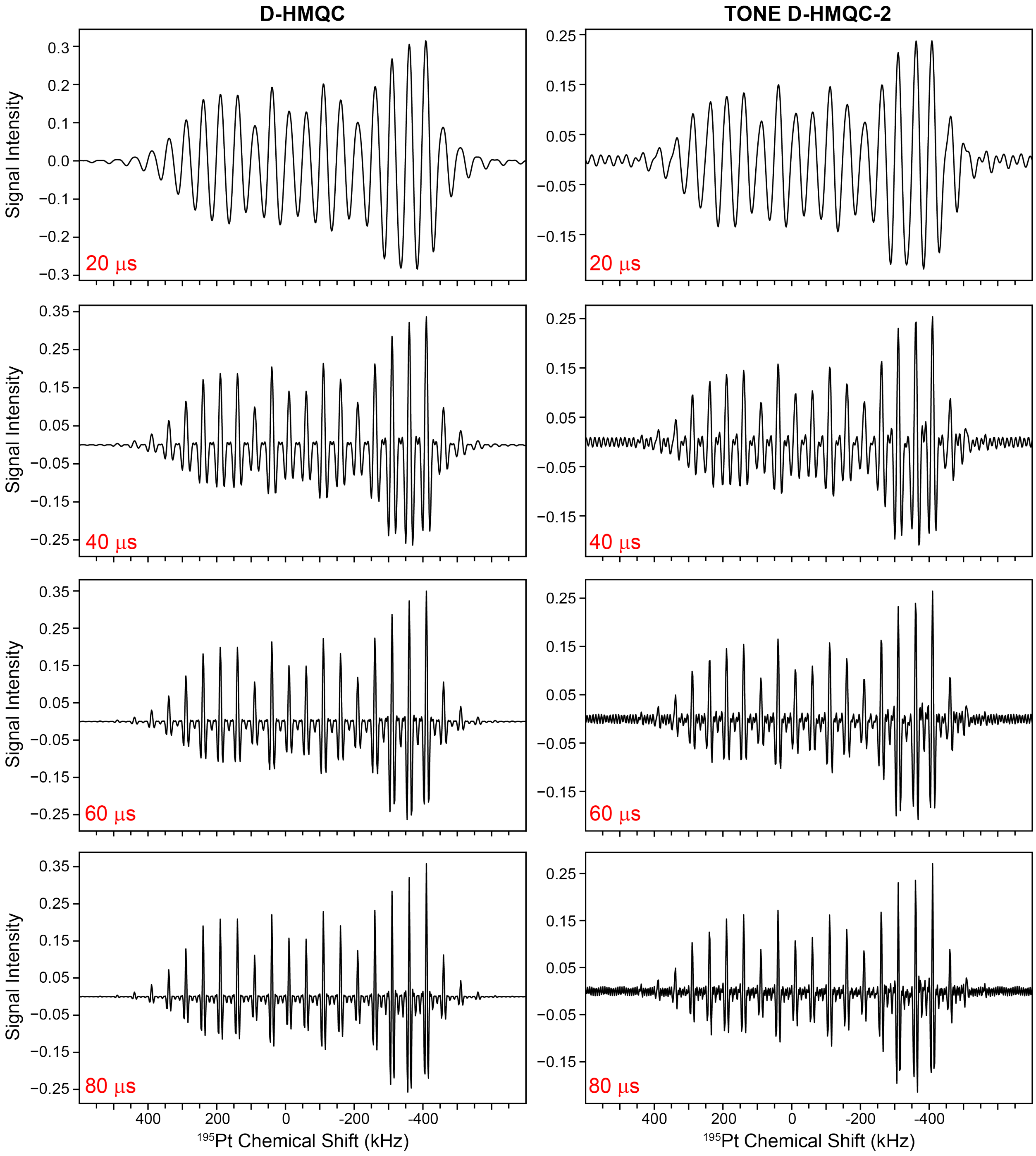

Figure S3. SIMPSON simulations of ^{1}H{^{195}Pt} (left column) D-HMQC and (right column) TONE D-HMQC-2 with the indicated sideband-selective pulse durations. The ^{1}H-^{195}Pt dipolar coupling was set to –3500 Hz and an optimal recoupling duration of 2.88 ms was used. The rep168 crystal file and 17 gamma angles were used for powder averaging. In the TONE D-HMQC-2 simulations, SHAP used tanh/tan shapes with a 20 μs duration, 270 kHz rf and 5 MHz sweep width.

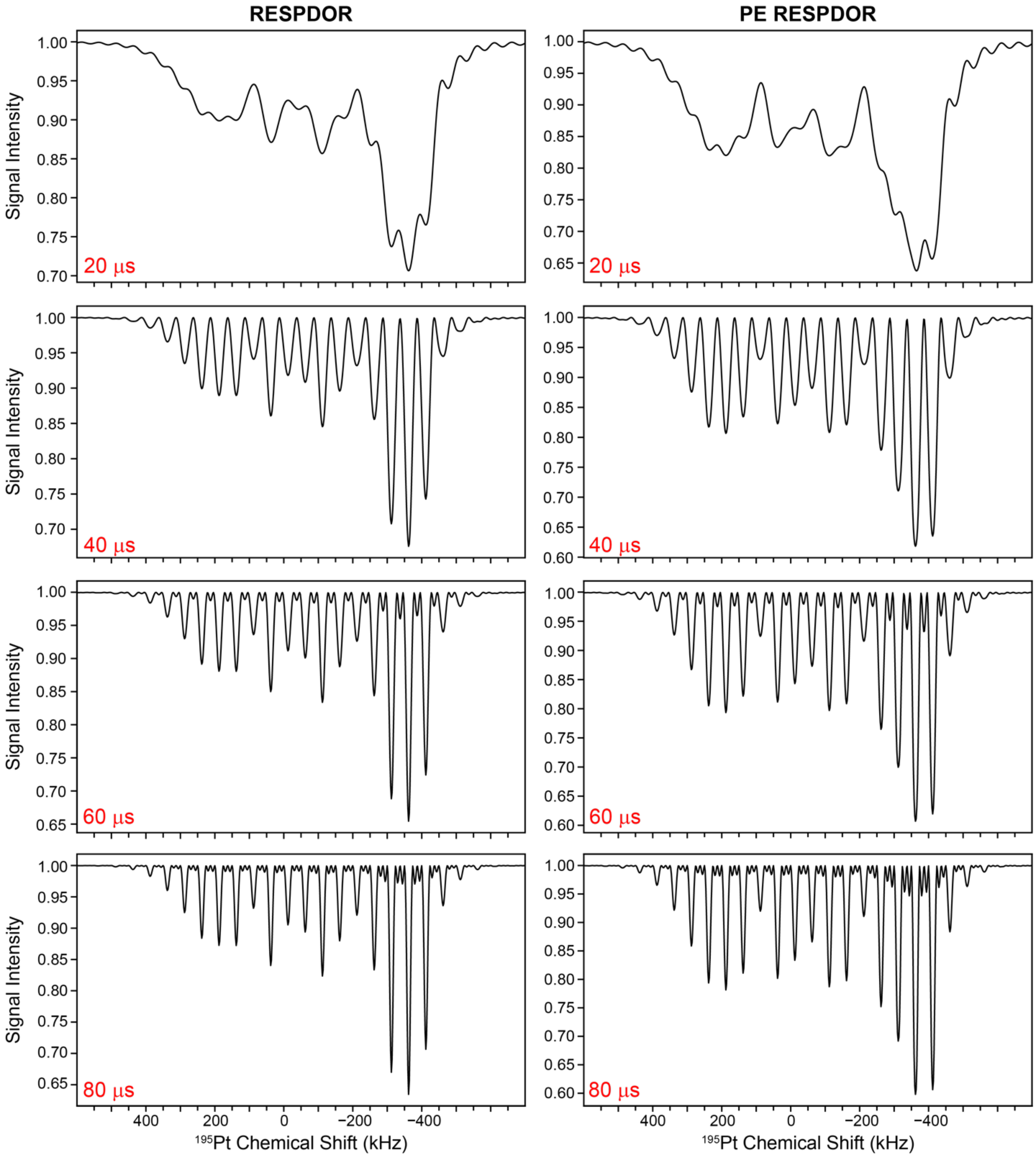

Figure S4. SIMPSON simulations of $^{1}H\{^{195}Pt\}$ (left column) RESPDOR and (right column) PE RESPDOR with the indicated sideband-selective pulse durations. The ^{1}H-^{195}Pt dipolar coupling was set to –3500 Hz and an optimal recoupling duration of 2.88 ms was used. The rep168 crystal file and 17 gamma angles were used for powder averaging. Note that the rf powers used for the simulations were optimized with D-HMQC experiments (Table S1). Therefore, the selectivity can be improved by reducing the rf powers for RESPDOR (particularly with 20 µs pulse duration), at the expense of the signal dephasing amount.

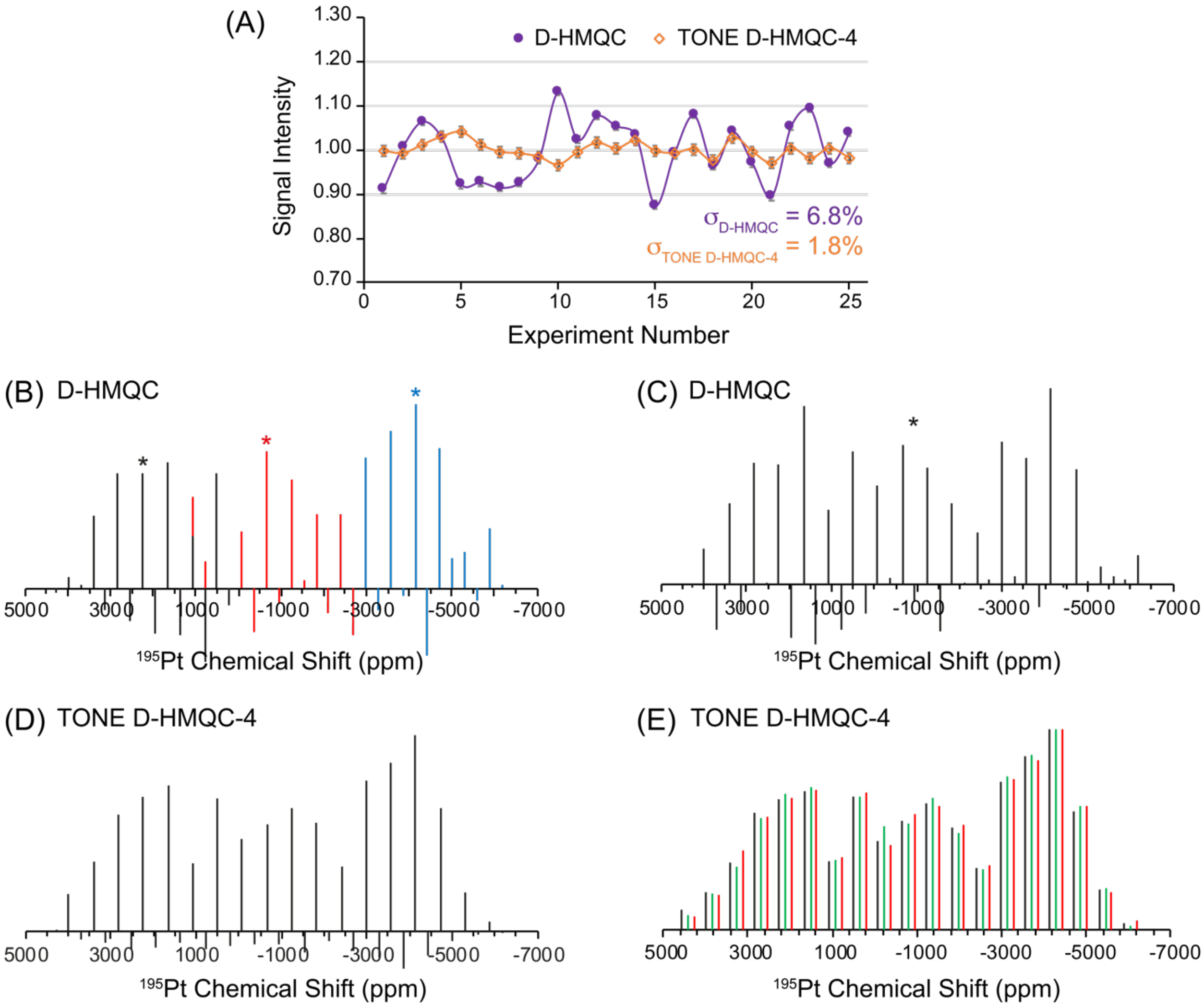

Figure S5. Sideband-selective $^{1}H\{^{195}Pt\}$ D-HMQC experiments with cisplatin. (A) Plot showing the normalized signal intensities obtained from repeated acquisition of 1D D-HMQC and TONE D-HMQC-4 experiments to illustrate the effect of MAS instability and the improved robustness of TONE D-HMQC. Sideband-selective $^{1}H\{^{195}Pt\}$ D-HMQC patterns acquired by (B) tuning the probe to three different positions and (C) tuning the probe to the center of the pattern. The frequencies to which the probe was tuned are indicated by asterisks. (D) Sideband-selective $^{1}H\{^{195}Pt\}$ TONE D-HMQC-4 obtained with probe tuned to the center of the spectrum. The comparison of the patterns in (C) and (D) emphasizes the reliability of the signal intensities from using TONE D-HMQC. In B-D, the ^{195}Pt transmitter offset of the excitation pulses was varied in steps of half the MAS frequency. (E) Comparison of three different sideband-selective $^{1}H\{^{195}Pt\}$ TONE D-HMQC-4 experiments to illustrate reproducibility (shown in red, green and black). Here, the ^{195}Pt transmitter offset was varied in steps of the MAS frequency. In all cases, the total recoupling time was 1.92 ms, and 60 μs saturation pulses at 9 kHz rf field were applied on the ^{195}Pt channel. In (A), the ^{195}Pt selective pulse offset was set to the most intense sideband.

Note S1: Robustness of perfect echo RESPDOR for sideband-selective dephasing experiments

PE RESPDOR provides improved robustness towards MAS fluctuations because it has a similar symmetry as the TONE D-HMQC experiments.[1] It is also well-established from solution NMR experiments that perfect echoes can refocus homonuclear scalar couplings.[2-4] Indeed, PE RESPDOR is shown to partly refocus ^{1}H homonuclear dipolar couplings and improve ^{1}H T_2' under heteronuclear dipolar recoupling, below.

Experimentally, the sensitivity of $SR4_1^2$ recoupled perfect echo (PE) and spin echo (SE) experiments, i.e. the control experiments of RESPDOR and PE RESPDOR (Figure S6), to MAS instability was investigated by repeatedly acquiring 1D ^{1}H NMR spectra of cisplatin. For these experiments, 8 scans were obtained with a 2.88 ms total duration of $SR4_1^2$ recoupling (Figure S7A). The standard deviation (σ) of the recoupled spin echo signal intensity was about 5%, whereas the recoupled perfect echo showed a σ of only 0.7%; the significantly lower variation of the ^{1}H NMR signal intensity clearly demonstrates the improved robustness to MAS instability for the PE sequence. This effect is persistent even at long recoupling times of 5.8 ms, where the σ of the PE sequence was much lower (5%) in comparison to the spin echo which showed a σ of 21% (Figure S8).

As described previously, the perfect echo symmetry increases efficiency by refocusing ^{1}H CSA across each of spin echo blocks, while the central π/2 pulse partly refocuses ^{1}H-^{1}H homonuclear dipolar couplings.[1] This results in an approximate doubling of the transverse relaxation time (T_2'), which is evident in Figure S7B. An increase in T_2' with PE RESPDOR was also observed for L-histidine·HCl·H$_2$O. Notably the improvement in T_2' is observed only with recoupled echo experiments and not with standard spin echo sequences (Figure S9 and S10).

The RESPDOR difference (S_0–S) signal intensity builds up to a maximum but decays and fluctuates rapidly after 2 ms of recoupling due to MAS instability, whereas the PE RESPDOR difference is more robust up to 5 ms of recoupling (Figure S7C). Consequently, the dipolar build-up curve (1–S/S_0) with the PE RESPDOR is significantly more robust, which will likely enable more accurate heteronuclear distance measurements.

With a 2.88 ms total recoupling duration, the recoupled perfect echo shows nearly two times more signal than a recoupled spin echo (S_0, Figure S7E). Next, the transmitter was placed on-resonance with the most intense sideband in the ^{195}Pt spectrum (Figure 1D) and a 60 µs saturation pulse at 9 kHz rf field was applied. On the application of saturation pulses, ca. 20 and 9% dephasing [$(1-S/S_0)\times100$], respectively, was observed with RESPDOR and PE RESPDOR. The gain in sensitivity with PE RESPDOR is translated to the dephased signal (S_0-S), as expected, with the PE RESPDOR showing about the same absolute signal (0.2 *vs* 0.17) as RESPDOR, even though the dephasing amount is lower with PE RESPDOR. These results clearly demonstrate the value of the PE RESPDOR pulse sequence.

Figure S11 shows sideband-selective ^{1}H{^{195}Pt} RESPDOR and PE RESPDOR patterns obtained with 5.6 or 2.88 ms total dipolar recoupling times. The fluctuation of the signal due to MAS instability results in 'noisier' sideband patterns for the longer recoupling time (Figure S11A). However, at both recoupling times, it is clearly evident the PE RESPDOR experiment provides more reliable sideband signal intensities, even though the maximum dephasing difference is only 9%. Notably, the dephasing observed in the PE RESPDOR experiment off-resonance from a ^{195}Pt sideband is minimal, which allows clear identification of the sideband (Figure S11B). As a result, PE RESPDOR provides reproducible sideband intensities (Figure S11C). Given that there is a 0.7% fluctuation of the control signal intensity due to MAS instability (Figure S7A) and a total dephasing of 9%, this may result in about 10% fluctuation of the dephasing difference signal intensities and hence in the experimental ^{195}Pt sideband intensities. Consequently, TONE D-HMQC-4 may provide more reliable ^{195}Pt NMR spectra.

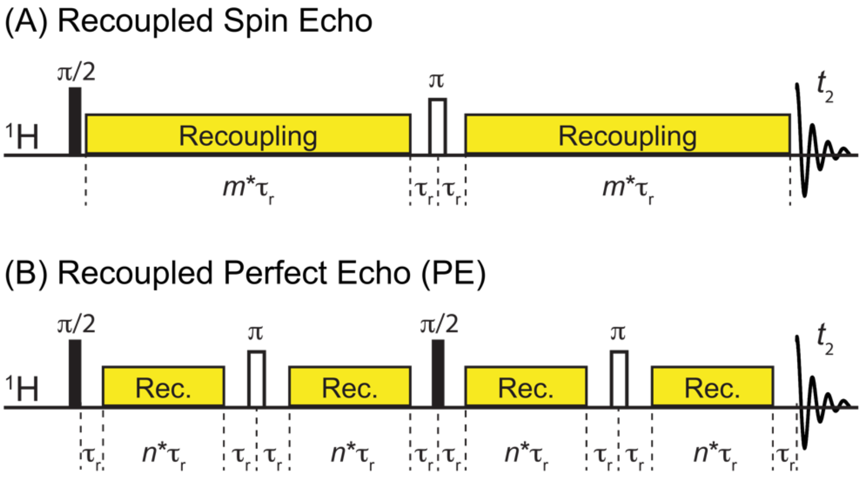

Figure S6. $SR4_1^2$ recoupled (A) spin echo and (B) perfect echo pulse sequences used to obtain the control signal intensities (S_0) for RESPDOR and PE RESPDOR, respectively. m and n are integers where $n = m/2$, and τ_r denotes a rotor period.

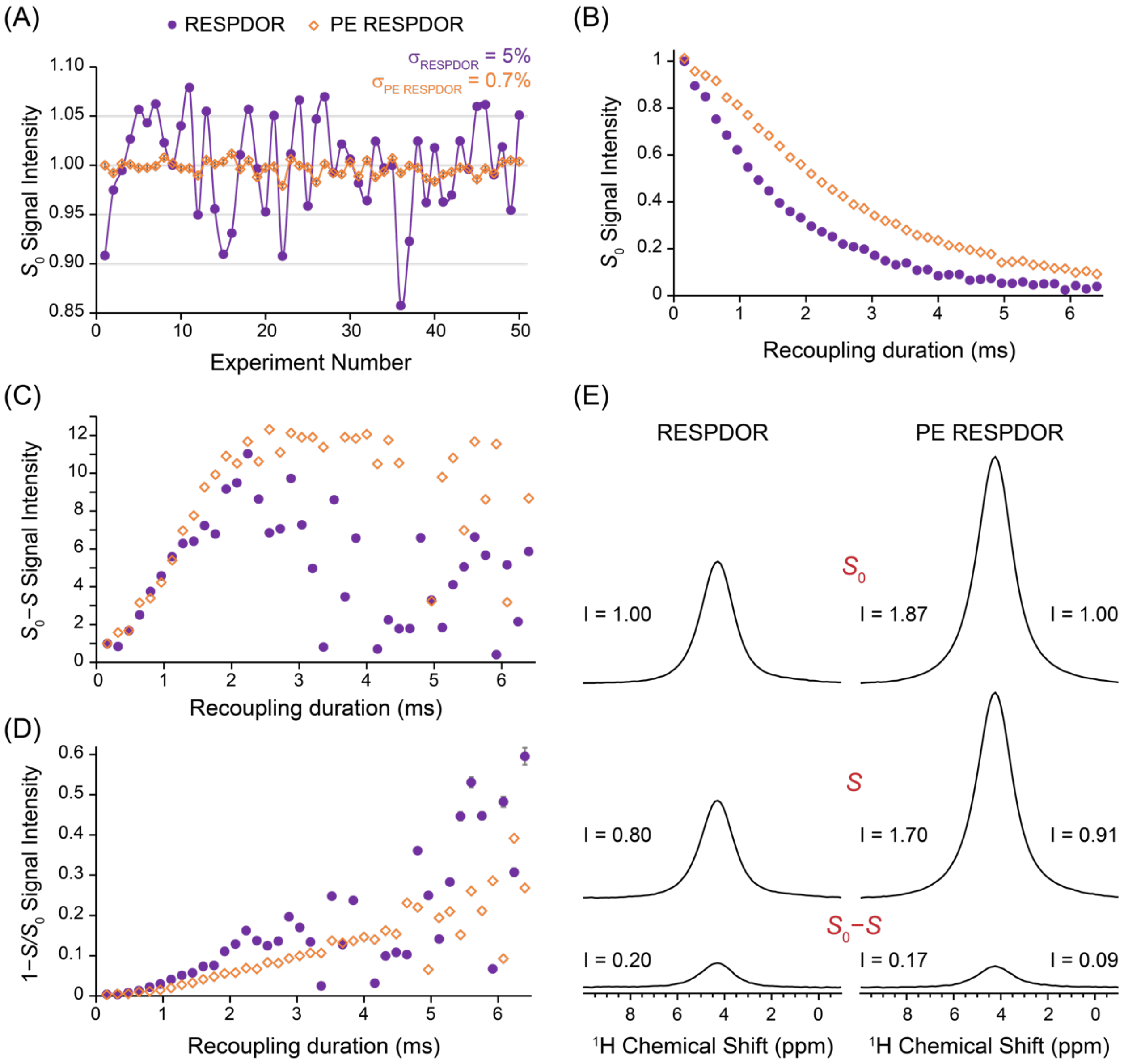

Figure S7. ^{1}H{^{195}Pt} RESPDOR and PE RESPDOR experiments with cisplatin. (A) Plots showing experimental control signal intensities (S_0) for (purple circles) RESPDOR and (orange diamonds) PE RESPDOR with a 2.88 ms total $SR4_1^2$ recoupling duration. (B) Variation of signal intensities with total recoupling duration on cisplatin, showing an approximate doubling of the transverse relaxation delay time constant with the PE sequence. (C) Plot showing the absolute signal intensity of the difference spectra (S_0-S) at different recoupling durations. (D) Plot of 1–S/S_0 as a function of the total recoupling duration. (E) Comparison of the control (S_0), dephased (S) and difference (S_0–S) ^{1}H{^{195}Pt} spectra obtained with RESPDOR and PE RESPDOR pulse sequences and 2.88 ms total recoupling duration. The relative signal intensities are provided to show the gain in signal with PE RESPDOR. Error bars based on signal-to-noise ratios are smaller than the data markers. Experiments were performed with 8 scans, 10 s recycle delay; 60 μs ^{195}Pt sideband selective pulses at 9 kHz rf were applied at a ^{195}Pt chemical shift of ca. –4150 ppm, corresponding to the most intense sideband.

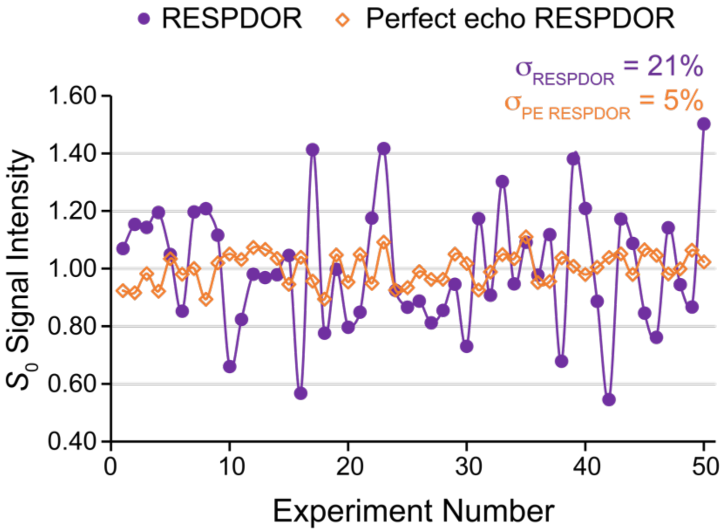

Figure S8. Plots showing experimental control signal intensities (S_0) for $SR4_1^2$ recoupled RESPDOR and perfect echo RESPDOR experiments with cisplatin. (A) Repeated acquisition of 8 scans (10 s recycle delay) with each pulse sequence, to illustrate the improved reliability of PE RESPDOR. The total recoupling duration was 5.6 ms in all experiments. Signal intensities were normalized to the average signal intensity of each dataset.

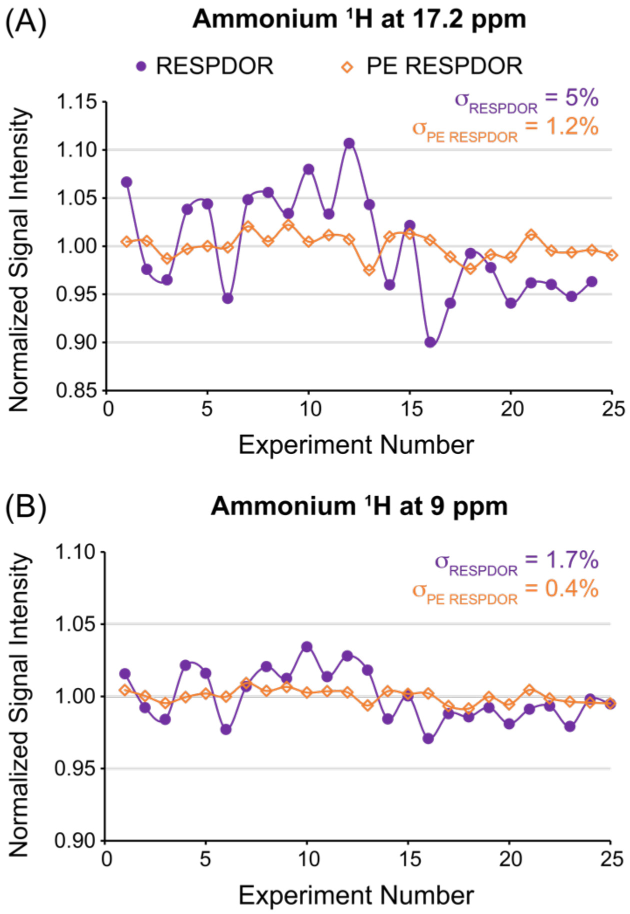

Figure S9. Plots showing experimental control signal intensities (S_0) for $SR4_1^2$ recoupled RESPDOR and PE RESPDOR experiments with L-histidine·HCl·H_2O. Plots are shown for (A) the NH^+ ammonium ^1H NMR signal at 17.2 ppm and for the (B) NH_3^+ ammonium ^1H NMR signal at 9 ppm. Repeated acquisition of 64 scans (0.5 s recycle delay) with each pulse sequence, to illustrate the improved reliability of PE RESPDOR. The total recoupling duration was 3.2 ms in all experiments. Signal intensities were normalized to the average signal intensity of each dataset.

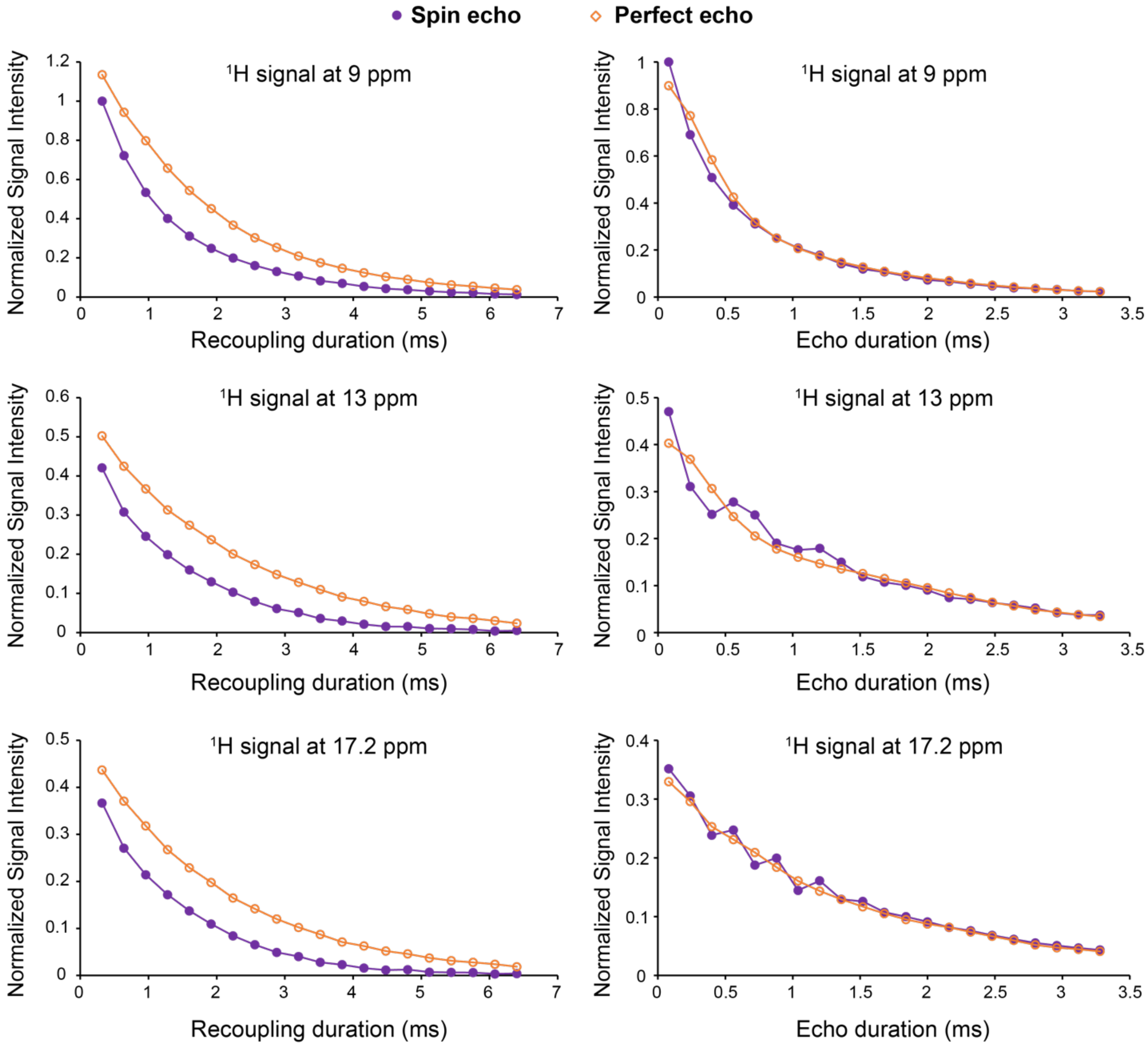

Figure S10. (Left) Variation of ^{1}H NMR signal intensities with total recoupling duration for $SR4_1^2$ recoupled spin echo and recoupled perfect echo pulse sequences. (Right) Variation of ^{1}H NMR signal intensities with total evolution time for a standard spin echo and perfect echo (no recoupling applied during echo delays). All data shown were acquired with L-histidine·HCl·H_2O. All signal intensities were normalized with respect to the ^{1}H spin echo signal at 9 ppm (top plots, purple). Experiments with recoupling show an increase of the ^{1}H transverse relaxation delay time constant (T_2') with the PE sequence due to improved robustness with respect to ^{1}H-^{1}H homonuclear dipolar couplings.

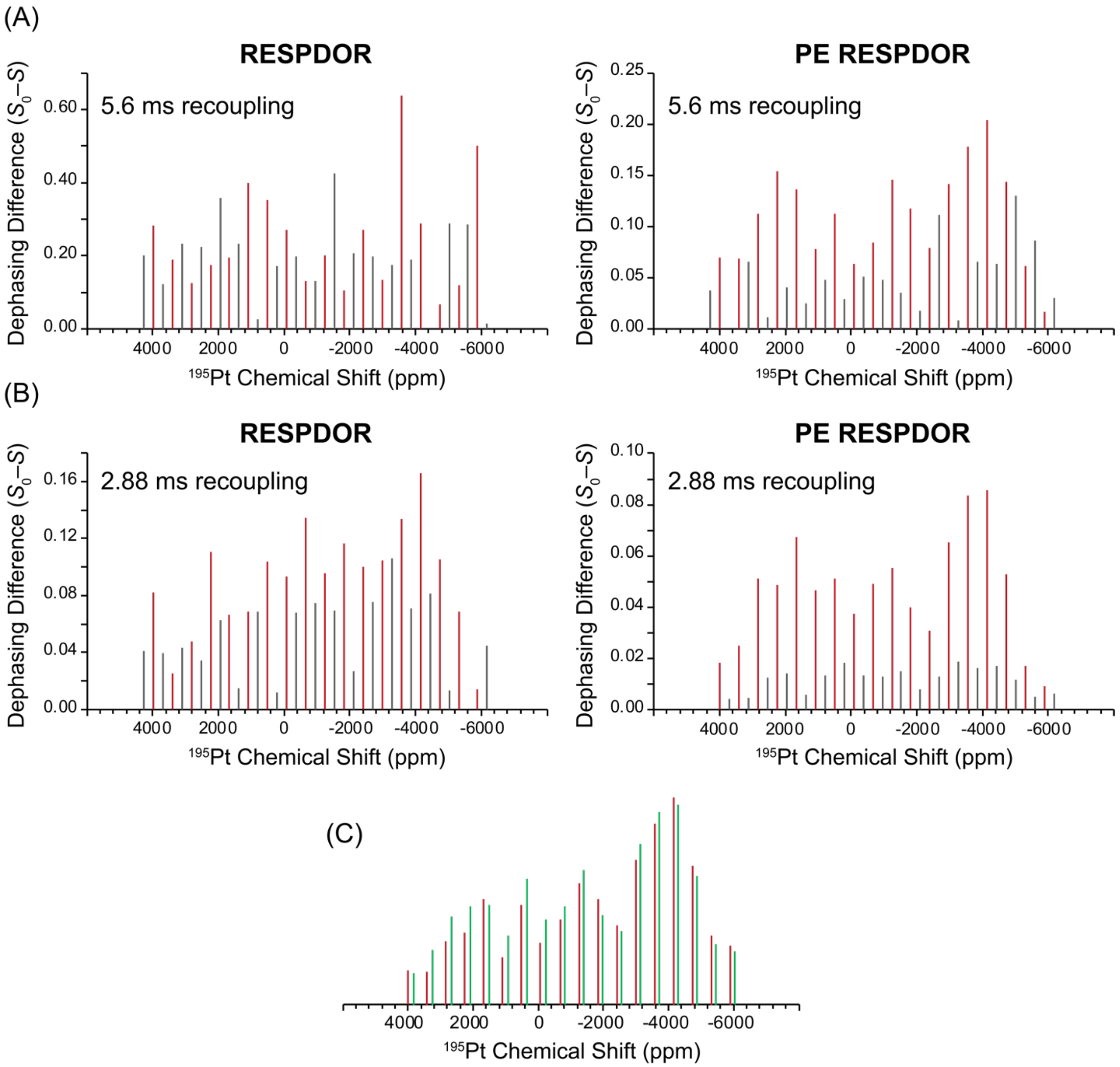

Figure S11. Sideband-selective ^{1}H{^{195}Pt} (left) RESPDOR and (right) PE RESPDOR experiments with cisplatin at (A) 5.6 ms and (B) 2.88 ms total dipolar recoupling times. The ^{195}Pt transmitter offset was varied in steps of half the MAS frequency; the off-resonance signals are colored grey whereas the on-resonance signals are in red. (C) Plot showing the reproducibility of sideband-selective ^{1}H{^{195}Pt} PE RESPDOR with 2.88 ms total recoupling time by comparing two sets of experimental sideband patterns (colored red and green). Here, the ^{195}Pt transmitter offset was varied in steps of the MAS frequency. In all cases, 60 μs saturation pulses with 9 kHz rf field were applied on the ^{195}Pt channel.

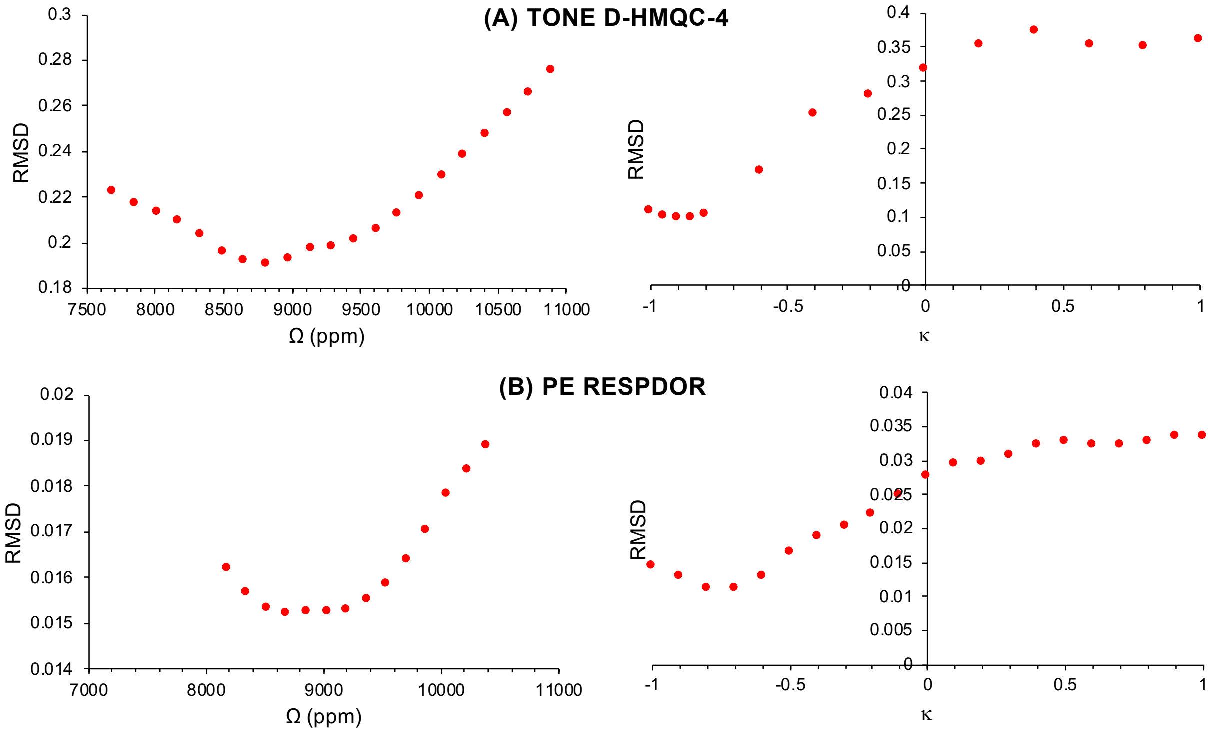

Figure S12. Plots showing the RMSD between the SIMPSON simulated and experimental sideband intensities obtained with sideband-selective $^{1}H\{^{195}Pt\}$ (A) TONE D-HMQC-4 and (B) PE RESPDOR for cisplatin (**1**). κ was initially set to –0.75 and –0.53 for TONE D-HMQC-4 and PE RESPDOR, respectively, and Ω was varied. The Ω with the lowest RMSD was then used to fit κ. SIMPSON simulations in (A) used the TONE D-HMQC-2 pulse sequence.

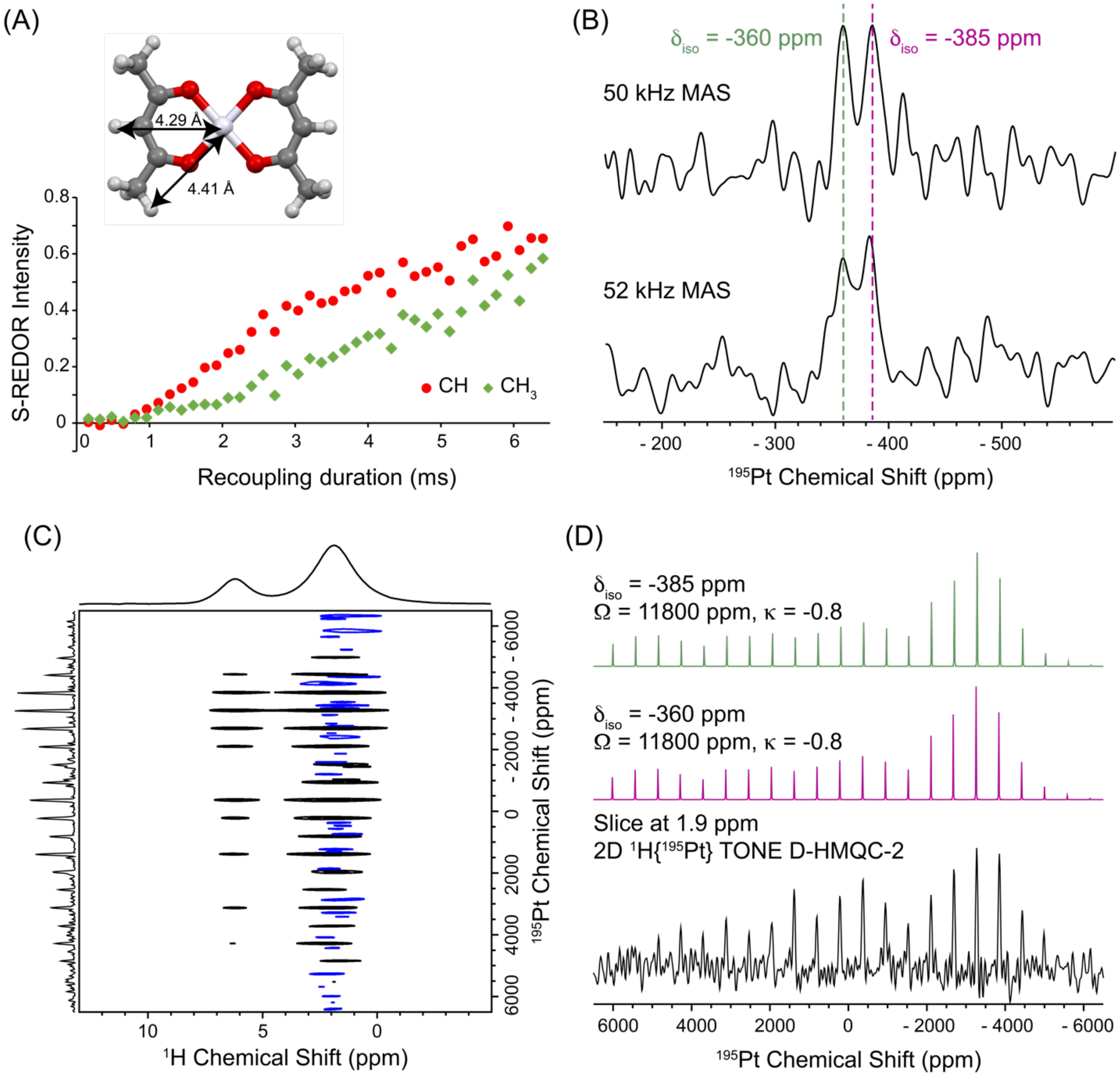

Figure S13. (A) ^{1}H{^{195}Pt} SHAP S-REDOR build-up curves of Pt(acac)$_2$; the intensities of the CH and CH$_3$ signals appearing at 6.3 and 1.9 ppm, respectively are plotted. Pt-HC distances to the CH and nearest methyl protons are shown in the structure of Pt(acac)$_2$ in (A). Plane-wave DFT was used to optimize the hydrogen atom positions from the previously reported crystal structure.[5] (B) ^{195}Pt NMR spectra extracted from rotor-synchronized 2D ^{1}H{^{195}Pt} TONE D-HMQC-4 to measure the ^{195}Pt isotropic chemical shifts. (C) Wideline 2D ^{1}H{^{195}Pt) AID TONE D-HMQC-2 spectrum which required 45 hours to acquire. (D) ^{195}Pt NMR spectrum extracted from the 2D spectrum shown in (C) at a ^{1}H chemical shift of 1.9 ppm, to measure the ^{195}Pt CSA parameters.

NOTE S2. ^{195}Pt CSA of Pt(acac)$_2$ (2)

Using the recently reported Arbitrary Indirect Dwell (AID) TONE D-HMQC-2 pulse sequence,[6] we were able to record a partial wideline ^{195}Pt MAS NMR spectrum (Figure S13C). However, the wideline ^{195}Pt MAS NMR spectrum was obtained after 45 hours of acquisition and also suffers from incomplete excitation as the outer sidebands have lower than expected relative intensities (Figure S13D). Unfortunately, due to the low sensitivity, sufficient datapoints to resolve the two CSA patterns could not be obtained within reasonable experimental time. The ^{195}Pt MAS NMR spectrum extracted from the 2D wideline ^{1}H{^{195}Pt} TONE D-HMQC-2 dataset was fit to a CSA pattern with a span (Ω) of 11800 ppm and a skew (κ) of –0.8 (Figure S13D). As discussed in the main text, analysis of the ^{195}Pt NMR spectrum obtained from the sideband-selective D-HMQC and PE RESPDOR data sets gave Ω = 12682 ppm or 12521 ppm and κ = –0.7 (Figure 4 of main text and Figure S14). To the best of our knowledge this is the largest span measured to date for ^{195}Pt.

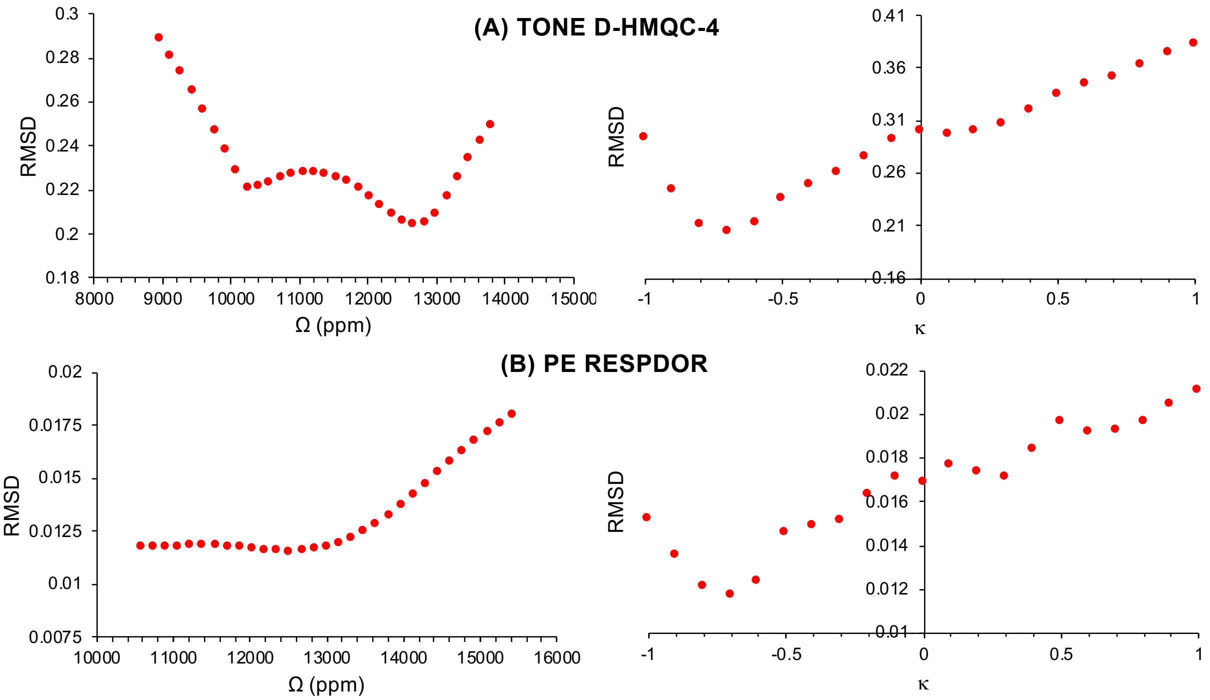

Figure S14. Plots showing the RMSD between the SIMPSON simulated and experimental sideband-selective ^{1}H{^{195}Pt} (A) TONE D-HMQC-4 and (B) PE RESPDOR with Pt(acac)$_2$. κ was initially set to –0.72 for both TONE D-HMQC and PE RESPDOR, and Ω was varied. The Ω with the lowest RMSD was then used to fit κ. SIMPSON simulations in (A) used the TONE D-HMQC-2 pulse sequence.

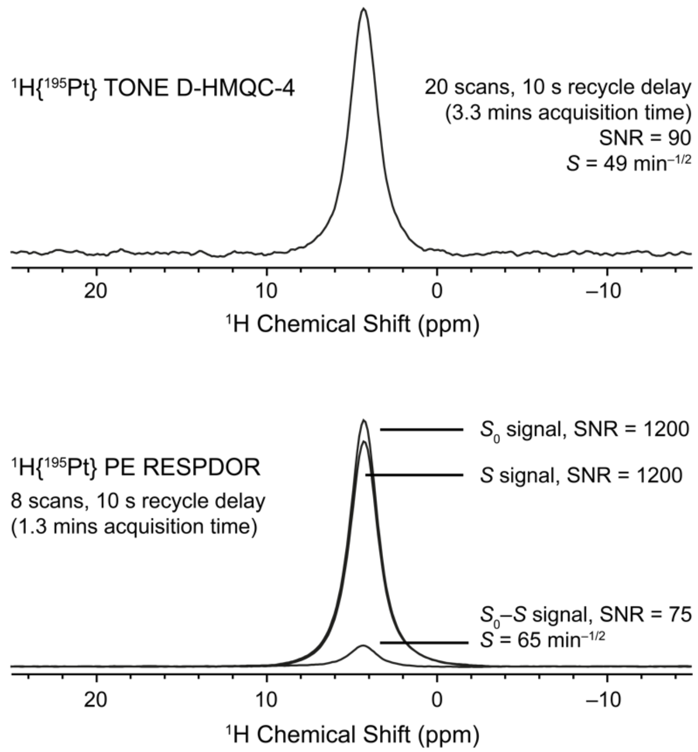

Figure S15. Comparison of sensitivities of sideband-selective 1D ^{1}H{^{195}Pt} (top) TONE D-HMQC-4 and (bottom) PE RESPDOR with cisplatin. The ^{195}Pt transmitter offset for the sideband-selective pulses was placed on the most intense sideband at ca. –4150 ppm. The acquisition times, SNR and overall sensitivities of each spectrum are shown in the figure. Although the sensitivities with TONE D-HMQC-4 and PE RESPDOR are comparable, the error in the PE RESPDOR the dephasing difference signal is greater (10%) than the error in the TONE D-HMQC-4 signal intensity (2%). Notably, these sensitivities are significantly greater than the sensitivities previously obtained with wideline TONE D-HMQC methods (see Venkatesh et al. *J. Magn. Reson.* **2021,** *327*, 106983).

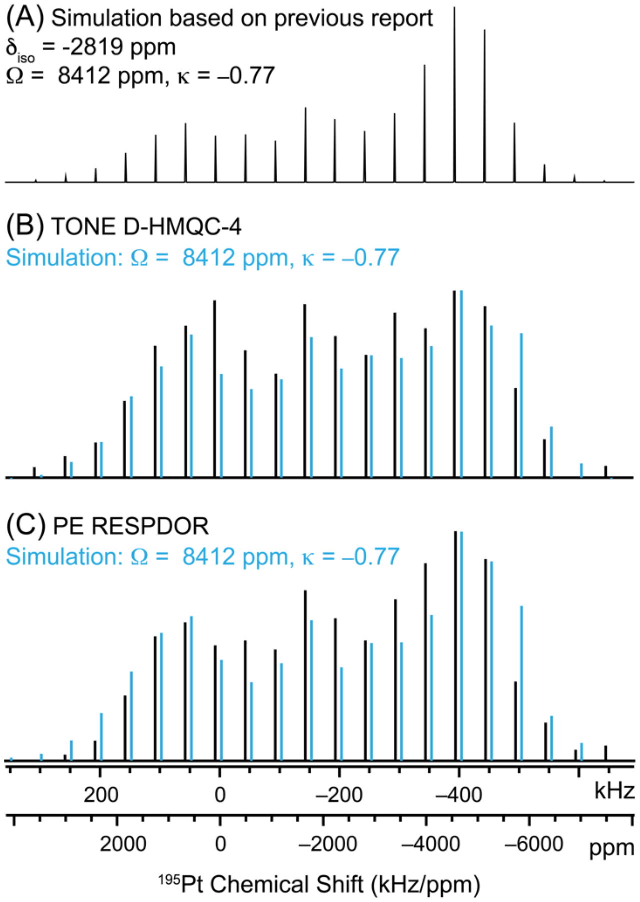

Figure S16. (A) Ideal ^{195}Pt sideband manifold of **3/SiO$_2$** using previously reported CSA parameters (δ_{iso} = –2819 ppm, Ω = 8412 ppm, κ = –0.77). Comparison of (black trace) experimental sideband-selective (B) TONE D-HMQC-4 and (C) PE RESPDOR with (blue trace) SIMPSON simulations; SIMPSON simulation in (B) used the TONE D-HMQC-2 pulse sequence. Simulations used the same previously reported parameters. The fitted spectra are shown in Figure 5A in the main text and Figure S17.

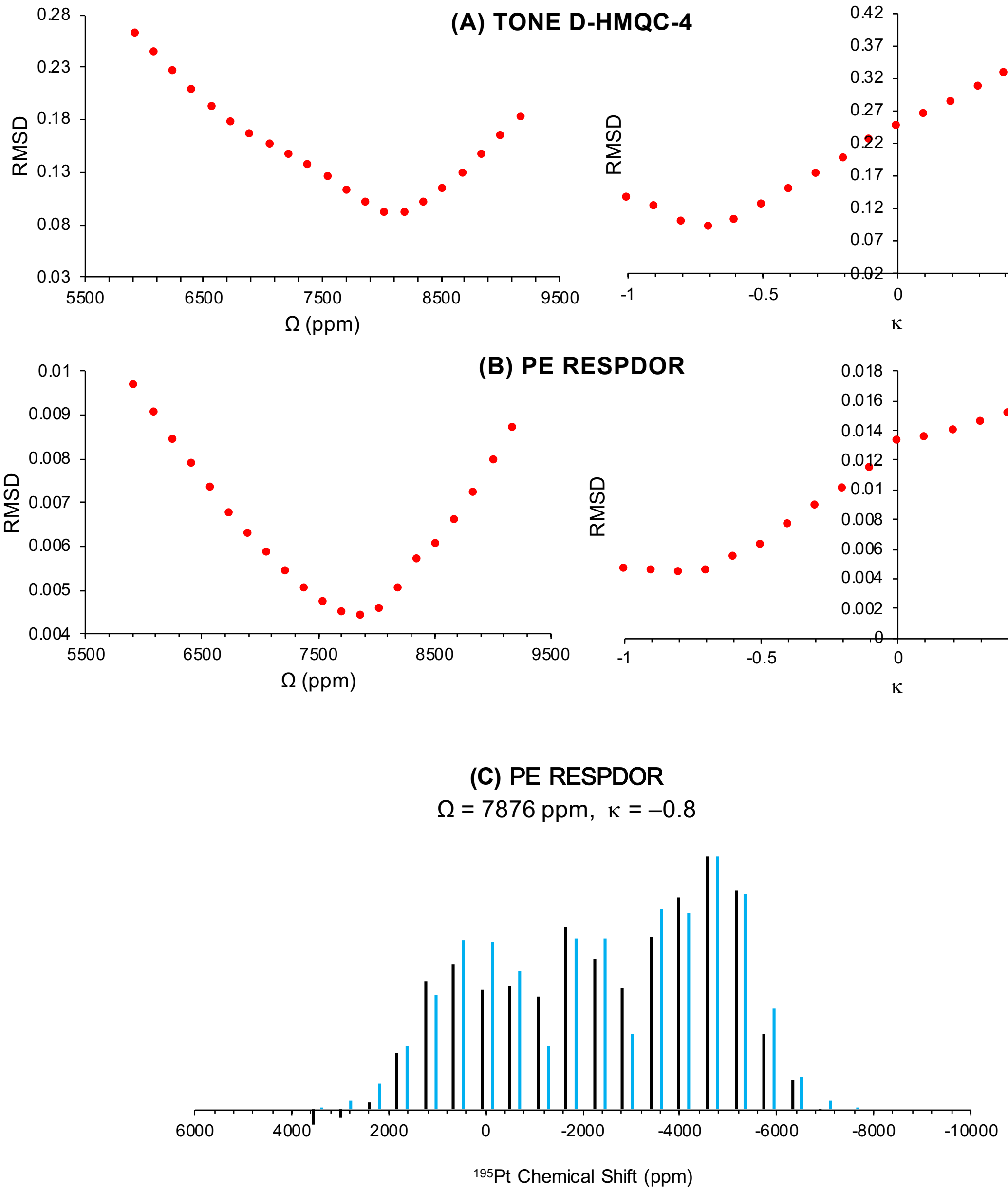

Figure S17. Plots showing the RMSD between the SIMPSON simulated and experimental sideband-selective $^{1}H\{^{195}Pt\}$ (A) TONE D-HMQC-4 and (B) PE RESPDOR with **3/SiO₂**. κ was initially set to –0.69 for both TONE D-HMQC and PE RESPDOR, and Ω was varied. The Ω with the lowest RMSD was then used to fit κ. SIMPSON simulations in (A) used the TONE D-HMQC-2 pulse sequence. (C) Comparison of (black trace) experimental and (blue trace) SIMPSON simulated sideband-selective PE RESPDOR. The entire pattern was obtained in 3 hours of experimental time.

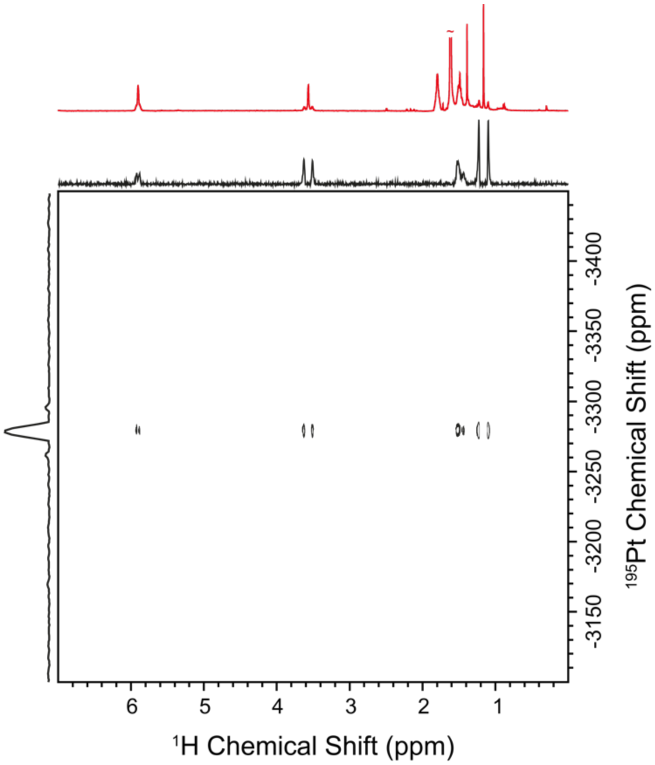

Figure S18. 2D ^{1}H{^{195}Pt} HSQC solution NMR spectrum of **4** dissolved in *d*$_6$-benzene at 14.1 T, obtained without ^{195}Pt decoupling during acquisition. The 1D 1H NMR spectrum is overlaid on top (shown in red).

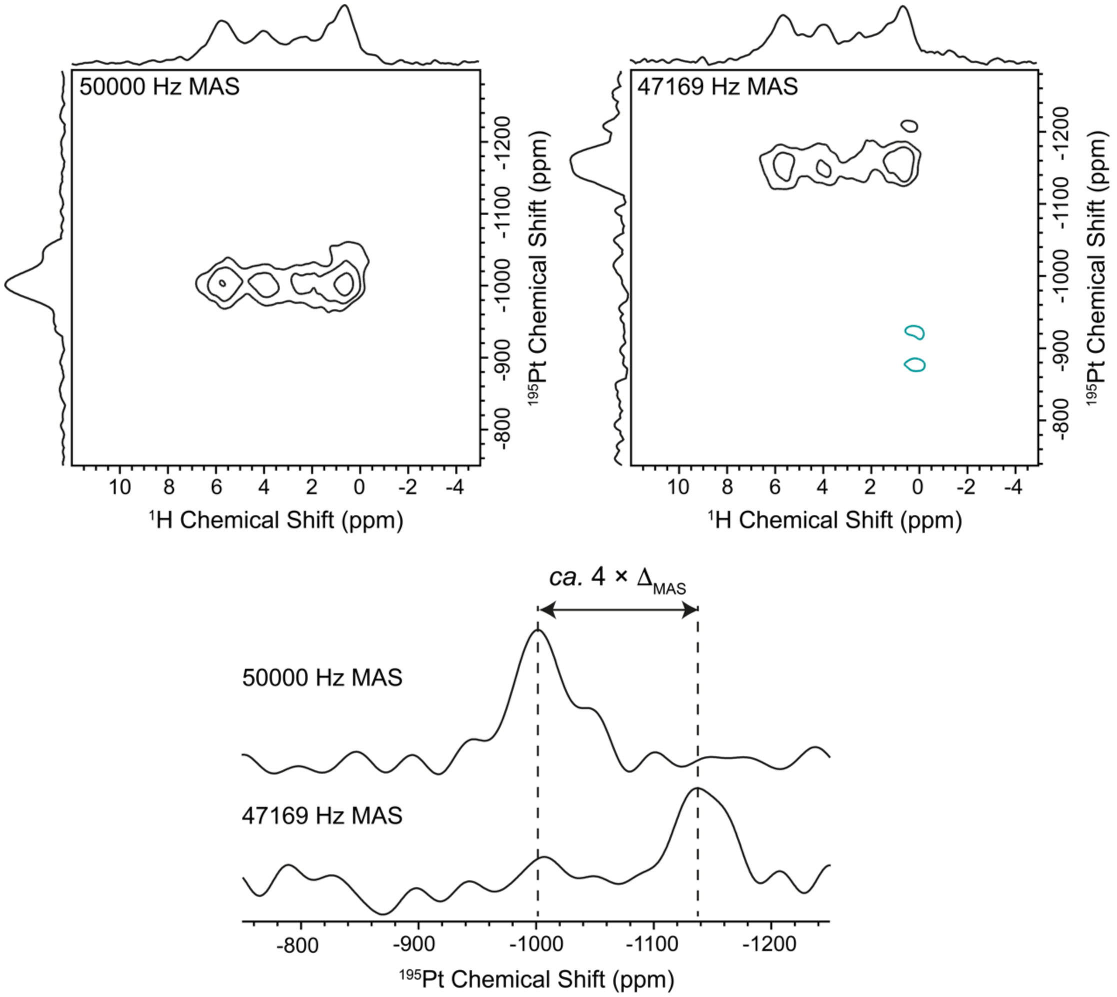

Figure S19. (top) Rotor-synchronized 2D ^{1}H{^{195}Pt} TONE D-HMQC-2 spectra of **4/SiO$_2$** obtained at (left) 50 kHz and (right) 47.169 kHz MAS frequencies. The second MAS frequency of 47.169 kHz was chosen to properly rotor-synchronize the dipolar recoupling sequence. (bottom) 1D ^{195}Pt traces from the 2D showing the frequency difference between the sidebands at the two MAS frequencies, which was used to determine the ^{195}Pt isotropic chemical shift was –3327 ppm. The spectra shown were obtained with 700 scans, 2 s recycle delay and 40 t_1-increments (with STATES-TPPI scheme for quadrature), using optimal total dipolar recoupling durations of 2.56 and 2.544 ms, respectively, at 50000 Hz and 47169 Hz MAS frequencies.

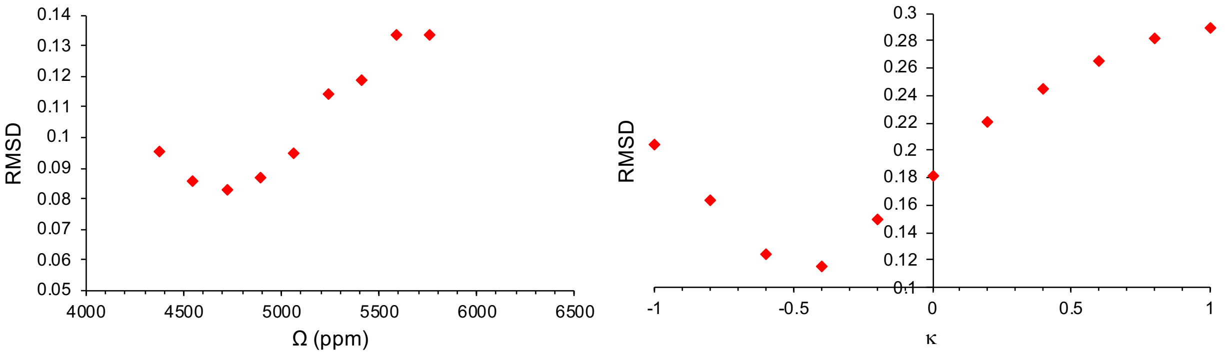

Figure S20. Plots showing the RMSD between the SIMPSON simulated TONE D-HMQC-2 and experimental sideband-selective ^{1}H{^{195}Pt} TONE D-HMQC-4 peak intensities for **4/SiO$_2$**. κ was initially set to –0.47 and Ω was varied. The Ω with the lowest RMSD was then used to fit κ.

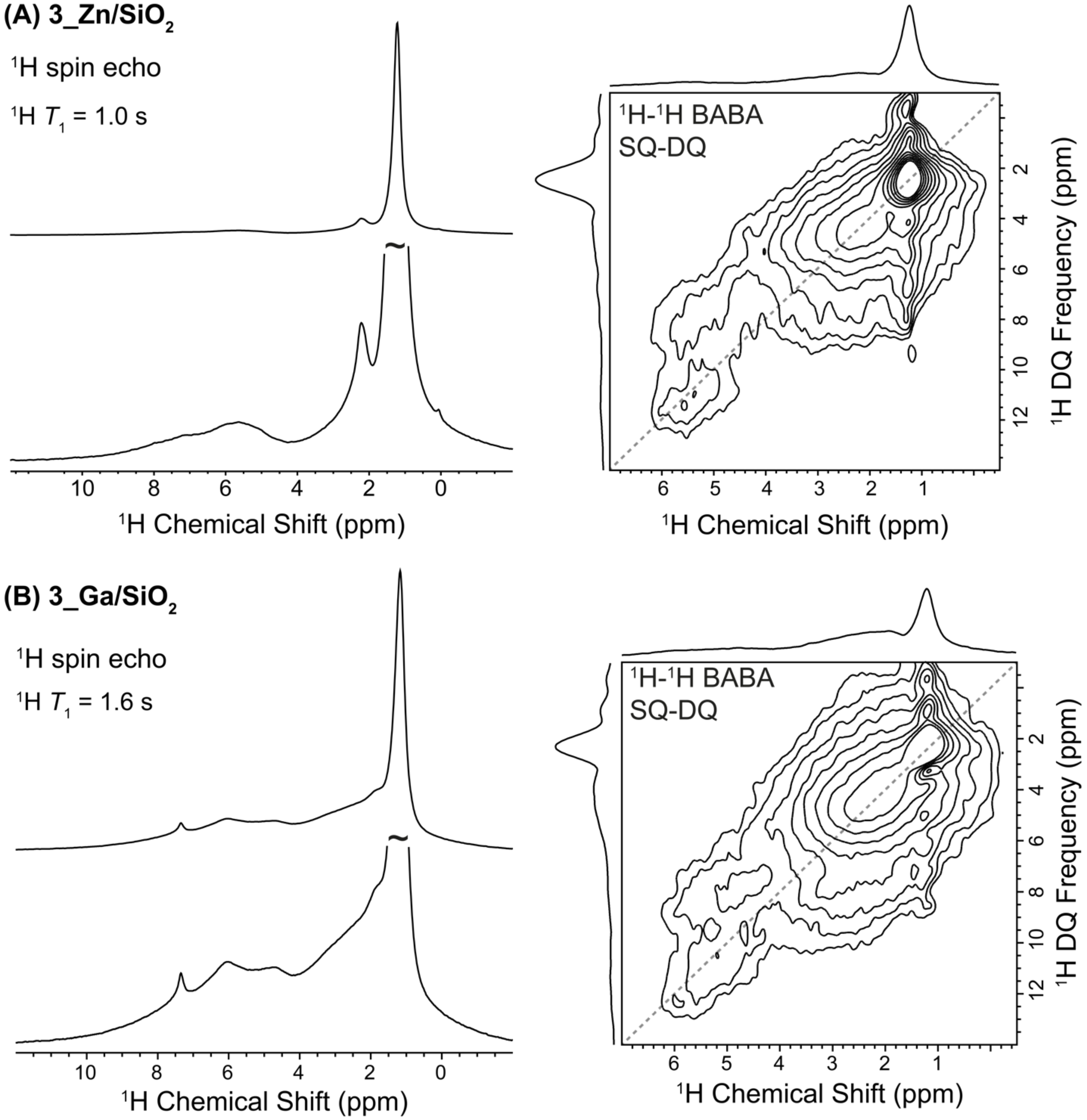

Figure S21. (left) 1D ^{1}H spin echo and (right) 2D ^{1}H-^{1}H SQ-DQ spectra of (A) **3_Zn/SiO$_2$** and (B) **3_Ga/SiO$_2$**. All spectra were obtained at 50 kHz MAS and 9.4 T. ^{1}H T_1 relaxation times were measured using a standard saturation recovery pulse sequence and an optimal recycle delay of 1.3 × T_1 was used to acquire the spectra shown here. The SQ-DQ spectra were obtained with the BABA pulse sequence (M. Feike, D. E. Demco, R. Graf, J. Gottwald, S. Hafner, and H. W. Spiess, Broadband multiple-quantum NMR spectroscopy, *J. Magn. Reson. A*, **1996**, *122*, 214-221).

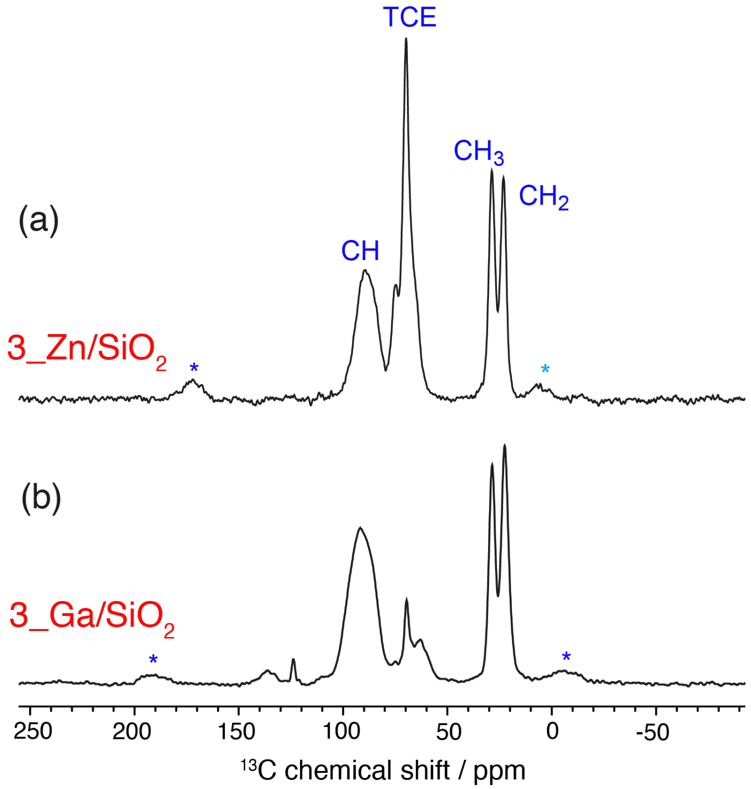

Figure S22. DNP-SENS $^1H \rightarrow ^{13}C$ CP spectra of (a) **3_Zn/SiO$_2$** and (b) **3_Ga/SiO$_2$**. Peaks arising from the CH and CH$_2$ groups of the COD ligand and the CH$_3$ groups of the ^{t}Bu groups of the siloxide ligand are labelled. A solvent suppression CPMAS spin echo pulse sequence was used to partially suppress the signal from the TCE solvent used for impregnation. The spectrum shown in (a) was acquired at a spinning frequency of 8 kHz, with 256 scans, 10 s recycle delay and a 1 ms CP contact time. The duration of the ^{13}C spin echo was 6.25 ms. The spectrum shown in (b) was acquired at a spinning frequency of 10 kHz, with 1024 scans, 10 s recycle delay and a 1 ms CP contact time. The duration of the ^{13}C spin echo was 8 ms. The spectra were recorded at around 105 K on a 9.4 T DNP NMR spectrometer.

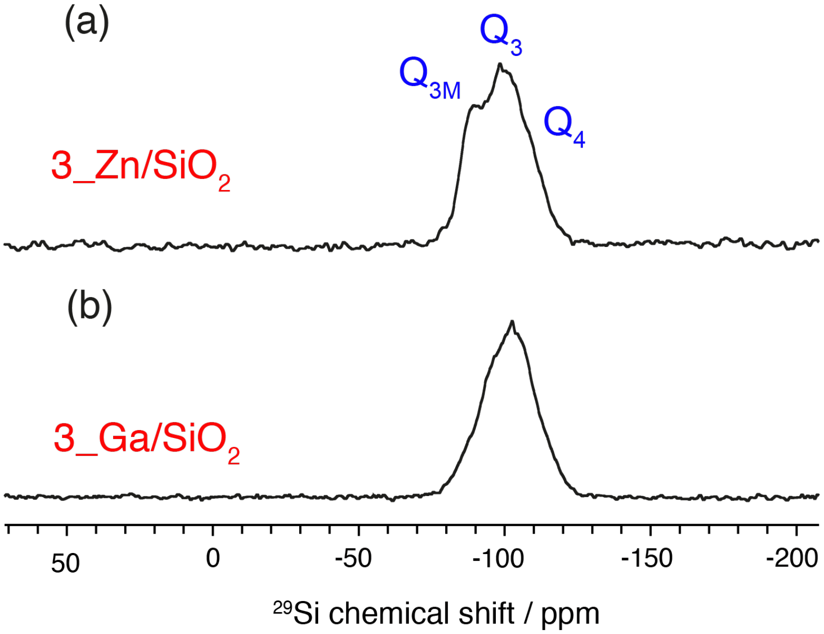

Figure S23. DNP-SENS $^1H \rightarrow {}^{29}Si$ CP spectra of (a) **3_Zn/SiO$_2$** and (b) **3_Ga/SiO$_2$**, showing the Q_4 and Q_3 groups on the surface of the material and the Q_{3M} of the OSi(O*t*Bu)$_3$ ligand of the Pt complex. The spectrum shown in (a) was acquired at a spinning frequency of 8 kHz, with 64 scans, 10 s recycle delay and a 1 ms CP contact time. The spectrum shown in (b) was acquired at a spinning frequency of 10 kHz, with 128 scans, 10 s recycle delay and a 1 ms CP contact time. The spectra were recorded at around 105 K on a 9.4 T DNP NMR spectrometer.

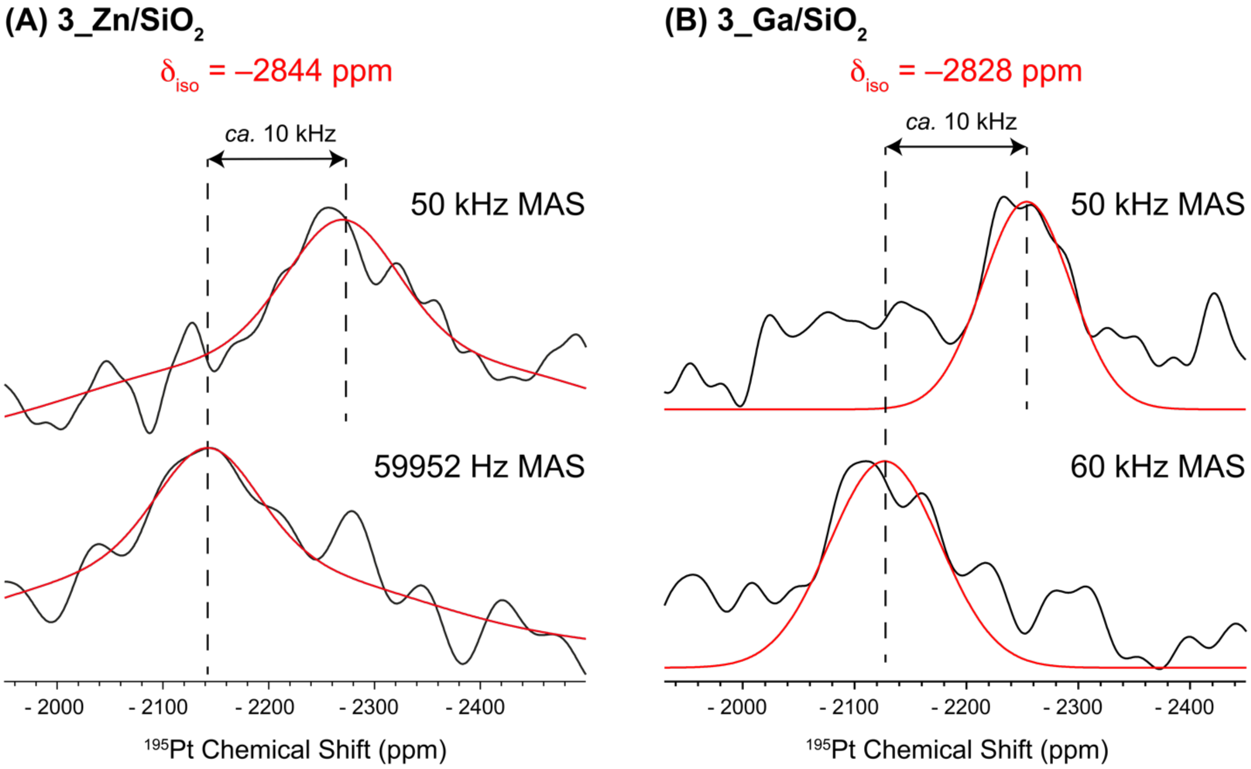

Figure S24. 1D ^{195}Pt traces extracted from rotor-synchronized 2D ^{1}H{^{195}Pt} TONE D-HMQC-4 spectra of (A) **3_Zn/SiO$_2$** and (B) **3_Ga/SiO$_2$** obtained at the indicated MAS frequencies, to determine the ^{195}Pt isotropic chemical shifts. The spectra shown in (A) were obtained with 500 scans, 1.3 s recycle delay and 48 t_1-increments, whereas the spectra shown in (B) were acquired with 400 scans, 2.08 s recycle delay and 40 t_1-increments (with STATES-TPPI scheme for quadrature detection). In both cases the t1-increment was equal to the inverse of the MAS frequency ($\Delta t_1 = 1/\nu_{rot}$).

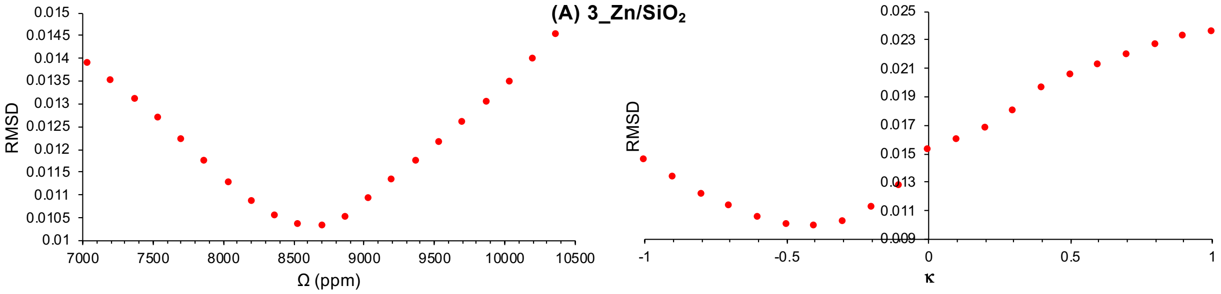
(A) 3_Zn/SiO$_2$

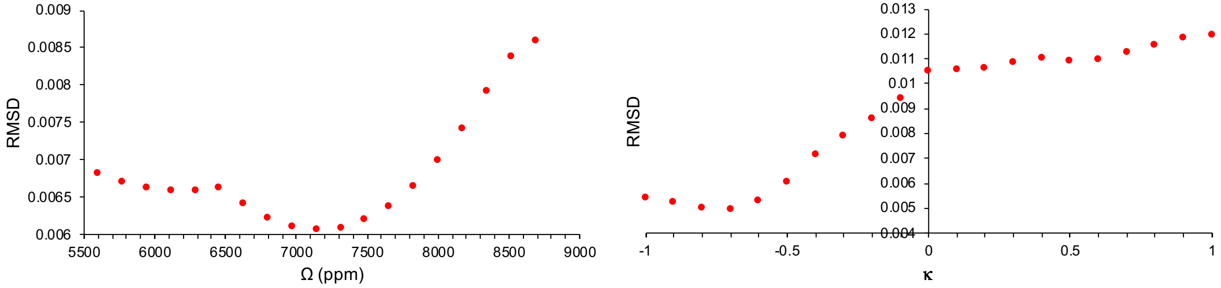
(B) 3_Ga/SiO$_2$

Figure S25. Plots showing the RMSD between the SIMPSON simulated and experimental sideband-selective ^{1}H{^{195}Pt} PE RESPDOR with **3_Zn/SiO$_2$** and **3_Ga/SiO$_2$**. κ was initially set to –0.6 and –0.5, respectively, for **3_Zn/SiO$_2$** and **3_Ga/SiO$_2$**, and then Ω was varied. The Ω with the lowest RMSD was then used to fit κ.

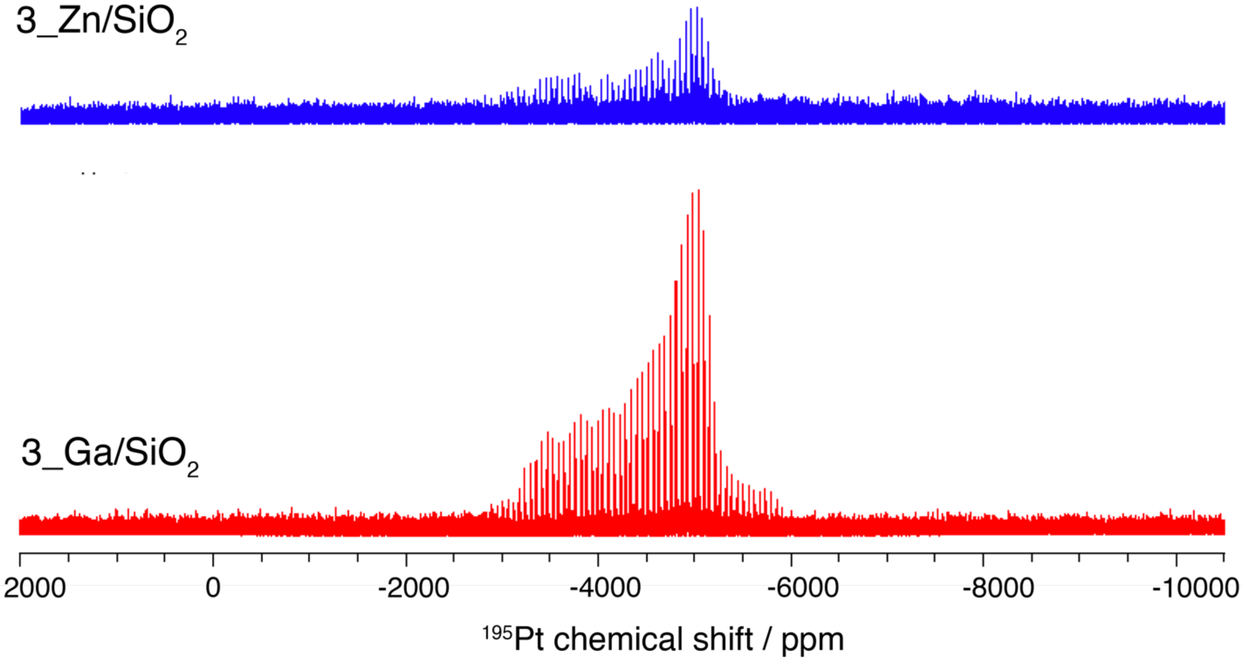

Figure S26. DNP enhanced $^{1}H \rightarrow ^{195}Pt$ BRAIN-CP-WCPMG spectra of **3_Zn/SiO₂** and **3_Ga/SiO₂** at 9.4 T and 105 K. A ^{1}H excitation pulse of 2.5 us was used followed by a 10 ms contact time, with WURST swept over 400 kHz applied to ^{195}Pt. For detection 50 µs WURST pulses were swept over 400 kHz with a spikelet separation of 5 kHz. Variable offset accumulation was used by stepping the transmitter by 100 kHz. The spectrum of **3_Ga/SiO₂** was obtained with a 6 s recycle delay, 2048 scans per sub-spectrum at five different offsets (17.1 hours total experiment time). The spectrum of **3_Zn/SiO₂** was obtained with a 10 s recycle delay, 2048 scans per sub-spectrum at two different offsets (11.3 hours total experiment time).

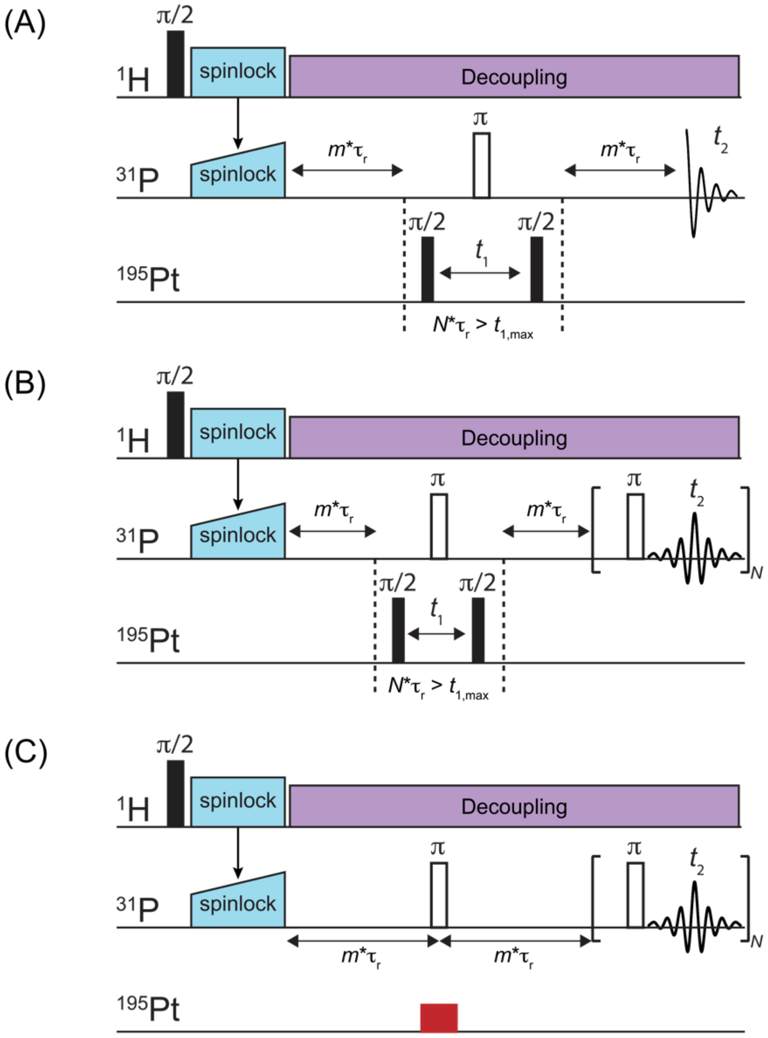

Figure S27. Pulse sequences used for the acquisition of (A) constant-time 2D ^{1}H-^{31}P{^{195}Pt} CP *J*-HMQC spectrum of **5**, (B) constant-time, rotor-synchronized 2D ^{1}H-^{31}P{^{195}Pt} CP *J*-HMQC spectra of **5/SiO$_2$** obtained with CPMG detection, and (C) sideband-selective ^{1}H-^{31}P{^{195}Pt} CP *J*-resolved spectra of **5/SiO$_2$** obtained with CPMG detection.

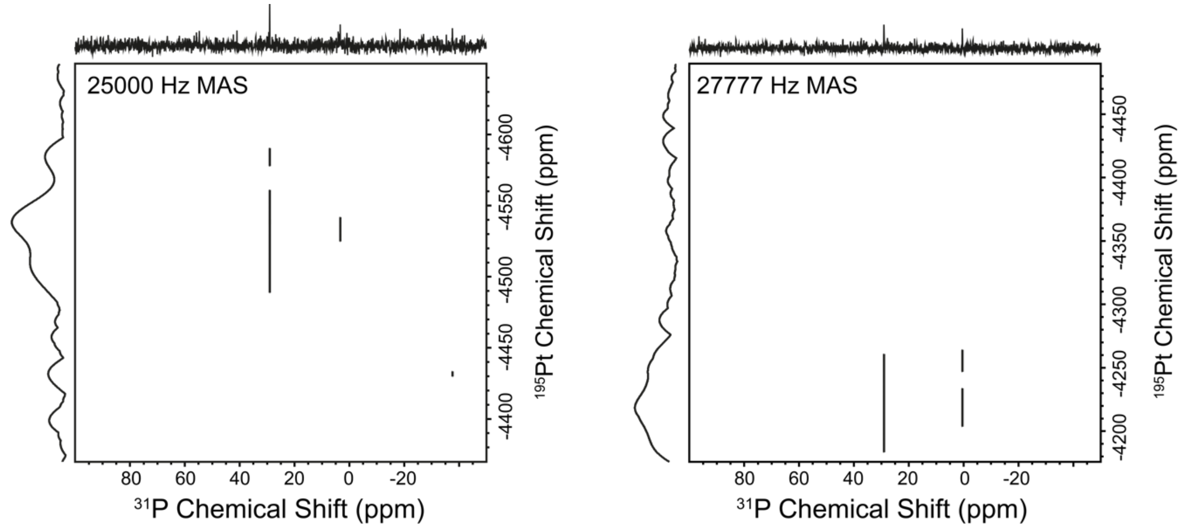

Figure S28. Constant-time, rotor-synchronized 2D ^{1}H-^{31}P{^{195}Pt} CP J-HMQC spectra of **5/SiO$_2$** obtained using CPMG detection and the indicated MAS frequencies. In both cases, the F_1 spectral width was equal to the MAS frequency and 50 complex increments were acquired. 640 scans and a 1.5 s recycle delay was used. The ^{195}Pt isotropic shift was determined to be –4231 ppm. The total mixing time ($2 \times m \times \tau_r$) was 480 μs (pulse sequence shown in Figure S27B). The total echo duration in the CPMG train was set to 4 rotor periods and (left) 201 and (right) 225 CPMG loops (spin echoes) were acquired.

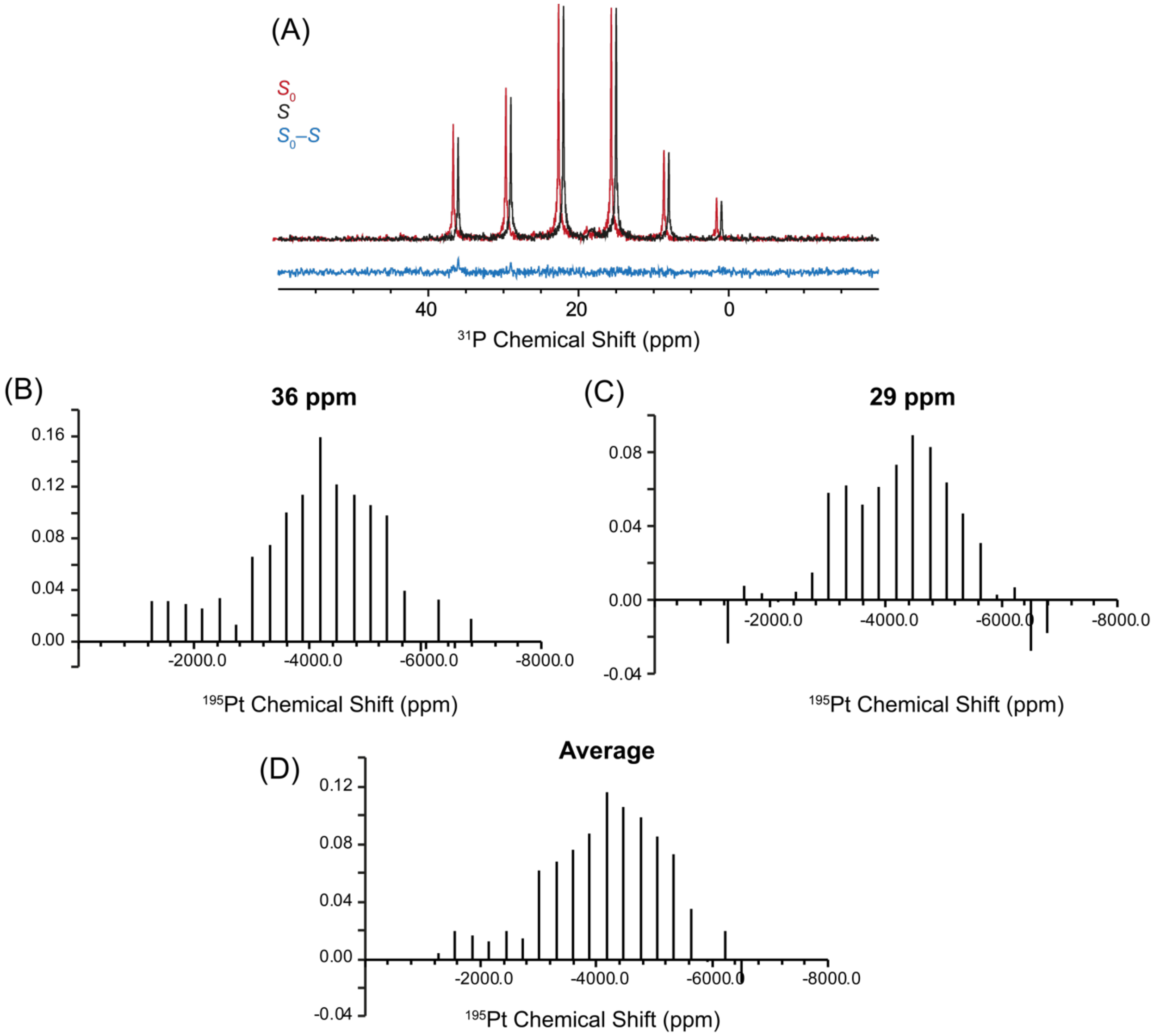

Figure S29. Sideband-selective ^{195}Pt CSA patterns of **5/SiO₂** acquired with a ^{1}H-^{31}P{^{195}Pt} CP J-resolved pulse sequence using CPMG detection and 25 kHz MAS. (A) ^{31}P control (S_0), dephased (S) and difference (S_0–S) traces obtained with a 40 μs ^{195}Pt saturation pulse, 22 kHz rf and a ^{195}Pt transmitter offset of –4180 ppm. Plots showing the dephasing difference (S_0–S) of CPMG spikelets at (A) 36 ppm and (B) 29 ppm; (C) average dephasing of the spikelets at 36 and 29 ppm.

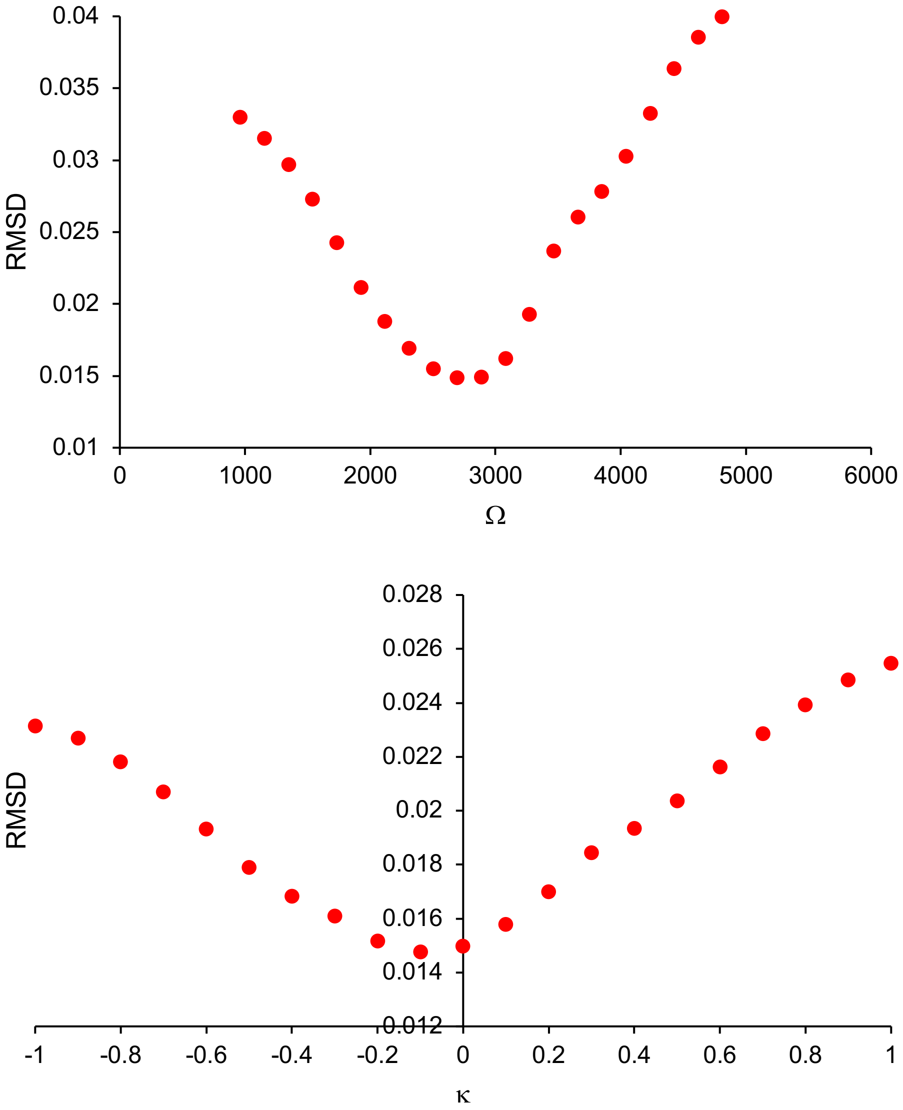

Figure S30. Plots showing the RMSD between the SIMPSON simulated and experimental sideband-selective ^{1}H-^{31}P{^{195}Pt} CP J-resolved experiments with **5/SiO$_2$** shown in Figure 7D. (top) Based on a visual inspection of the sideband pattern, κ was initially set to 0.11 and Ω was varied. The RMSD was minimized to a Ω of 2695 ppm. (bottom) Using Ω = 2695, the lowest RMSD was obtained with a κ of –0.1.

Table S2: Table showing comparison of experimental and DFT calculated ^{195}Pt CS tensor parameters, in the Herzfeld-Berger notation.

Compound	**Experiments**							**DFT***		
		Wideline static or D-HMQC methods#		**Sideband-Selective TONE D-HMQC-4**		**Sideband-Selective PE RESPDOR**				
	δ_{iso} (ppm)	**Ω (ppm)**	**κ**	**Ω (ppm)**	**κ**	**Ω (ppm)**	**κ**	**δ_{iso} (ppm)**	**Ω (ppm)**	**κ**
1	–1834	8975	–0.96	8816	–0.95	8687	–0.7	–1563 (–1897)	9420 (8350)	–0.88 (–0.92)
2	–360, –385	11800	–0.8	12682	–0.7	12521	–0.7	280 (–216)	14071 (12782)	–0.85 (–0.80)
3/SiO_2	–2819	8412	–0.77	8039	–0.7	7876	–0.8	–2959	6703	–0.97
4/SiO_2	–3327	-	-	4719	–0.4	-	-	–3196	5235	–0.47
5	–4503	-	-	630	–0.4	-	-	–4515	1111	–0.99
5/SiO_2	–4769	-	-	2695	–0.1	-	-	–4132	3480	–0.125

*Values provided in parentheses were obtained by fixing the heavy-atom positions from the crystal structure. All other DFT calculations were performed by relaxing all atoms prior to performing NMR calculations.

#^{195}Pt CSA parameters for **1** and **3/SiO_2** were previously reported.[7-9]

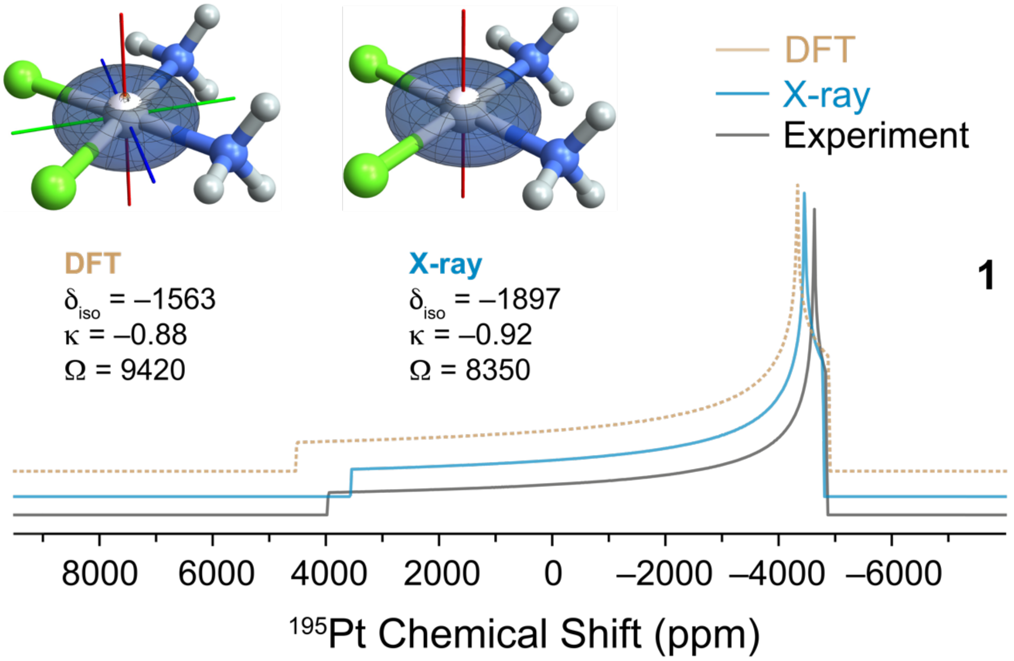

Figure S31. CS components of the Pt nucleus in **(1)** were computed for both the X-ray ($d_{Pt\text{-}N}$ = 2.05Å) and the optimized DFT optimized structures ($d_{Pt\text{-}N}$ = 2.11Å). The calculation of ^{195}Pt CS tensor parameters with the DFT optimized structure results in an overestimation of δ_{zz} by ca. 1000 ppm. The previously reported X-ray structure of alpha-cisplatin was used.[10]

Note S3. Orbital rotation model

The information on the electronic structure of a Pt center is encoded within the CS tensor, which depends on diamagnetic and paramagnetic contributions, that also include spin-orbit (SO) coupling effects (eq. 1):

$$\delta = \delta_{dia} + \delta_{para+SO} \qquad (1)$$

In all cases, the diamagnetic contributions, mostly related to core orbitals, are often constant for all Pt nuclei across a broad range of compounds, while paramagnetic contributions are strongly dependent on the electronic structure of Pt, *i.e.* valence orbitals, e.g. electron pairs localised in the non-bonding Pt 5d orbitals and low-lying antibonding Pt-ligand orbitals. The magnitude of the paramagnetic term (excluding SO terms) originates from the coupling between low-lying vacant orbital (Ψ_{vac}) with high-lying occupied orbitals (Ψ_{occ}), that are orthogonal to each-other and close in energy, upon action of the magnetic moment operator $\hat{L_i}$ (i= x, y, z) (eq.2).

$$\delta_{ii,para} \Leftrightarrow \frac{\langle \Psi_{vac} | \hat{L}_i | \Psi_{occ} \rangle \langle \Psi_{vac} | \hat{L}_i / r^3 | \Psi_{occ} \rangle}{\Delta E_{vac-occ}} \qquad (2)$$

For the general class of square planar $Pt^{II}L_4$ complexes, deshielding for the CS component along the *z* direction (δ_z), originate from the coupling of the high-lying, filled d_{xy} orbital with the antibonding σ *(Pt-L) orbital by the $\hat{L_z}$ operator and, to a minor extent, from the filled d_{xz} and d_{yz} Pt orbitals coupling with the specific σ *(Pt-L) along the y or x axis, by $\hat{L_y}$ and $\hat{L_x}$ respectively (Figure 8B).[11]

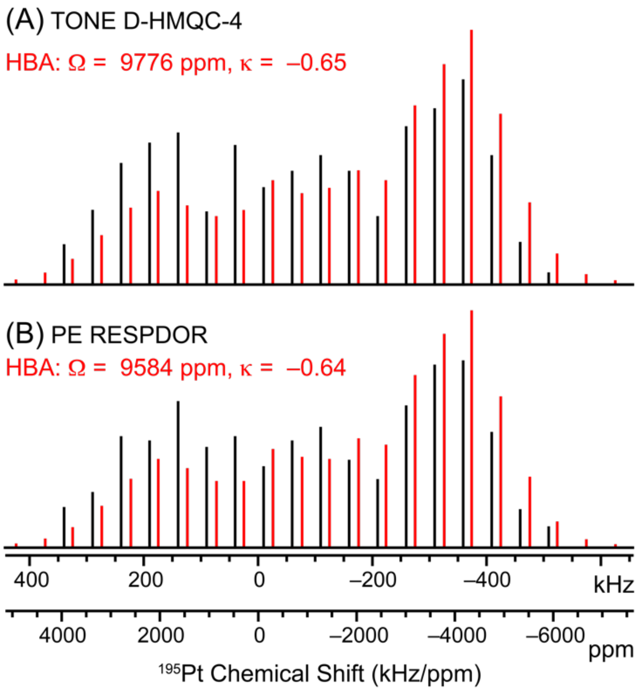

Figure S32. Estimation of ^{195}Pt CSA from ^{1}H{^{195}Pt} sideband-selective experiments with cisplatin, using Herzfeld-Berger analysis (HBA). (black trace) Sideband-selective (A) TONE D-HMQC-4, and (B) PE RESPDOR experiments and (red trace) fitted sideband signal intensities from HBA.

Supporting Information References:

1. Venkatesh, A.; Luan, X.; Perras, F. A.; Hung, I.; Huang, W.; Rossini, A. J. t_1-Noise Eliminated Dipolar Heteronuclear Multiple-Quantum Coherence Solid-State NMR Spectroscopy. *Phys. Chem. Chem. Phys.* **2020,** *22*, 20815-20828.
2. Parella, T. Towards Perfect NMR: Spin-Echo versus Perfect-Echo Building Blocks. *Magn. Reson. Chem.* **2019,** *57* (1), 13-29.
3. Takegoshi, K.; Ogura, K.; Hikichi, K. A Perfect Spin-Echo in a Weakly Homonuclear J-Coupled 2 Spin-1/2 System. *J. Magn. Reson.* **1989,** *84* (3), 611-615.
4. Vanzijl, P. C. M.; Moonen, C. T. W.; Vonkienlin, M. Homonuclear-J Refocusing in Echo Spectroscopy. *J. Magn. Reson.* **1990,** *89* (1), 28-40.
5. Ha, K. Crystal structure of bis(pentane-2,4-dionato-kappa O-2,O ')platinum(II), Pt(C5H7O2)(2). *Z Krist-New Cryst St* **2011,** *226* (3), 329-330.
6. Venkatesh, A.; Perras, F. A.; Rossini, A. J. Proton-detected solid-state NMR spectroscopy of spin-1/2 nuclei with large chemical shift anisotropy. *J. Magn. Reson.* **2021,** *327*, 106983.
7. Venkatesh, A.; Lund, A.; Rochlitz, L.; Jabbour, R.; Gordon, C. P.; Menzildjian, G.; Viger-Gravel, J.; Berruyer, P.; Gajan, D.; Copéret, C.; Lesage, A.; Rossini, A. J. The Structure of Molecular and Surface Platinum Sites Determined by DNP-SENS and Fast MAS ^{195}Pt Solid-State NMR Spectroscopy. *J. Am. Chem. Soc.* **2020,** *142* (44), 18936-18945.
8. Lucier, B. E. G.; Reidel, A. R.; Schurko, R. W. Multinuclear Solid-State NMR of Square-Planar Platinum Complexes - Cisplatin and Related Systems. *Canadian Journal of Chemistry-Revue Canadienne De Chimie* **2011,** *89* (7), 919-937.
9. Rossini, A. J.; Hanrahan, M. P.; Thuo, M. Rapid Acquisition of Wideline MAS Solid-State NMR Spectra with Fast MAS, Proton Detection, and Dipolar HMQC Pulse Sequences. *Phys. Chem. Chem. Phys.* **2016,** *18* (36), 25284-25295.
10. Ting, V. P.; Schmidtmann, M.; Wilson, C. C.; Weller, M. T. Cisplatin: Polymorphism and Structural Insights into an Important Chemotherapeutic Drug. *Angew Chem Int Edit* **2010,** *49* (49), 9408-9411.
11. Autschbach, J.; Zheng, S. H. Analyzing Pt Chemical Shifts Calculated from Relativistic Density Functional Theory Using Localized Orbitals: The Role of Pt 5d Lone Pairs. *Magn. Reson. Chem.* **2008,** *46*, S45-S55.